Spin-Echo Small-Angle Neutron Scattering Development

Ontwikkeling van Spin-Echo Kleine-Hoek Neutronenverstrooiing

Spin-Echo Small-Angle
Neutron Scattering
Development

Contents

Chapter 1

Introduction

A great deal of our understanding of the structure of matter comes from scattering techniques. This can vary from elementary particles to macro objects. Small-Angle Neutron Scattering (SANS) is one such scattering technique by which one can obtain structural information of materials, varying from bacteria to steel precipitates. Structural information means the size and the form of the object. In SANS one obtains data as a function of the momentum transfer which is connected with the angle of scattering. To measure the structure of large objects which means measuring very small angles, the incident beam needs to be collimated and the detector is put at large distances from the sample. This detector is position sensitive: it includes several thousands of pixels illuminated by the beam. At D11 at ILL one can put the detector at a distance up to 40 m from the sample. The neutron intensity drops quadratically with the distance. Therefore, it takes a lot of effort and time to measure small scattering angles which limits the maximum size of objects to 200 nm. In SESANS one measures depolarization as a function of the so called spin-echo length which is a real space parameter. Each data point automatically includes integration over the momentum space and there is no need to collimate the beam. So, very small scattering angles are included as easily as large angles and need not be measured explicitly with the consequence that with SESANS one measures with high intensity over a large size range.

In Fig. 1.1 an overview is given to measure different objects by means of diffraction and microscopic techniques. SANS covers a range from 0.3 nm to 200 nm whereas USANS (Ultra-SANS) covers a range from 300 nm to 30 μm [1]. However, to measure such a large range with USANS one has to use perfect Si crystals with mosaicities of arc seconds. This means that the intensity drops tremendously. One can measure objects with SESANS from 2 nm up to the micron region with a divergent beam where there is no loss of

neutron intensity. Although the microscopical techniques cover a large range they are not suited to measure bulk properties.

We said that the beam has to be collimated in SANS measurements, and this means that the incoming neutron wave vectors are determined precisely. The sample and the pixel position determine the outgoing wave vector. Therefore, to get information on the momentum transfer both determinations are done precisely which leads to intensity loss. If in someway the momentum transfer could be measured directly without collimation there would be no loss of intensity.

A method to realize this is to use the spin-echo principle. There is a convenient analogy to understand this principle. Suppose three runners run a race over a circle. The runners start from the same position on the circle. After some time, the runners will have run different distances. At that time the runners are told to stop and turn and run back. By doing so they will arrive at the same time at the starting position. So the initial and final situation for the runners is the same and we may say that the final situation is in echo with the initial one. However, if something happens to the runners during their run so that they change their speed, the final situation will not be the same as the initial one and the final situation will not be in echo with the initial one.

The neutron is a spin-half particle, and this property of the neutron gives it an extra degree of freedom which can be used in experiments. The neutron spin precesses in a magnetic field. This precessional motion is called Larmor precession that can be used as an internal clock in experiments with polarized neutrons. One can make this clock run say in a clockwise direction and then make it run in the counterclockwise direction. The initial and final state is then the same. This is called the spin-echo principle. However, if there is a scattering process the velocity of the neutrons change. So, the final state will not be the same as the initial one.

There is a small difference between the analogy and the neutrons. For the neutron clock to run in the counterclockwise direction, the neutrons do not travel back, but continue in the same direction.

In 1973 the first inelastic Spin-Echo spectrometer was built in Grenoble based on Larmor precession of neutrons [2]. The importance of the spin-echo spectrometer is that it can measure extremely small energy transfers in inelastic processes.

In 1978 R. Pynn proposed to use magnets tilted with respect to mean neutron direction in a spin-echo three axis spectrometer to make the precession depend on the orientation of the incoming neutron beam with respect to the tilt angle [3]. In this way the neutrons are labelled with the scattering angle.
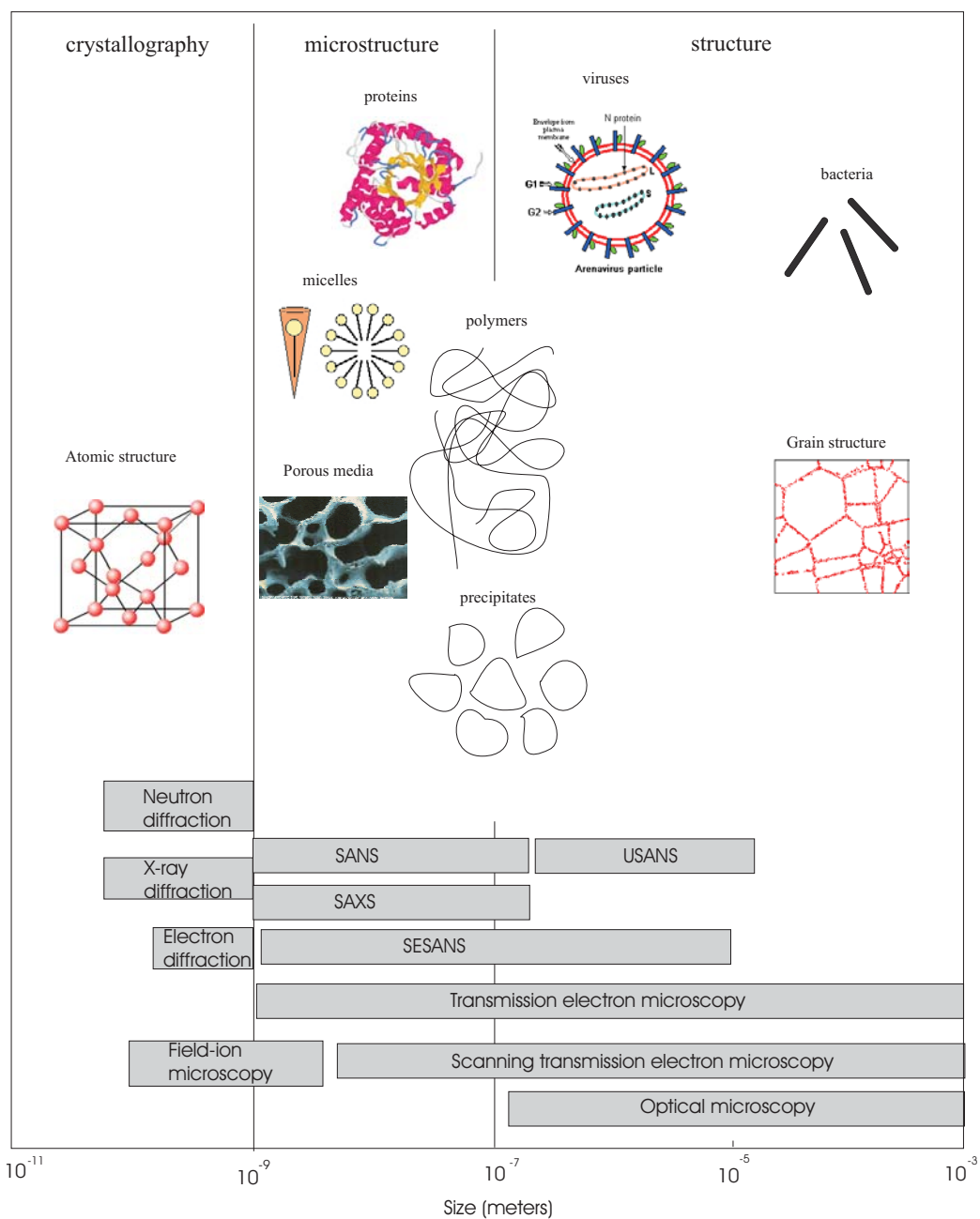
Figure 1.1: An overview of the length sizes which can be measured by diffraction and microscopic techniques. SESANS covers a range varying from a few nanometers up to the micron region.

In 1993 Lebedev et.al proposed the real space small-angle scattering device [4]. In their device the intensity of an unpolarized beam is modulated before and after the scattering process by two grids. The first grid makes a square modulation whereas the second one makes a sinusoidal modulation. The detected intensity is proportional to the product of the transmission of these modulators multiplied by the scattering cross-section. In first order the intensity is then proportional to the cosine transform of the scattering cross-section in momentum space if the transmission factors are expanded in their Fourier series, whereby retaining only the first order coefficients. In this way it was possible to measure directly the Fourier transform of the the scattering cross-section which gives the correlation function. They were able to determine the radius of latex spheres with radii of 710 $\mathring{A}$ and 2500 $\mathring{A}$. The latex spheres had a concentration of 25 % which means that multiple scattering effects and structure factor must have played an important role. However, these considerations are not included in the analysis.

In 1995 Keller et.al applied the method of angle labelling proposed by R. Pynn on the Neutron Resonance Spin Echo spectrometer (NRSE) at BENSC [5]. Because of this labelling, the amount of precession in the two arms of the spectrometer will be different if a small-angle scattering process happens in a sample placed between the arms. As a consequence, the final polarization is less than the initial polarization. The difference in precession will have a first order dependence on the angle of scattering and hence on the momentum transfer Q. If the scattering power of the sample is $S(Q)$, then the final polarization is proportional to the Fourier transform of $S(Q)$, i.e. to $G(\delta)$, the density-density correlation function. Keller et.al called δ the spin-echo length similar to the spin-echo time in inelastic scattering. In their article the authors present a measurement of the depolarization as a function of the spin-echo length on porous glass. The spin-echo length covers a range of 25 to 400 nm.

In 1996 Rekveldt [6] proposed triangularly shaped precession areas to label the neutron precession. In this way only precession in the triangles are required and no precession is required in the region between the triangles. There are two advantages of this technique. Firstly, the contribution of elastic scattering can be amplified by choosing the distance between the triangles large compared to the size of the triangles. Secondly, there is less precession required which reduces possible errors. This method is called Spin-Echo Small-Angle Neutron Scattering or SESANS.
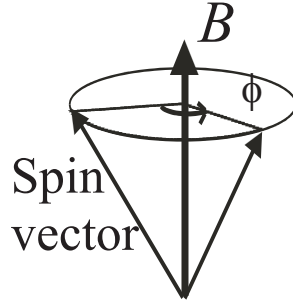
Figure 1.2: Precession of the spin vector around the magnetic field vector

1.1   Layout of the thesis

In the remainder of this chapter, some basic components used in the SESANS setup will be explained, and the SESANS theory will be formulated.

In chapter 2 the design parameters for the magnetic components in the SESANS instrument will be calculated. In this respect two requirements have to be fulfilled: homogeneity of the magnetic fields in the SESANS magnets and the line integral homogeneity.

In chapter 3 line integral corrections will be discussed. The line integral homogeneities cannot be corrected by changing the magnet parameters and therefore, it is corrected by external coils. This is done in two steps. In the first step, line integral inhomogeneities are transformed form one of the perpendicular directions to the neutron beam into the other direction. By doing so, there is only line integral inhomogeneity in one direction. In the second step this remaining inhomogeneity is corrected by a parabolically shaped coil.

In chapter 4 we will discuss some model calculations. These include, spherical systems, the effect of Gaussian polydispersity, structure factor effects, multishell model, ellipsoid of revolution and cylindrical model. The Debye-Lorentz model will be treated analytically.

In chapter 5 SESANS measurements done so far will be shown. This includes measurements on limestone and spherical particles.

Finally, in chapter 6 the conclusions will be given.

1.2   Polarization and polarizers

Polarization of a neutron beam is defined as:

$$P = \frac{I_+ - I_-}{I_+ + I_-}. \tag{1.1}$$

Here $I_\pm$ are the spin up and down intensities.

When neutrons are produced, there are as many as spin-up as spin-down neutrons. In order to select one spin state neutrons are reflected on supermiror surfaces. This consists of magnetically scattering layers which scatter one of the spin-states more strongly than the other. A polarizer is then a box with an entrance and exit window between which a stack of these supermirror layers are mounted [7].

1.3   Larmor precession

When a neutron enters a magnetic field region as shown in Fig.1.2, its spin starts to rotate around the direction of the **B** field. In quantum mechanics for every operator A in the Schrödinger picture the corresponding operator $A_H(t) = U(t)AU^\dagger(t)$ in the Heisenberg picture can be written where $U(t) = e^{-\frac{i}{\hbar}Ht}$ is the evolution operator. The Heisenberg equation of motion is given by [8]:

$$\frac{dA_H(t)}{dt} = -\frac{1}{i\hbar}[A_H, H_H] + \frac{\partial A_H}{\partial t} \tag{1.2}$$

This equation can be used to write the equation of motion for the Pauli spin vector $\vec{\sigma}(t)$ after working out the commutator by using $H = -\gamma\vec{\sigma} \cdot \mathbf{B}$ and the evolution operator. Here γ is the gyromagnetic ratio. This gives:

$$\frac{d\vec{\sigma}(t)}{dt} = \gamma\vec{\sigma} \times \mathbf{B}. \tag{1.3}$$

By taking the ensemble average of Eq. 1.3 and noting that $\mathbf{P} = <\vec{\sigma}>$ one obtains:

$$\frac{d\mathbf{P}(t)}{dt} = \gamma\mathbf{P} \times \mathbf{B}. \tag{1.4}$$

When this equation is solved, the solution of $\mathbf{P}(t)$ appears to be the Larmor precession of $\mathbf{P}(t)$ around $\mathbf{B}$ with the Larmor frequency $\omega = \gamma B$. For a neutron which has interaction in a magnetic field region over a length l the total rotation angle is:

$$\phi = \omega t = \gamma B\frac{ml\lambda}{h}. \tag{1.5}$$

Here m is the neutron mass, h the Planck constant, and λ the wavelength. More generally, when the field is varying:

$$\phi = \frac{\gamma m}{h} \lambda \int_{path} |B| dl = c\lambda \int_{path} |B| dl \qquad (1.6)$$

where $c = 4.63 \times 10^{14}$ T $^{-1}\cdot$ m $^{-2}$.

1.4 Flippers

Flippers are used to change the direction of the spin vector so that the two spin states can be measured. In the top and middle drawing of Fig. 1.3 a flipper used in the SESANS instrument is shown [9]. It consists of two identical coils. The coils are wound in such a way that they can produce a magnetic field in the y-direction. In Fig. 1.3 the first part of the flipper produces a field in the $+y$ direction whereas the second part produces a field in the $\pm y$ direction according to the polarity of the current. In the bottom figure, the fields inside and outside the flipper are plotted. For $x < 150$ mm the dominant field is the stray field of the magnet which is in the z direction whereas for $x > 150$ mm the dominant field is due to the stray field of the analyzer that is in the z direction. In the first part of the flipper the field is in the y direction. So, the total field turns from the z direction to the y direction and the neutrons follow this slow change. In the second part of the flipper, $0 < x < 150$ mm, the field can be in the y direction. So, the total field turns from the y direction to the z direction which is followed by the neutrons. This results in measurement of the spin up state. However, when the field in the second part of the flipper is in the $-y$ direction, the neutrons cannot follow this rapid change in the field direction. So, the neutron spin will still point in the y direction. Therefore, when the field changes from $-y$ to z, the spin direction changes from $-y$ to $-z$ direction. In this case the spin down state can be measured.

1.5 Magnetic foils as polarisation manipulators

Magnetized foils can be used as flippers [10]. To realize this we use a foil (see Fig. 1.4a) of a soft magnetic material placed between the poles of an electromagnet which is magnetized to saturation by the applied magnetic field B_{ext}. This local strong magnetic field is very convenient for manipulation of the neutron polarization. The neutron in the foil is subject to an effective
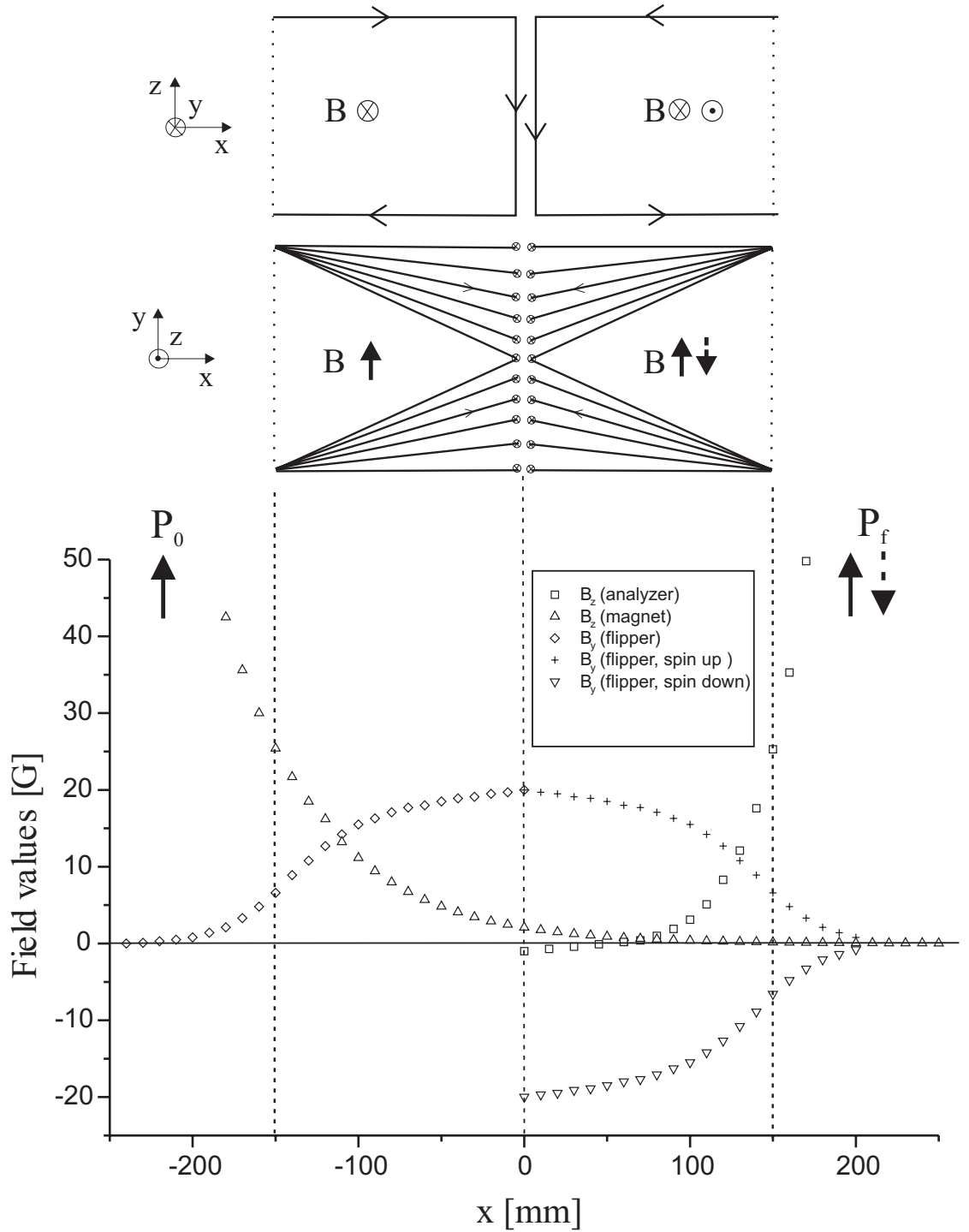
Figure 1.3: Spin flipper with the fields inside and outside the flipper. In the top and middle figure side and top view of the flipper is shown, respectively. The flipper is wound in such a way that it produces a field in the $\pm y$ direction. In the bottom figure, the fields inside and outside the flipper are shown. The fields outside are due to the stray fields of the magnet and the polarizer, respectively. The final polarization P_f is equal or antiparallel to the initial polarization P_0, dependent on the direction of the field in the y-direction in the second part of the coil.
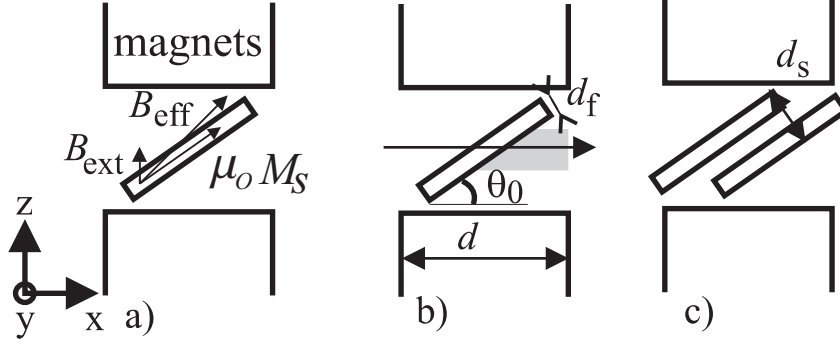
Figure 1.4: Schematic side views of the single and double foils (a) The effective induction $\vec{B}_{eff}$ is the vector sum of the in-plane local magnetic induction $\mu_0 M_s$ and the applied external field B_{ext}. Neutrons that traverse the foil will experience this effective induction $\vec{B}_{eff}$. (b) Definition of the angle θ_0, the thickness of the foil d_f and the length d of the pole shoes. The length that the neutrons traverse in the magnetic field after the foil (indicated with the gray area) depends on their height in the field. (c) A double foil consists of two foils mounted parallel at a distance d_s.

field B_{eff} which is the vector sum of the in-plane local magnetic induction $\mu_0 M_s$ and the applied external field B_{ext} as shown in Fig. 1.4a where M_s is the saturation magnetization. The value of the field is:

$$B_{eff} = \sqrt{(\cos(\theta_0)\mu_0 M_s)^2 + (\sin(\theta_0)\mu_0 M_s + B_{ext})^2} \qquad (1.7)$$

and its angle with the horizontal is:

$$\theta_{eff} = \arctan\left(\frac{\sin(\theta_0)\mu_0 M_s + B_{ext}}{\cos(\theta_0)\mu_0 M_s}\right). \qquad (1.8)$$

The polarization vector rotates in the foil over an angle:

$$\phi_f = c\lambda B_{eff}d_f/\sin(\theta_0) \qquad (1.9)$$

around this local induction, in which $d_f/\sin(\theta_0)$ is the path length through the magnetized foil. The rotation matrix R_f for the polarization vector can be calculated from these parameters.

1.5.1   Single foils to start and stop precession

When we calculate the precession inside the foil with the matrix R_f acting on the initial polarization in the z-direction, we find that the polarization

is turned into the horizontal plane, perpendicular to the applied field. As a consequence, the Larmor precession starts after the foil. The precession continues until the end of the field between the poles of the electromagnet which is perpendicular to the neutron beam. Thus a triangular precession region is created as shown in Fig. 1.4b.

The vertical polarization can be calculated with the zz-element of R_f:

$$P_{zz} = \sin^2(\theta_{eff}) \left(\cos(\phi_f) - 1 \right) + 1 \qquad (1.10)$$

In this way, it is possible to bring the vertical polarization vector to the horizontal plane by using a foil of an amorphous CoFeNi alloy with a thickness of $d_f = 30$ μm and $\mu_0 M_s = 0.55$ T mounted under an angle $\theta_0 = 41^0$ on a flat aluminum frame. The strength of the applied magnetic field has a noticeable effect on the flipping behavior of the magnetic foil. The foil is already saturated at a very small applied field.

1.5.2   Double foils as a π rotator

Two parallel foils spaced by a distance d_s (Fig. 1.4c) can function as a spin flipper by rotating the polarization by π radians around the x-axis. The transformation of the polarization vector is composed of three rotations: a rotation ϕ_f around the magnetization in the first foil, next a rotation in the space between the foils ϕ_s around the vertical magnetic field, and finally again a rotation ϕ_f around the magnetization in the second foil. The rotation between the foils is over an angle:

$$\phi_s = c\lambda B d_s / \sin(\theta_0) \qquad (1.11)$$

which is described by rotation matrix R_s. So, the matrix due to the double foil can be calculated:

$$R_d = R_f R_s R_f. \qquad (1.12)$$

The rotation in the space between the foils can be tuned, for example by varying B. The double foil is a π flipper when $d_s = 0.35$ mm, $\lambda = 0.245$ nm and $B = 53$ mT. The importance of the double foil is that it now works as a mirror for the polarization vector in the xz-plane which leaves the y-direction of the polarization vector unaffected.

1.6   The SESANS principle

In Fig. 1.5 the complete SESANS setup is shown. First the neutrons are polarized by the polarizer. By entering the first magnet, the polarization

vector is turned 90^0 by the single foil which acts as a $\pi/2$ flipper [10]. The double foil is a π flipper and the single foil in the third magnet stops the precession. If there is no scattering the total amount of precession in the precession areas denoted by a + sign will be equal to that with a - sign. This is the echo situation. The reason for this is simply that the length of path for unscattered neutrons in the + region is the same as in the - region. The single foil turns the polarization with 90^0 from the $x - y$-plane to the z direction. The flipper together with the analyzer is used to select the spin up or spin down state. Finally, the neutrons are counted by the detector.

When there is scattering, the length of the scattered and unscattered paths after the sample are not the same. This gives rise to a difference in precession angle $\Delta\varphi$, and therefore the polarization vector will make an angle $\Delta\varphi$ with the z axis when it is rotated over 90^0 by the single foil from the $x - y$ plane to the z direction. In order to calculate the difference in precession we must first calculate the length of these paths. Lets suppose a right handed coordinate system with the x-axis in the neutron beam direction on the sample. The unscattered beam is defined by the angles θ_1 and ϕ_1 and the scattered beam by θ_2 and ϕ_2. These angles are the usual spherical polar coordinates with the pole angles defined as the complementary angle to the z-axis and the azimuthal angles are defined with respect to the x-axis. The equation of the path for the unscattered beam can be written as:

$$\mathbf{r_u} = \mathbf{e_u}t \tag{1.13}$$

where t is a scalar and $\mathbf{e_u}$ is the spherical unit vector given by:

$$\mathbf{e_u} = (\cos(\theta_1)\cos(\phi_1), \cos(\theta_1)\sin(\phi_1), \sin(\theta_1)) \tag{1.14}$$

The length of the path is $|\mathbf{r_u}| = t$. The equation of the plane of the last foil is given by:

$$z = \tan(\theta_0)(x - s_x) \tag{1.15}$$

where s_x is the distance from the sample to the last foil, θ_0 the angle between the foils and the horizontal direction as shown in Fig.1.5. The x and z coordinates in Eq.1.14 and Eq.1.15 are the same when the path intersects the plane of the foil. By substituting the x and z components of Eq. 1.14 in Eq. 1.15 we can solve t which is the length from the sample to the point of intersection of the foil by the path. This length for the unscattered neutrons t_{u1} is given by:

$$t_{u1} = \frac{s_x \tan(\theta_0)}{\cos(\phi_1)\cos(\theta_1)\tan(\theta_0) - \sin(\theta_1)} \tag{1.16}$$

The length from the sample to the straight part of the precession area in magnet 3, t_{u2}, can be obtained by Eq. 1.16 by taking the limit $\theta_0 \to \pi/2$ and replacing s_x by $s_x - d/2$:

$$t_{u2} = (s_x - d/2)\sec(\varphi_1)\sec(\theta_1) \tag{1.17}$$

The length over which precession takes place for the unscattered beam, Δt_u is the difference between t_{u1} and t_{u2}: $\Delta t_u = t_{u1} - t_{u2}$. In the same way we can define the length over which precession takes place for the scattered beam as Δt_s which is obtained from Δt_u with the following changes: $\theta_1 \to \theta_2$ and $\varphi_1 \to \varphi_2$

The difference in precession is then given by Eq.1.6 for a homogenous field B as:

$$\Delta\phi = c\lambda B(\Delta t_s - \Delta t_u) \tag{1.18}$$

The scattering angles are defined by $\theta = \theta_2 - \theta_1$ and $\phi = \phi_2 - \phi_1$. The divergence of the beam is neglected when $\theta_1 = \phi_1 = 0$. By using this in Eq. 1.18 and making a Taylor expansion of (θ, ϕ) around $(0, 0)$ one obtains up to first order [6]:

$$\Delta\phi = c\lambda Bs_x \cot(\theta_0)\theta = Q_z \frac{c\lambda^2 B \cot(\theta_0)s_x}{2\pi} = Q_z z \tag{1.19}$$

where we used $Q_z = k_0\theta = \frac{2\pi}{\lambda}\theta$, the z-component of the wave vector transfer, θ the scattering angle and

$$z = \frac{c\lambda^2 B \cot(\theta_0)s_x}{2\pi}. \tag{1.20}$$

The sample does not scatter over one angle but over all angles according to the scattering power of the sample $F^2(\mathbf{Q})S(\mathbf{Q})$ where $F(\mathbf{Q})$ is the form factor and $S(\mathbf{Q})$ the structure factor. The polarization can be written as:

$$P(z) = 1 - \sigma t + \sigma G(z)t \tag{1.21}$$

with:

$$G(z) = \frac{1}{\sigma k_0^2} \int_{-Q_{zm}}^{Q_{zm}} \int_{-Q_{ym}}^{Q_{ym}} \frac{d\sigma(\mathbf{Q})}{d\Omega} \cos(Q_z z) dQ_z dQ_y. \tag{1.22}$$

Here σ is the scattering probability per unit length of thickness that contributes to the detector intensity:

$$\sigma = \frac{1}{k_0^2} \int_{-Q_{zm}}^{Q_{zm}} \int_{-Q_{ym}}^{Q_{ym}} \frac{d\sigma(\mathbf{Q})}{d\Omega} dQ_z dQ_y. \tag{1.23}$$

The integration boundaries are determined by the critical reflection angle
of the polarizer and analyzer mirrors in the y-direction and the acceptance
angle of the detector in the z-direction. This leads to $Q_{ym} = 0.13$ nm^{-1} and
$Q_{zm} = 0.94$ nm^{-1} in the setup used in the Delft reactor [6]. The scattering
cross-section is given by:

$$\frac{d\sigma(\mathbf{Q})}{d\Omega} = \eta(\Delta\rho)^2 F^2(\mathbf{Q})S(\mathbf{Q}). \tag{1.24}$$

where η is the volume fraction and $\Delta\rho$ the scattering length density difference
between the particle and solvent. In Eq.1.21, σt gives the fraction of scattered
neutrons and $(1 - \sigma t)$ gives the fraction of unscattered neutrons.

1.7   Multiple scattering

If multiple scattering is present the formulae are somewhat more complicated
and (1.21) should be written as [11]:

$$P(z) = 1 - s_t + G'(z,t) \tag{1.25}$$

with s_t the total cross-section of the sample and $G'(z,t)$ representing the
fraction of the beam modified in polarization by the changed transmission
angle. The scattering in the sample can be thought to be built up of the
scattering processes taking place along an individual path. Let us assume
that n scattering events happen, with the probability for one such event equal
to ρ_n. The chance is given by [12]:

$$\begin{aligned}
\rho_n &= \frac{t^n \int \int dQ_{1y}dQ_{1z}\frac{d\sigma}{d\Omega}(Q_1) \int \int dQ_{2y}dQ_{2z}\frac{d\sigma}{d\Omega}(Q_2)... \int \int dQ_{ny}dQ_{nz}\frac{d\sigma}{d\Omega}(Q_n)}{k_0^{2n}1 \times 2 \times ... \times n}T \\
&= \frac{(\sigma t)^n}{n!}T
\end{aligned}$$

with:

$$Q_1 + Q_2 + ... + Q_n = Q \tag{1.26}$$

and T is the transmission of un-scattered neutrons given by:

$$T \equiv 1 - s_t \tag{1.27}$$

The total scattering is found by summing over all path probabilities ρ_n:

$$s_t = \sum_{n=1}^{\infty} \rho_n = \sum_{n=1}^{\infty} \frac{(\sigma t)^n}{n!}T = T(e^{\sigma t} - 1) = 1 - e^{-\sigma t} \tag{1.28}$$

and thus $T = \exp(-\sigma t)$. Let us now evaluate the second term $G'(z, t)$ on the right hand side of (1.25). The total wave vector transfer, Q_z, in the cosine term of this equation is the sum of all individual transfers according (1.26) occurring during the passage in one path through the sample and in particular the cosine term, $\cos(Q_z)$, can be written as:

$$\cos(Q_z) = \cos(Q_{1z})\cos(Q_{2z})...\cos(Q_{nz}) \qquad (1.29)$$

+ odd terms in Q_1, Q_2 and Q_n. In the integrals over Q_i the odd terms in Q_i do not contribute and can be omitted. In a similar way as for the total scattering derivation in and (1.26) to (1.28) we find:

$$
\begin{aligned}
\rho_n' &= \frac{t^n \int \int dQ_{1y}dQ_{1z} \frac{d\sigma}{d\Omega}(Q_1)\cos(Q_{1z}z)}{k_0^{2n}1 \times 2 \times ... \times n} \\
&\quad \times \int \int dQ_{2y}dQ_{2z} \frac{d\sigma}{d\Omega}(Q_2)\cos(Q_{2z}z) \\
&\quad \times ... \int \int dQ_{ny}dQ_{nz} \frac{d\sigma}{d\Omega}(Q_n)\cos(Q_{nz}z) \times T \\
&= \frac{(\sigma G(z)t)^n}{n!}T
\end{aligned}
$$

$$(1.30)$$

and:

$$G'(z, t) = \sum_n \rho_n' = \sum_{n=1} \frac{(\sigma G(z)t)^n}{n!}T = T(e^{\sigma G(z)t} - 1). \qquad (1.31)$$

Substituting this result in (1.25) we find for $P(z)$ in case of multiple scattering:

$$P(z) = T + G'(z, t) = Te^{\sigma G(z)t} = e^{\sigma t(G(z)-1)} = T^{1-G(z)} \qquad (1.32)$$

or:

$$G(z) = 1 - \frac{\ln(P(z))}{\ln(T)}. \qquad (1.33)$$

This equation shows that there is a one to one relation between the measured polarization and the correlation function $G(z)$ independent of possible multiple scattering, provided the level s_t or T can be defined. That means that one does not need to limit the number of scattering processes of the neutrons in transmission through the sample, in marked contrast to conventional SANS where the sample thickness must be chosen such as to avoid multiple scattering. This is a great advantage of the SESANS technique in view of measuring statistics.

If one does not know the transmission or the total amount of scattering, it is still possible to scale the depolarization with the thickness to obtain the shape of the correlation function:

$$\frac{\ln(P(z))}{t} = \sigma(G(z) - 1) \qquad (1.34)$$

1.8 Different options for SESANS

There are several possibilities to realize a SESANS instrument. So far we have discussed extensively the foil option. In Fig. 1.6 four possible options of SESANS are shown. The first one, Fig. 1.6.a is the SESANS option with three foils which has already been discussed. The advantage of this option is that the inclination angle θ_0 can be made very small which increases the spin-echo length tremendously. Another advantage is that the fields are in the same direction throughout the setup. There are three disadvantages: Firstly, the foils work for a certain wavelength. Secondly, the line integrals have to be corrected with external coils. Thirdly, the accuracy for setting θ_0 increases with decreasing angle. This can be understood with the following: By differentiating the spin-echo length, Eq. 1.20, with respect to θ_0 we can write:

$$\Delta\theta_0 = -\sin(\theta_0)^2 \frac{2\pi}{c\lambda^2 B s_x} \Delta z \qquad (1.35)$$

This means that an allowable error $\Delta\theta_0$ in the inclination angle θ_0 becomes small when θ_0 is decreased in order to increase the spin-echo length. If $\theta_0 = 45^0$ is compared with $\theta_0 = 5.5^0$ we obtain:

$$\Delta\theta_0(\theta_0 = 5.5^0) = \frac{\sin(5.5^0)^2}{\sin(45^0)^2} \Delta\theta_0(\theta_0 = 45^0) = \frac{\Delta\theta_0(\theta_0 = 45^0)}{54}. \qquad (1.36)$$

So, with $\theta_0 = 5.5^0$ the angle θ_0 must be set 54 times more accurate than with $\theta_0 = 45^0$ to obtain the same resolution in z.

The wedge option is shown in Fig. 1.6.b. The poles of the magnets are shaped like wedges which create triangular precession areas as shown in the figure. The disadvantages of this option are that firstly, the line integral must be corrected with external coils. Secondly, the magnetic field in the first part of the setup is opposite to the field in the second part. Thirdly, it is difficult to change the angle θ_0 since this is determined by the magnet poles. A strong advantage of such an option is that it is applicable to all wavelengths. If the sample is positioned in the middle of the setup the spin-echo length is given by:

$$z_{wedge,1} = \frac{c\lambda^2 B \cot(\theta_0)(d + 2L)}{2\pi}, \qquad (1.37)$$

Polarizer

Magnet 1

Single foil

a neutron path

Magnet 2

Double foil

B

Magnet 3

Single foil

flipper

analyzer

Detector

Sample

Scattered beam

diaphragm

θ_0

$+$

L

X

$-$

L

d

S_x

ϕ

Figure 1.5: Cross-section of the SESANS setup. The neutrons are polarized by the polarizer in the z direction. The state of the polarization vector at different stages of the setup is drawn in the middle and the bottom figure. The middle figure is for the unscattered neutrons whereas the bottom one for the scattered. By passing through the single foil in the first magnet the polarization is turned by $\pi/2$ from the z direction to the $x-y$ plane. The polarization vector precesses over some angle in the triangles denoted with a + sign at the time it reaches the double foil. The double foil mirrors the polarization vector in the $x-z$ plane and consequently after traversing the double foil the polarization vector is mirrored. When the polarization vector reaches the single foil in the third magnet it precesses the same amount in the - regions a in the + regions. Finally the polarization is turned from the $x-y$ plane to the z direction. When the neutrons scatter the amount of precession in the + regions is not equal to the precession in the - region. There is a different amount of precession ϕ.
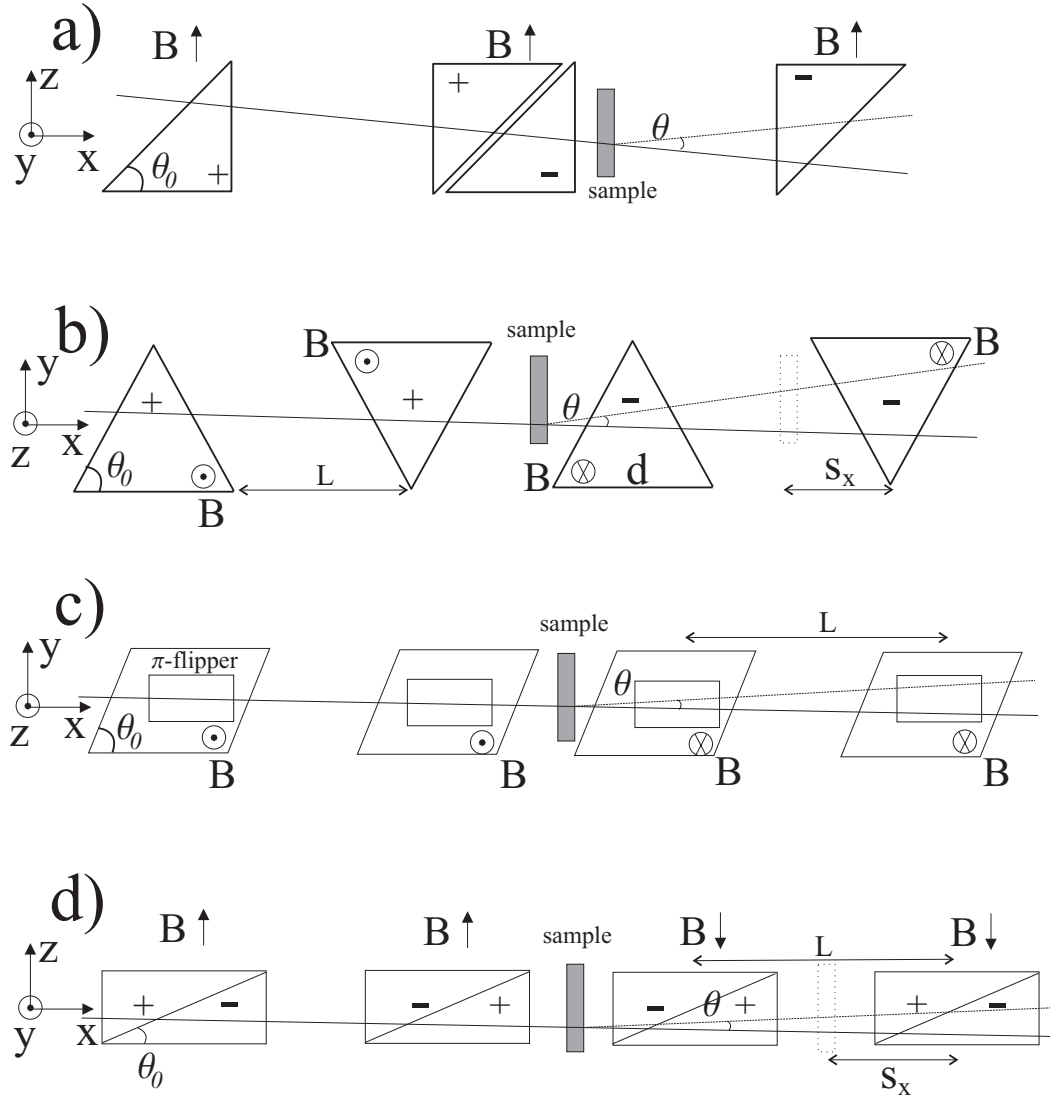
Figure 1.6: Different options with which a SESANS instrument can be realized. a) SESANS with three foils. The outer foils work as $\pi/2$ flipper whereas the middle one works as a π flipper. b) SESANS with wedges. The poles of the magnets are shaped as wedges which create triangular precession regions. c)SESANS with resonant field option. The poles of the magnets are shaped as parallelograms. π flippers are placed between the poles. d)SESANS with four foils which work as π flipper.

whereas if it is positioned between the third and fourth precession area it is given by:

$$z_{wedge,2} = \frac{2s_x c \lambda^2 B \cot(\theta_0)}{2\pi},$$

(1.38)

An comparison of Eq. 1.20 and Eq. 1.38 shows that with the wedge option the spin-echo length is two times larger than with the foil option.

In Fig. 1.6.c the resonant field option is shown [13]. The magnet poles are shaped like parallelograms which create the SESANS effect. π-flippers are placed between the magnet poles which consist of solenoids with the field in the neutron beam direction. A sinusoidally changing current is passed through the solenoids of which the frequency matches the energy of zeeman splitting of the spin states. The disadvantages are twofold. Firstly, it is difficult to change θ_0. Secondly, the fields are in the opposite direction for the first and second part of the setup. There are two advantages: Firstly, the π flippers work for all wavelengths [14]. Secondly, because of the π flipping in the middle of each precession area the line integral errors at the entrance and exit of each magnet cancel each other. Therefore, there are no correction coils needed. The spin-echo length is given by [15]:

$$z_{resonant field} = \frac{2Lc\lambda^2 B \cot(\theta_0)}{2\pi}.$$

(1.39)

The last option is shown in Fig. 1.6.d. There are four dipole magnets in which inclined foils are placed which work as π flippers. In this way, eighth triangular shaped precession regions are created. The advantage of this option is that the line integral is automatically corrected for each magnet due to the π flipping in the middle. Additionally, the spin-echo length can be largely increased by decreasing the inclination angle θ_0. A disadvantage is that the fields are oppositely oriented for the first and second part of the setup and the foils work for one wavelength. Furthermore, the allowable error in θ_0 becomes small with increasing θ_0, Eq.1.35. If the sample is positioned in the middle of the setup the spin-echo length is given by:

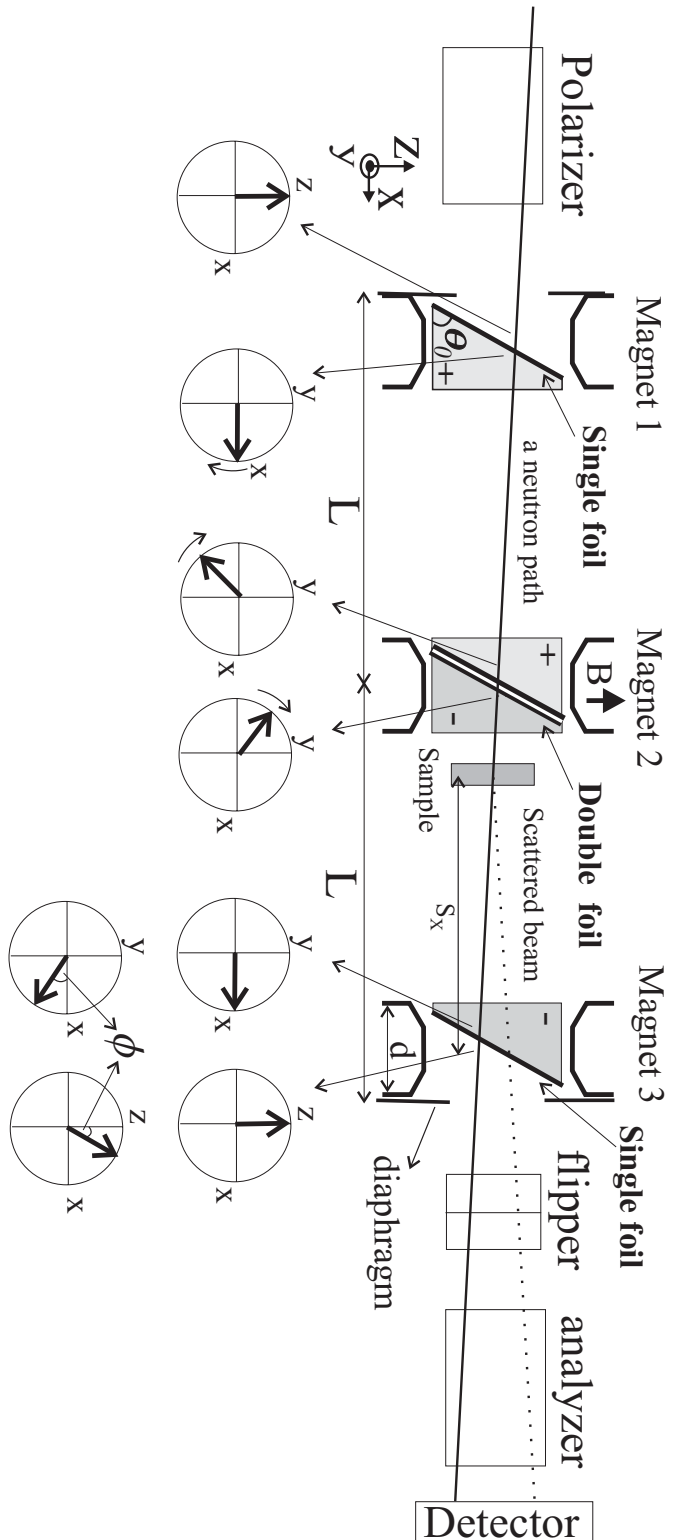$$z_{foil,1} = \frac{2Lc\lambda^2 B \cot(\theta_0)}{2\pi},$$

(1.40)

whereas if it is positioned between the third and fourth precession area it is given by:

$$z_{foil,2} = \frac{2s_x c \lambda^2 B \cot(\theta_0)}{2\pi}.$$

(1.41)

The spin-echo length is increased by a factor of two in comparison with the three foil option.

	three foils	wedges	resonant field	four foils
λ	one λ	all	all	one λ
spin-echo length	z^*	$2z^*$	$2z^*$	$2z^*$
zero field transition	no	yes	yes	yes
line integral	external coils	external coils	automatically corrected	automatically corrected
adjustment of θ_0	easy	difficult	difficult	easy

Table 1.1: Advantages/disadvantages of the four options with which SESANS can be realized. The zero field transitions has to do with when the magnetic fields are in the same or opposite direction in the first or second part of the setup.

In Tabel 1.1, a summary of the advantages/disadvantages of the four SESANS options is given. When the three and four foil options are compared the four foils option is better except for the zero field transition. However, this is not a serious problem. It can be solved with a field stepper placed at the zero field transition point. A choice between four foils and resonant field option is choosing between a large z range or high intensity, respectively. The wedge option compared to resonant field and four foils has the disadvantage that the line integral must be corrected and that it is difficult to adjust θ_0. However, the line integral can be corrected very well with external coils as will be shown in chapter 3. So, the only disadvantage of this option is the θ_0 adjustment. On the other hand it works for all wave lengths like the resonant field option.

Chapter 2

Magnetic design of a Spin-Echo Small-Angle Neutron Scattering instrument

2.1 Introduction

A photo of the SESANS setup with the four foil option is shown in Fig. 2.1. It can consist of two symmetrical parts containing dipole electromagnets with inclined foils in it. The amount of precession in each magnet is a linear function of the height of the neutron path in the magnet. In order to preserve this linearity the fields produced by the magnets must be homogeneous enough in the magnets around the regions where this linear labelling occurs. In this paper the design parameters for a homogeneous SESANS magnet will be calculated. Line integral homogeneity is another important requirement for the SESANS magnet. The origin of these inhomogeneities is explained.

The magnetic fields in the SESANS instrument are perpendicular to the neutron direction contrary to conventional spin-echo setups [2] where the fields are parallel to the neutron direction. In the latter case cylindrical coils are used with the cylinder axis parallel to the beam axis. The magnetic field distribution for such coils can be calculated analytically rather than integrating the Biot-Savart law numerically [16]. In our case we use electro

Figure 2.1: Photo of the SESANS setup with four foils. Various components are indicated.

magnets containing iron parts which forces us to use numerical calculations.

In the literature there is considerable knowledge on design parameters for insertion devices for synchrotron radiation and NMR magnets. In the case of NMR, one is interested in a homogenous field around the sample volume of approximately $20 \times 20 \times 20$ mm^3. By using shim coils one can obtain 3 parts per billion field homogeneity [17]. One is not interested in the field distribution outside the sample volume due to these shim coils which is not homogenous. If in SESANS such shim coils were used around the foils to homogenize the field, the line integral outside the foil region would be spoiled due to the inhomogeneities there, created by the shim coils.

In the case of insertion devices such as wigglers and undulators, one is interested in the integrated homogeneity of the magnetic field vector along the electron trajectory [18]. However, in SESANS the important quantity is the integrated homogeneity of the absolute value of the magnetic field along the neutron trajectory. Moreover, the line integral must be homogenous over the whole beam cross-section. There are also reports about insertion devices for homogenizing the field by modifying the pole face. In [19, 20, 21], it is reported that by putting metal plates with a high μ against the pole faces the magnetic field can be homogenized. In [19], it is argued that the central field would decrease if the pole width would be increased. In this paper we will show that the value of the central field is only dependent on the distance between the pole faces and the current. Therefore, the pole width will be increased to homogenize the field.

In the SESANS instrument guide fields have to be used in order to preserve the polarization of the neutrons between the magnets. The necessary homogenous field can be produced by coils. The required parameters for such coils will be calculated.

2.2   Calculation of the magnetic fields

The magnetic field calculations were performed with two different programs: Poisson Superfish code of the Los Alamos National Laboratory [22] and Radia [23] from the ESRF in Grenoble, France. Poisson is a 2D code that uses finite element methods to solve the problem. On the other hand, Radia is a 3D code. It uses finite difference methods to solve the problem. In this method of solution, only the actual material regions have to be segmented. Therefore, the space between a point where the field value is required and the material is not segmented. This saves a lot of computation time in solving 3D geometries. However, in situations where 2D calculations were sufficient we used the 2D program instead of the 3D program. The reason for this is
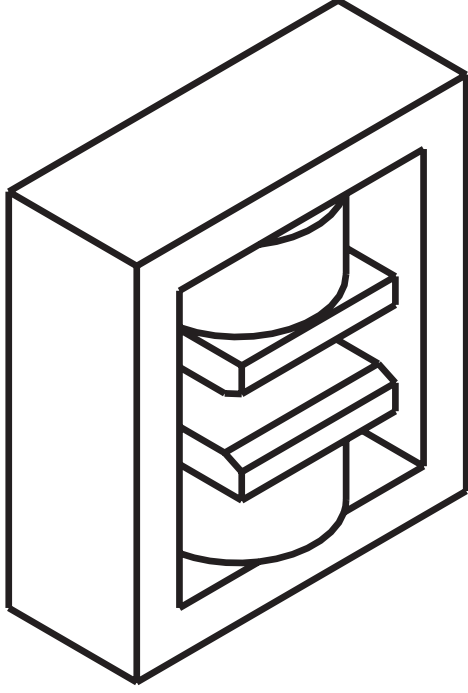
Figure 2.2: 3D picture of a SESANS magnet with skewed pole faces.

twofold. Firstly, it is not possible in Radia to switch to 2D. Secondly, the required time in order to calculate the magnetic field for geometries with pole faces as shown in Fig.2.2 increased tremendously in the 3D calculations in comparison with magnets with no pole faces.

2.3   Magnetic field homogeneity

In the center of the magnet in a volume of $30 \times 30 \times 30$ mm^3 the magnetic field homogeneity should be better than 1.3 G to maintain a good polarization [24]. In Fig. 2.3 one can see the cross-section of a quarter part of the magnet in Fig.2.2 which is used in the simulations. The short-circuiting yoke is in the actual set-up in the y-direction but it is drawn in the $x - z$ plane because the simulations and the calculations are done in two dimensions. Various parameters in the magnet in Fig. 2.3 are varied to study the effect on the line integral and field homogeneity.

In Fig. 2.4 the field inhomogeneity ΔB in the x and z directions are plotted as a function of x_p. As a measure for ΔB the difference of the field values at $x = 1.5$ cm, $z = 1.5$ cm and $x = 0$ cm, $z = 0$ cm are taken. At these points, the fields differ the most from each other. The magnet is one
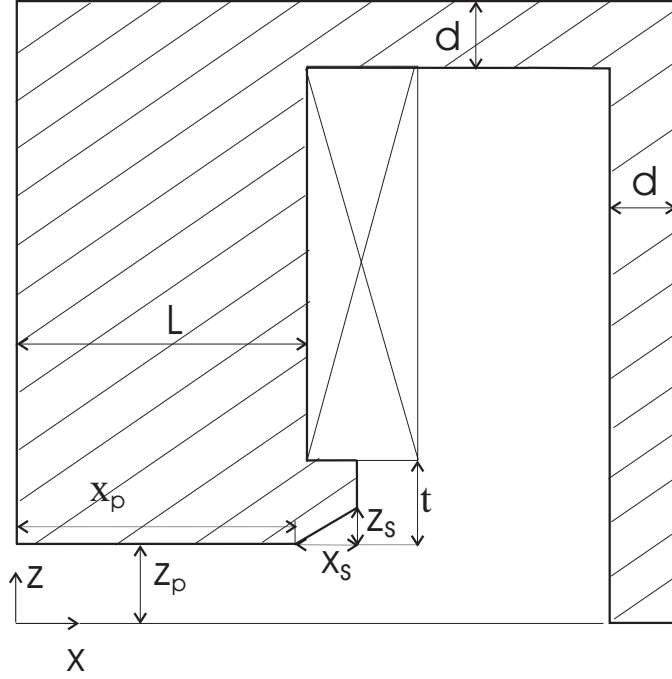
Figure 2.3: Quarter of the cross-section of the magnet in the $x - z$ plane as used in the simulations. Various parameters are indicated.

with a rectangular pole face, i.e. $x_s = 0$, $L = x_p$, $d = 2$ cm and $z_p = 3$ cm. The simulations are done in cylindrical symmetry with $B(0,0) = 2000$ G. Therefore the x axis can also be read as the y axis. We can see from this figure that with $x_p = 9$ cm the magnet is homogenous enough in the three directions.

2.4   Saturation effect and thickness of the yoke and core

In the previous section we concluded that x_p had to be at least 9 cm. Having the same value for the radius of the core L would make this rather heavy. To save weight one might decrease L. However L cannot be chosen too small because then the iron saturates.

In decreasing L one should keep in mind that x_p should be 9 cm in order to preserve the homogeneity of the field. Another important point here is the thickness of the pole face, t. If this is too small the flux in the iron core cannot be distributed smoothly enough through the pole face in the $x - y$ direction which leads to inhomogeneities. If $L = 5$ cm $x_p = 9$ cm, $x_s = 0$ cm
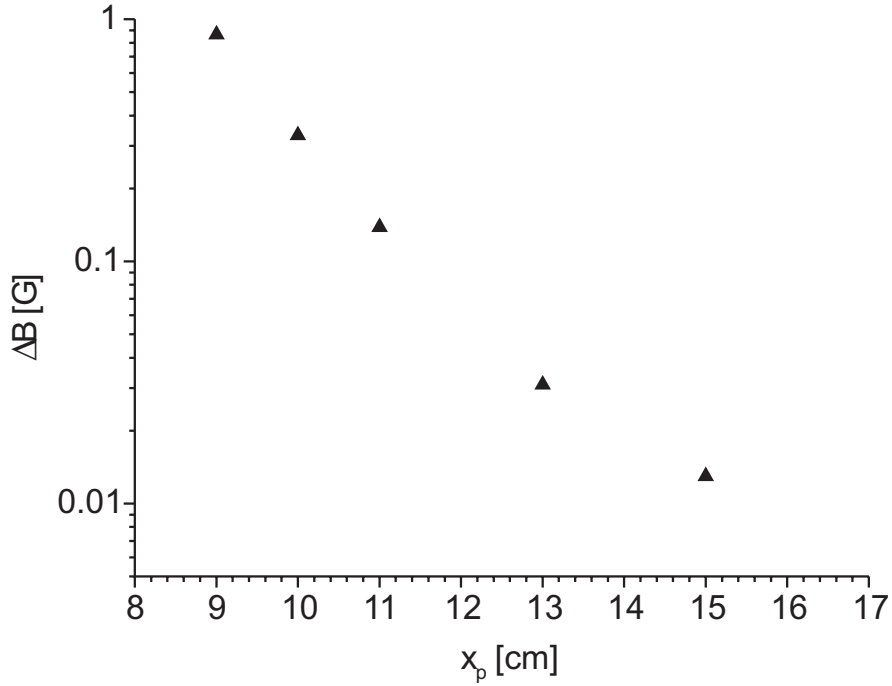
Figure 2.4: Difference between the magnetic fields at $x = 1.5$ cm, $z = 1.5$ cm and $x = z = 0$

and $t = 1$ cm then $\Delta B = 15.1$ G in a volume of $30 \times 30 \times 30$ mm^3 around the center of the magnet. When we increase t from 1 cm to 3 the inhomogeneity becomes 1.9 G which is sufficient.

The purpose of the yoke is to short-circuit the flux. However, if the cross-section of the yoke perpendicular to the flux lines is too small the yoke gets saturated. This is a situation which has to be avoided. For an estimate of the yoke thickness, consider the iron in saturation. The cross-section of the iron core is $\pi \times L^2$ and that of the yoke is d, see Fig. 2.3. Here we have taken the yoke in the y direction. The width in the x direction is l and the flux in the iron core is $\phi_{core} = \pi L^2 B_{core}$. The flux in the yoke is $\phi_{yoke} = dl B_{yoke}$ where B_{core} and B_{yoke} are the magnetic induction in the core and yoke, respectively. From conservation of flux we can write; $\phi_{core} = 2 \times \phi_{yoke}$. This gives for B_{yoke} in order not to be saturated when B_{core} approaches saturation:

$$B_{yoke,sat} \geq \frac{\pi L^2 B_{iron,sat}}{2dl} \tag{2.1}$$

where $B_{yoke,sat}$ and $B_{iron,sat}$ are the fields in the yoke and core, respectively,
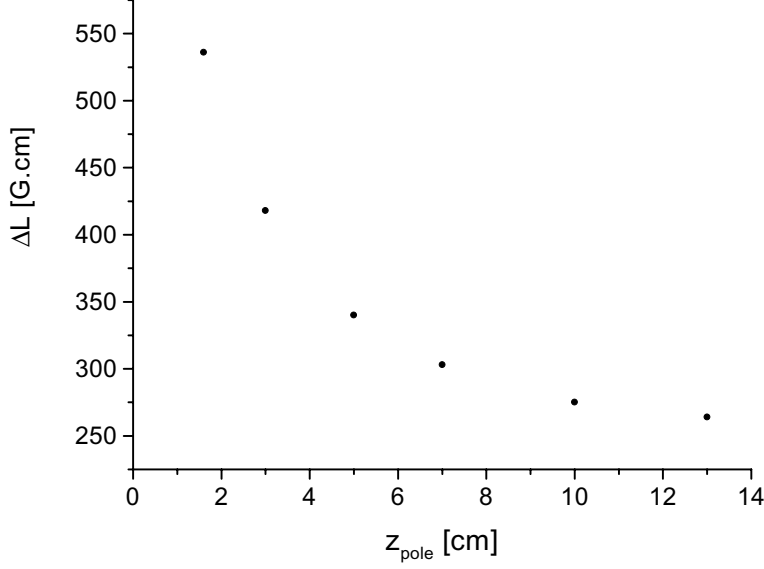
Figure 2.5: Difference of the line integral evaluated at $z = 1.5$ cm and $z = 0$ cm as a function of the gap distance. The other magnet parameters are: $L = 8$ cm, $x_s = 3$ cm, $x_p + x_s = L$ and $z_s = 1$ cm.

approaching saturation. The minimum thickness of the yoke is then:

$$d \geq \frac{\pi L^2}{2l} \qquad (2.2)$$

From simulation we obtain that the field in the core is 10 kG for a field of 2000 G in the center of the magnet and with $L = 6$ cm and $t = 3$ cm. This can also be reasoned by equating the flux in the core to the flux in the gap. This gives $L \geq l\sqrt{\frac{2000}{\pi B_{core}}}$. For $l = 18$ cm and $B_{core} = 10$ kG, $L = 4.5$ cm and a square pole face

So, the minimum thickness of the yoke is from Eq. 2.2, $d = 3.1$ cm for $L = 6$ cm and $l = 18$ cm.

2.5 Line integral homogeneity

The total amount of precession which a neutron performs when it follows a path, l, through a magnetic field is given by:

$$\phi = c\lambda \int B dl, \qquad (2.3)$$
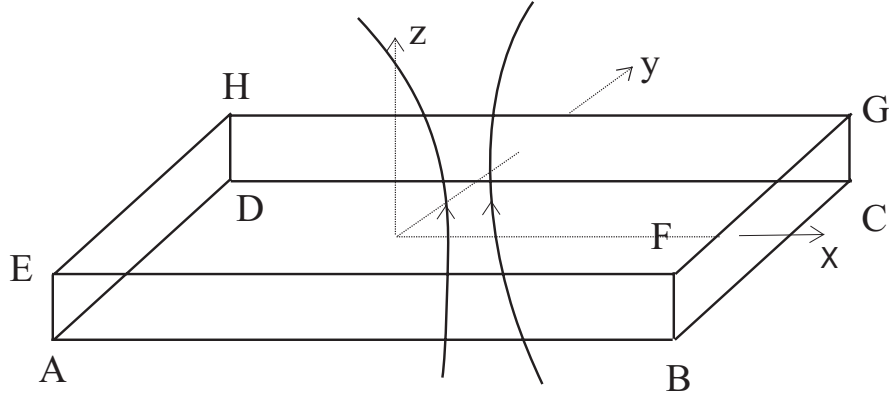
Figure 2.6: Rectangular box for calculation of the flux through its surface.

where $c = 4.63 \times 10^{14}$ G.cm^{-2}, λ is the wavelength and B the magnetic field. For a horizontal path through the middle of the magnet, Fig. 2.3, and the end top part of the magnet the difference in the line integral becomes

$$\Delta(\int B dx) = \frac{\Delta\phi}{c\lambda}. \tag{2.4}$$

If we want the polarization better than 0.98 then $\Delta\phi$ of the total setup must be smaller than 0.2 rad., since $\cos(0.2) = 0.98$. Then:

$$\Delta(\int B dx) \leq 2.2 \, \text{G.cm}. \tag{2.5}$$

for λ=0.2 nm [25].

The difference in the line integral can be written more specifically as:

$$\Delta(\int B dx) = \int \left(\sqrt{(B_x'^2 + B_z'^2)} - B_z \right) dx. \tag{2.6}$$

The primes denote the field values at some height $z = z_1$ for a horizontal path along x. The unprimed fields are those at $z = 0$. Because of symmetry at $z = 0$, $B_x = 0$. The field in the z direction is much larger than the field in the x direction. Therefore, we can expand the first term in Eq. 2.6. We can then write:

$$\Delta(\int B dx) = \int (B_z' - B_z) dx + \int \frac{B_x'^2}{2B_z'} dx. \tag{2.7}$$

Now we will use the conservation of flux to show that the first term in Eq. 2.7 vanishes. The conservation of flux reads as $\nabla \cdot \overrightarrow{B} = 0$. This can also be written as a surface integral, i.e $\oint \overrightarrow{B} \cdot d\overrightarrow{O} = 0$ where $d\overrightarrow{O}$ is an infinitesimal
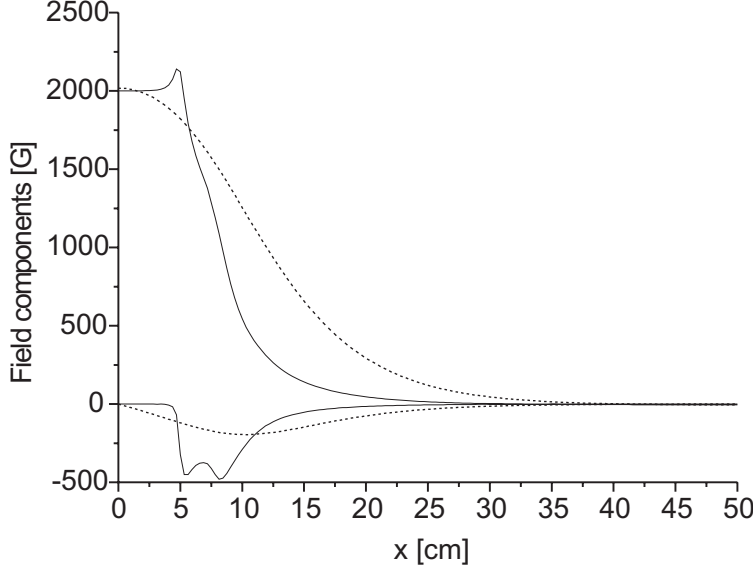
Figure 2.7: Field components B_x and B_z at $z = 1.5$ cm for two half pole distances. The continuous curves are at $z_p = 1.6$ cm, whereas the dashed curves are at $z_p = 10$ cm. The negative and positive valued curves are the x-components and the z-components, respectively.

surface element. We choose as integration area the surface of the rectangular box in Fig. 2.6 whereby the magnet is not drawn. The bottom face of the rectangular box, $ABCD$, is in the $x - y$ plane at $z = 0$ and the top face, $EFGH$ is also in the $x - y$ plane but at $z = z_1$. The length of the rectangular box in the x direction is much larger than the length of the magnet L. Conservation of flux can now be written as:

$$\oint \overrightarrow{B} \cdot d\overrightarrow{O} = \int_{EFGH}(B'_z - B_z)dxdy + \int_{FBCG}(B_{2,x} - B_{1,x})dydz + \int_{DCGH}(B_{4,y} - B_{3,y})dxdz.$$

$$(2.8)$$

Here $B_{1,x}$ and $B_{2,x}$ are the x components of the fields at the planes $EADH$, $FBCG$, respectively. $B_{3,y}$ and $B_{4,y}$ are the y components of the fields at the planes $ABFE$, $DCGH$, respectively. The last term in Eq. 2.8 vanishes, because $B_{3,y} = B_{4,y} = 0$. The second term is also very small if one takes the rectangular box sufficiently large. Therefore, Eq.2.8 reduces to:

$$\oint \overrightarrow{B} \cdot d\overrightarrow{O} = 0 = \int_{EFGH}(B'_z - B_z)dxdy = \int dy \int (B'_z - B_z)dx, \qquad (2.9)$$

because B_z has no y dependency. Combining this with Eq. 2.7 gives:

$$\int (B'_z - B_z)dx = 0, \text{ and } \Delta(\int B dx) = \int \frac{B'^2_x}{2B'_z}dx. \qquad (2.10)$$

Therefore, inhomogeneities in the z component of the field will not contribute to the line integral inhomogeneities. Furthermore, the line integral is proportional to the square of the x-component of the magnetic field. This means that it is important in the design to reduce these x-components.

2.5.1   Dependence on pole gap

In Fig. 2.5 the difference of the line integral $\int |\overrightarrow{B}| dx$ at $z = 1.5$ cm and $z = 0$ cm is plotted as a function of the half pole distance. Increasing the pole gap by a factor 8 reduces the line integral difference only by a factor of 1.8. Therefore increasing the pole gap in order to fulfil the requirement on the line integral difference will not help much. Increase of the pole gap distance has also a disadvantage. The field produced by the magnet can be approximately written by Ampere's Law as $B = I/(2 \times z_{pole})$. Therefore, increasing the pole gap distance will lower the produced field. It is also clear that the magnitude of B is independent of the width of the pole faces.

To get a better understanding of what is happening the field components for two pole distances are plotted in Fig. 2.7. When the pole distance increases the x component decreases, but as one can see from Fig. 2.7 it gets extended. So the integral in Eq. 2.10 does not decrease enough to make the difference in the line integral small.

2.5.2   Dependence on pole angle

The next parameter which has to be determined is the pole angle. This angle is defined by x_s and z_s. There will be a strong B_x if the pole angle is 90^0 i.e. $x_s = 0$. Therefore, in order to reduce the line integral inhomogeneities there should be a smooth transition. The situation where x_s is small and z_s is large and *vice versa* leads to the same configuration. So there is an optimum x_s, z_s ratio. Indeed, in Fig. 2.8 one can see the variation of the difference of the line integral as function of the slope z_s/x_s. For zero and large slope the line integral is the same. At a slope of 0.49 the line integral is minimal. In these simulations x_s is kept constant at 3 cm while z_s is varied and $x_p + x_s = L$.

2.5.3   Discussion

By careful design the inhomogeneity of the line integral difference is still 550 G.cm. This value is still far away from the required 2.2 G.cm. It is not possible to reduce the line integral differences further by choosing the optimal pole angle. The remaining inhomogeneity will be reduced by two external coils. Therefore, it is preferable to keep the starting value of the line integral
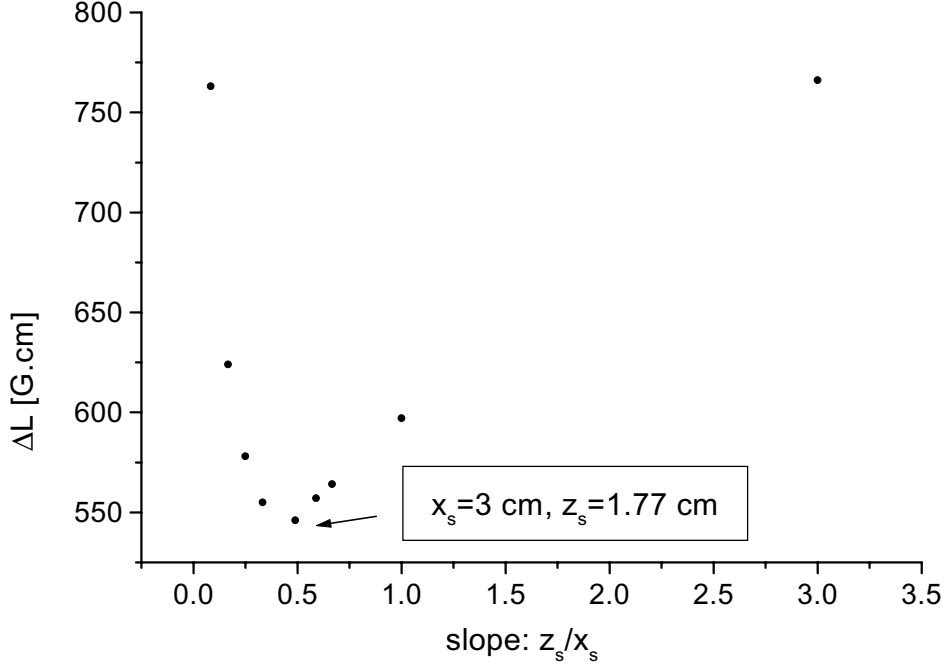
Figure 2.8: Dependency of the line integral difference on the slope of the pole face.

errors as small as possible because then the current for the correction coils will also be small. The first coil consists of four current carrying bunches of wires placed along the mean beam trajectory [25]. These wires create a quadratically changing fields in the perpendicular direction to the neutron beam over the beam cross-section. This coil actually transforms the line integral inhomogeneity from one perpendicular direction to the other. The second coil has a parabolic cross section. This will correct the remaining inhomogeneity. In this way it is possible to increase the polarization from 0.15 to 0.82 for a beam cross-section of 10×15 mm^2 [26].

2.6   Measurements

Measurement of the magnetic field B along the x-axis at $y = z = 0$ in a SESANS magnet designed according to the calculations is shown in Fig. 2.9. The various parameters are: $t = 3.8$ cm, $z_s = 0.93$ cm, $x_s = 2$ cm, $x_p = 7.5$ cm, $L = 5$ cm and $d = 5$ cm. Some parameters are somewhat larger
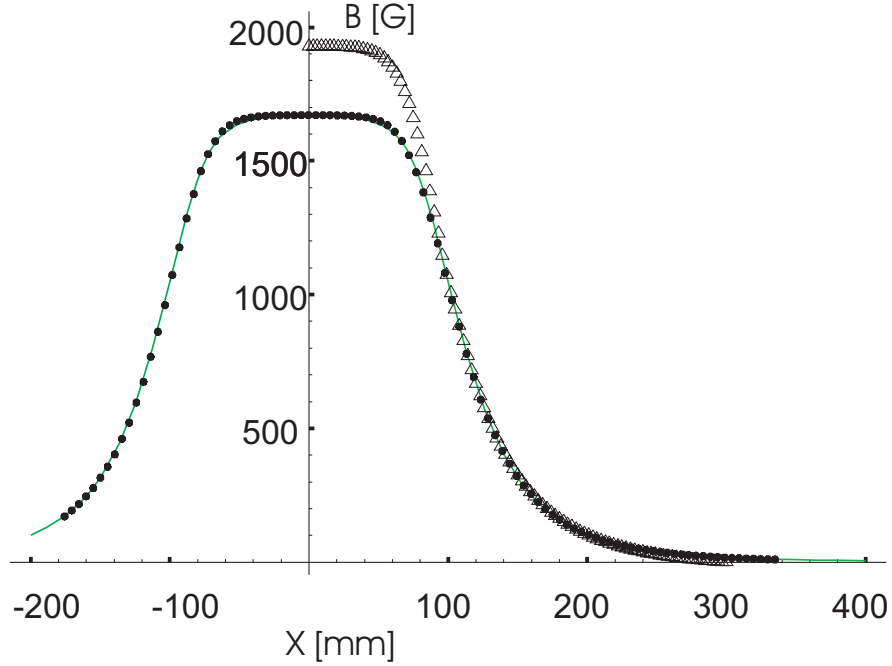
Figure 2.9: Measurment and simulation of the field with 2-D and 3-D geometry along the x axis at $y = z = 0$. The circles are the measurement, the triangles are the 2-D simulation and the continuous curve is the 3-D simulation.

than the minimum required values because of standard material sizes. These parameters are also used for the simulations of the 3-D geometry. There is a good agreement between the measured field and the calculated one in 3-D. The field calculated in 2-D geometry is in agreement with the measurement in the flanks whereas in the middle the calculations give a larger field. The reason for this is that in 3-D the flux in the iron core is spread in the x and y direction in the pole face. However, in 2-D geometry the flux is only distributed in the x direction which gives rise to a higher field in the middle of the magnet.

In Fig. 2.10 the middle part of Fig. 2.9 is shown. The calculated fields are normalized to the measured field at $x = 0$. The inhomogeneity in the measurement and the 3-D calculation is 0.85 G and the inhomogeneity in the 2-D calculation is $0.55 \times 1900/1670 = 0.63$ G. These are all well within the requirement of 1.3 G.

It seems that upon zooming in, the 2D calculations agree better with the measurements than those for 3D. The meshes of the pole face for obtaining the results in Fig. 2.9 and Fig. 2.10 are about a few millimeters. In the case
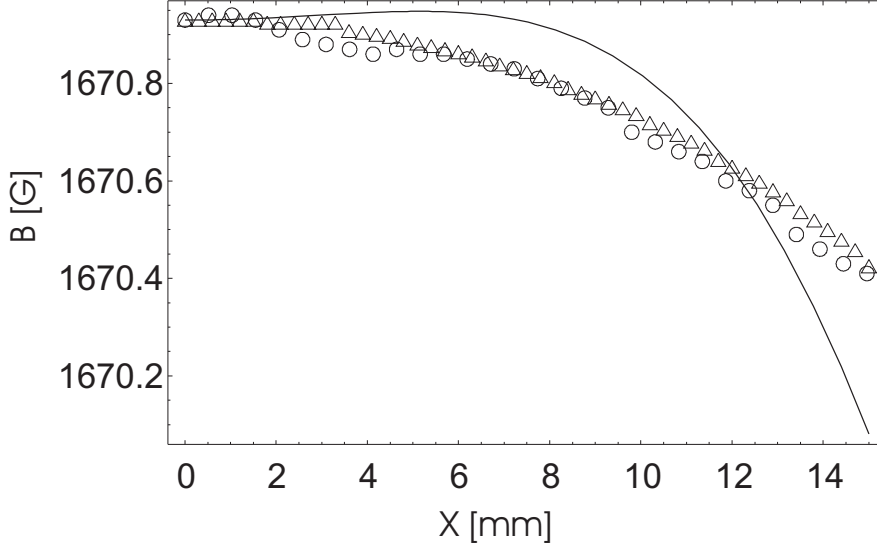
Figure 2.10: The normalized middle part of Fig. 2.9. The circles are the measurement, the triangles are the 2-D simulation and the continuous curve is the 3-D simulation.

of the results with 2D simulations the meshes were in the order a tenths of millimeters. So, this can be the reason for the deviation in Fig. 2.10. However, one should note that we are talking about differences of 0.1 *permille.*

2.7 Guide field coils

In the present SESANS instrument the magnets will be placed in guide fields, Fig. 2.11. The purpose of the guide field is to prevent the neutron beam from depolarization in a nearly zero field region. This field should be homogenous enough. The criteria is that two neutron paths in the beam should not give rise to a line integral difference of more than 2.2 G.cm.

A homogenous field can be produced by using a coil system consisting of four wires as shown in Fig. 2.12. These coils have a finite length in the x direction, but for simplicity we will consider them as infinite. For the magnetic field produced by the first wire we can write $\mathbf{B}(\mathbf{r}') = \frac{\mu_0 \mathbf{i} \times \mathbf{r}'}{2\pi |\mathbf{r}'|^2}$ with $\mathbf{i}$ the current through the wire and $\mu_0 = 4\pi \times 10^{-7}$ H.m^{-1} . Furthermore, $\mathbf{r} = \mathbf{r_0} + \mathbf{r}'$ with $\mathbf{r} = (y, z)$, $\mathbf{r}' = (y', z')$ and $\mathbf{r_0} = (\pm y_0, \pm z_0)$. Therefore, the field at a point (y, z) due to the four wires will be:

$$\mathbf{B}_c(y, z) = \sum_{j=1}^{j=4} \frac{\mu_0 \mathbf{i}_j \times (\mathbf{r} - \mathbf{r}_{0,j})}{2\pi |\mathbf{r} - \mathbf{r}_{0,j}|^2}. \tag{2.11}$$
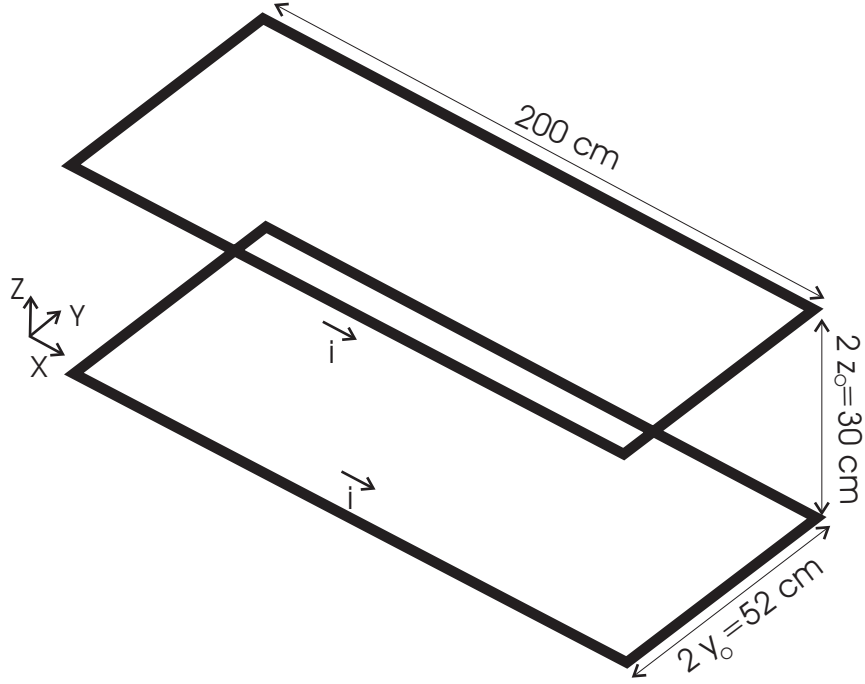
Figure 2.11: Guide field coils.

When the summation is carried out $B_c(y,z)$ can be calculated which is given by:

$$B_c(y,z) = \frac{2\mu_0 i y_0}{\pi} \times$$
$$\sqrt{\frac{y^4 - 2y^2(y_0^2 - z^2 + z_0^2) + (y_0^2 + z^2 + z_0^2)^2}{[(y-y_0)^2 + (z-z_0)^2][(y+y_0)^2 + (z-z_0)^2]}} \times$$
$$\sqrt{\frac{1}{[(y-y_0)^2 + (z+z_0)^2][(y+y_0)^2 + (z+z_0)^2]}}$$

(2.12)

If we expand this around $(y,z) = (0,0)$ we obtain:

$$B(y,z) = b_{0,0} + b_{2,0}y^2 + b_{0,2}z^2 + b_{2,2}y^2z^2 + b_{4,4}y^4z^4... \qquad (2.13)$$

where $b_{i,j} = \frac{\partial^i \partial^j B_c(y,z)}{\partial^i y \partial^j z}|_{y=0,z=0}$. This gives the following coefficients:

$$b_{0,0} = \frac{2\mu_0 i y_0}{\pi(y_0^2 + z_0^2)}$$

$$b_{0,2} = -\frac{2\mu_0 i y_0 (y_0^2 - 3z_0^2)}{\pi(y_0^2 + z_0^2)^3}$$
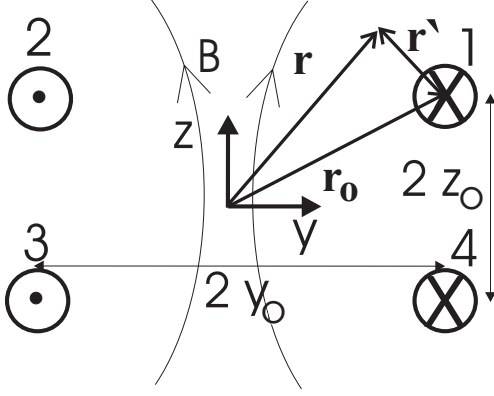
Figure 2.12: Four current wires in the $y - z$ plane.

$$
\begin{aligned}
b_{2,0} &= \frac{2\mu_0 i y_0 (y_0^2 - 3z_0^2)}{\pi (y_0^2 + z_0^2)^3} \\
b_{0,4} &= b_{4,0} = \frac{2\mu_0 i y_0 (y_0^4 - 10 y_0^2 z_0^2 + 5 z_0^4)}{\pi (y_0^2 + z_0^2)^5} \\
b_{2,2} &= -\frac{8\mu_0 i y_0 (y_0^4 - 12 y_0^2 z_0^2 + 3 z_0^2)}{\pi (y_0^2 + z_0^2)^5}
\end{aligned}
\tag{2.14}
$$

In order to have a homogeneous field up to fourth order in y and z, the coefficients $b_{0,2}$ and $b_{2,0}$ in Eq.2.13 should be zero, which is achieved by choosing $y_0 = \sqrt{3} z_0$ in Eq.2.14.

In Fig.2.13 the magnetic field distribution in the middle of the guide field in the $x-y$ plane is shown for which the current in each coil is 540 A, $z_0 = 15$ cm and $y_0 = 26$ cm. The inhomogeneity across a plane of 1.5×1.5 cm ^{2} is 0.003 G. This gives rise to a line integral difference of 0.3 G.cm over a length of 200 cm which is below the requirement of 2.2 G.cm.

2.8   Conclusions

In the center of a SESANS magnet in a volume of $30 \times 30 \times 30$ mm^3 the magnetic field homogeneity should be better than 1.3 G for a field of 2000 G. In order to achieve this, dipole magnets are used. The requirement on the homogeneity of the magnetic field is readily achieved. This is mainly dependent on the width of the pole face. For a half pole distance of $z_p = 3$ cm, see Fig.2.3 a width of 9 cm is enough, i.e. $x_p + x_s = 9$ cm. In order to save
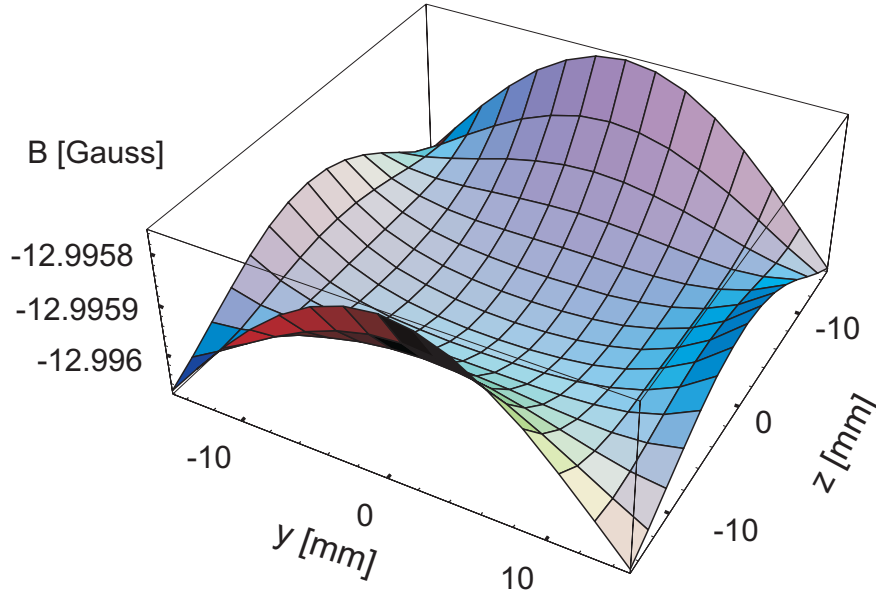
Figure 2.13: Field of the guide field coils at $x = 0$ in the $y - z$ plane.

weight one can choose the iron core smaller than 9 cm. However in this case the width of the core should not be smaller than 6 cm due to the saturation of iron. So $L = 6$ cm. For the homogeneous distribution of the flux lines the thickness of the pole face must be 3 cm, i.e. $z_s = 3$ cm. The saturation of the yoke must also be taken into consideration. This imposes restrictions on the minimal thickness of the yoke.

With these design parameters, in order to have 2000 G in the center one needs a total current of 5000 A through one current package.

Inhomogeneities of the z-component of the magnetic field will not contribute to the line integral inhomogeneities. The line integral is proportional to the square of the x-component of the magnetic field. This means that it is important in the design of the magnets to reduce these x-components.

A homogenous guide field can be obtained by using a coil consisting of four wires in which the distance of the wires to each other are chosen in a special way. If $y_0 = \sqrt{3}z_0$ then the coil produces a homogeneous field up to fourth order. This method of design can also be used when one needs quadratic increasing fields: the coefficients of the fourth order terms in Eq. 2.14 are then equated to zero. For correcting the line integrals inhomogeneities, coils having this property are used [25].

At the moment, the magnets and the guide field coils in the present SESANS setup are build according to these parameters.

Chapter 3

Line integral corrections

3.1 Introduction

In Chapter 1 we discussed four possible options for the realization of SESANS. The line integral of two of these options, three foil and wedge options, is not corrected automatically. In chapter 2 it was shown that the line integral cannot be corrected by increasing the pole gap distance of the dipole magnets used in SESANS. Here we will show that the line integral can be corrected by using external coils. This chapter consists of three section. In the first section line integral correction in one dimension will be treated. In the second section correction in two dimensions will be discussed. The last section is an analytical treatment of the applied correction scheme.

3.2 Line integral correction in one dimension

This section has been reprinted from Physica B, Vol. 297; Oktay Uca, Wicher H. Kraan, Wim G. Bouwman and M. Theo Rekveldt, Line integral corrections in Spin-Echo Small-Angle Neutron Scattering instrument, pp 28-31 Copyright (2001), with permission from Elsevier Science.

3.2.1 Introduction

Spin Echo Small Angle Neutron Scattering (SESANS) instrument is a novel SANS technique which enables one to characterize distances from a few nanometers up to the micron range [6], [10]. The most striking difference between normal SANS and SESANS is that in SESANS one gets information in real space, whereas in a SANS measurement one obtains data in reciprocal

space which has to be Fourier transformed. Another important difference is that a fully divergent beam can be used which means high intensity.

Larmor precession is the basic physical principle for SESANS: When a neutron enters a magnetic field the spin of the neutron precesses around the magnetic field. Larmor precession of neutrons is used to make a polarized beam precess through four precession regions in a symmetrical setup. The Larmor precession in a magnetic field B over a path l is given by:

$$\phi = c\lambda \int |B| dl, \tag{3.1}$$

with ϕ the precession angle, λ the wavelength and $c = 4.63 \times 10^{14} \, \text{T}^{-1}.\text{m}^{-2}$. The measured quantity in a SESANS experiment is the depolarization of the polarized beam. For an initial polarization, P_0, the final polarization, P, can be written as:

$$P = P_0 \cos(\Delta\phi) \tag{3.2}$$

Here $\Delta\phi$ is the difference in the precession angle between two paths which is proportional to the line integral difference $\Delta \int |B| dl$ between those paths (see Eq. 3.1). For a given dipole magnet there will be a significant line integral difference due to the fringing of the magnetic field lines near the magnet edges. We will show that this line integral differences give rise to unacceptable depolarization. We find, however, a method to correct and to maintain a good polarization.

3.2.2   Requirement on the homogeneity of the line integral

In Fig. 3.1 one can see a SESANS magnet and correction coils. For a horizontal path along the x-axis at $z = 0$ and one at $z \neq 0$ the difference in the line integral becomes (see Eq. 3.1)

$$\Delta(\int |B| dx) = \frac{\Delta\phi}{c\lambda}. \tag{3.3}$$

If we want the polarisation better than 0.98 then $\Delta\phi$ must be smaller than 0.2 rad., because $\cos 0.2 = 0.98$ (see Eq 3.2). Then

$$\Delta(\int |B| dx) \leq 2.2 \, \text{G.cm} \tag{3.4}$$

with $\lambda = 0.2 \, \text{nm}$.
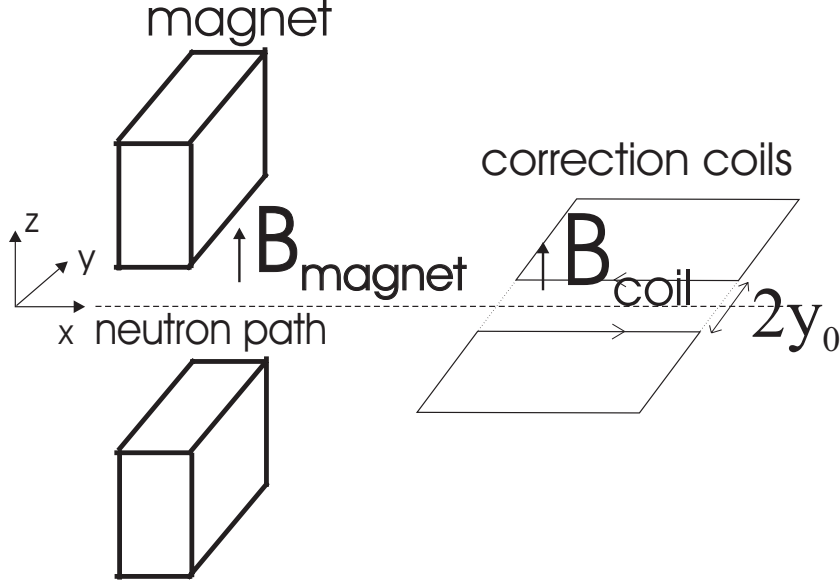
Figure 3.1: Dipole magnet as used in the SESANS instrument with correction coils. The coils are in the $x - y$ plane. $2 \times y_0$ is the distance between the two current wires.

3.2.3 Origin of the inhomogeneity of the line integral

The difference of the line integral between two paths can be written more specifically as:

$$\Delta(\int |B| dx) = \int \sqrt{(B_x'^2 + B_z'^2)} - \int B_z dx \qquad (3.5)$$

The primes denote the field values at some height $z = z_1$ for a horizontal path along x. The unprimed fields are those at $z = 0$. Because of symmetry, at $z = 0$ $B_x = 0$. The magnet is taken infinitely long in the y direction. This is a good approximation in reality. This means that the magnetic fields are independent of the y coordinate. The field in the z direction is much larger than the field in the x direction. Therefore we can expand the first term in Eq. 3.5. We can write then

$$\Delta(\int |B| dx) = \int (B_z' - B_z) dx + \int \frac{B_x'^2}{2B_z'} dx = \int \frac{B_x'^2}{2B_z'} dx \qquad (3.6)$$

Conservation of flux, $\nabla \cdot \vec{B} = 0$, can be used to show that the first term in Eq. 3.6 vanishes. So the line integral is proportional to the square of the x-component of the magnetic field.

3.2.4   Quadratic dependence of the line integral

The z component of the magnetic field in a point (x, z) is in second order:

$$B_z(x, z) = B_z(x, 0) + \frac{1}{2} \frac{\partial^2 B_z(x, 0)}{\partial z^2} z^2 \qquad (3.7)$$

since B_z is symmetric in z. The Taylor expansion of $B_x(x, z)$ around (x, z) is given by:

$$B_x(x, z) = B_x(x, 0) + \frac{\partial B_x(x, 0)}{\partial z} z = \frac{\partial B_x(x, 0)}{\partial z} z \qquad (3.8)$$

since the there are no x components at $z = 0$. $\nabla \times \overrightarrow{B} = 0$ allows us to write $\frac{\partial B_x}{\partial z} = \frac{\partial B_z}{\partial x}$. So Eq. 3.8 becomes:

$$B_x(x, z) = \frac{\partial B_z(x, 0)}{\partial x} z \qquad (3.9)$$

From Eq. 3.6, Eq. 3.7 and Eq. 3.9 we obtain up to first order:

$$\Delta(\int |B| dx) = cz^2 \qquad (3.10)$$

where

$$c = \frac{1}{2} \int \frac{\left(\frac{\partial B_z(x, 0)}{\partial x} \right)^2}{B_z(x, 0)} dx. \qquad (3.11)$$

So in first order the line integral increases quadratically with z. This means that if one wants to correct the line integral differences by means of correction coils the magnetic fields of the correction coils must also be quadratic in z. Furthermore, the value of the inhomogeneity of the line integral can be calculated from measured values of $B_z(x, 0)$, as will be done in the next section.

3.2.5   Correction of the line integral

In Fig. 3.1 the magnet and the correction coils are shown. The correction coils are placed in the $x - y$ plane. The magnetic field of the coils in the $y - z$ plane can be approximated by

$$B_c(y, z) = B_c(0, 0)(1 + (\frac{y}{y_0})^2 - (\frac{z}{y_0})^2 - 4\frac{y^2 z^2}{y_0^4}...) \qquad (3.12)$$

Here $2 \times y_0$ is the distance between the two current wires, see Fig 3.1. $B_c(0, 0) = \frac{\mu_0 I}{\pi y_0}$ is the magnetic field of the coil in $y = 0$, $z = 0$ with I the
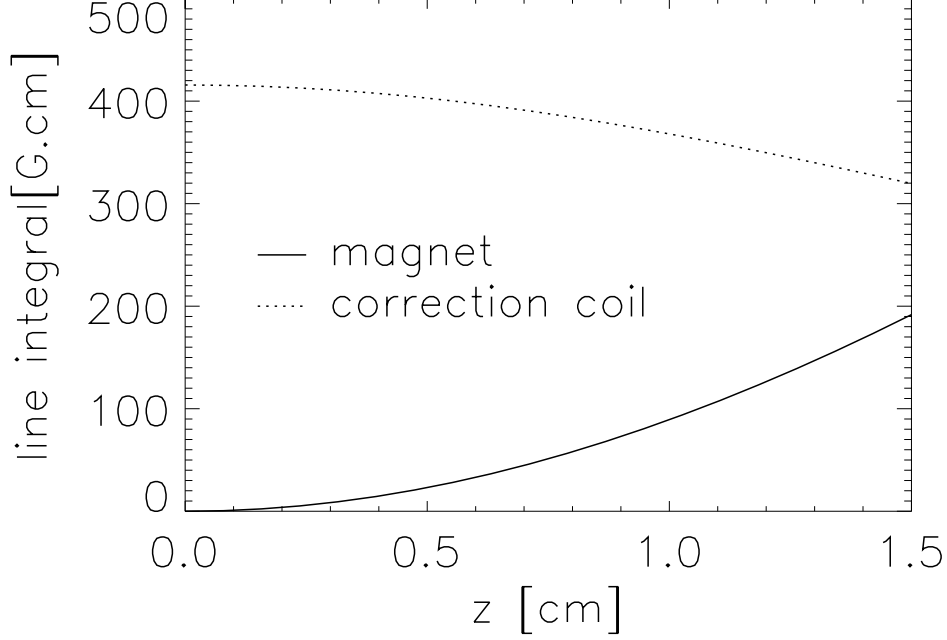
Figure 3.2: The varying part of the line integral difference of the magnet is obtained by measuring B_z along the x axis at $z = 0$. The value of the line integral at $z = 0$ has been subtracted from the curve. The line integral of the correction coils are calculated. The total current is 270 A. The length of the correction coils in the x direction is 18 cm.

current through the wires and $\mu_0 = 4\pi \times 10^{-7} \, \mathrm{H\, m^{-1}}$. For a sufficiently small beam in the y direction the fourth term in Eq. 3.12 can be neglected. This means that the B_c and thus the line integral of the correction coil decreases quadratically with z in the z direction. This is the opposite of the line integral of the magnet see Eq. 3.10. In Fig. 3.2 the total line integral of the correction coil and the varying part of the line integral difference of the magnet is shown. The line integral difference of the magnet is calculated according to Eq. 3.10 by measuring $B_z(x, 0)$ along the x axis at $z = 0$. The line integral of the correction coils is calculated numerically by making use of the Biot-Savart law. The line integral of the magnet and the correction coil are both nearly quadratic in z.

In Fig. 3.3 the sum of the curve of the correction coil with 270×1.48 A and the curve of the magnet is plotted which shows that some higher orders
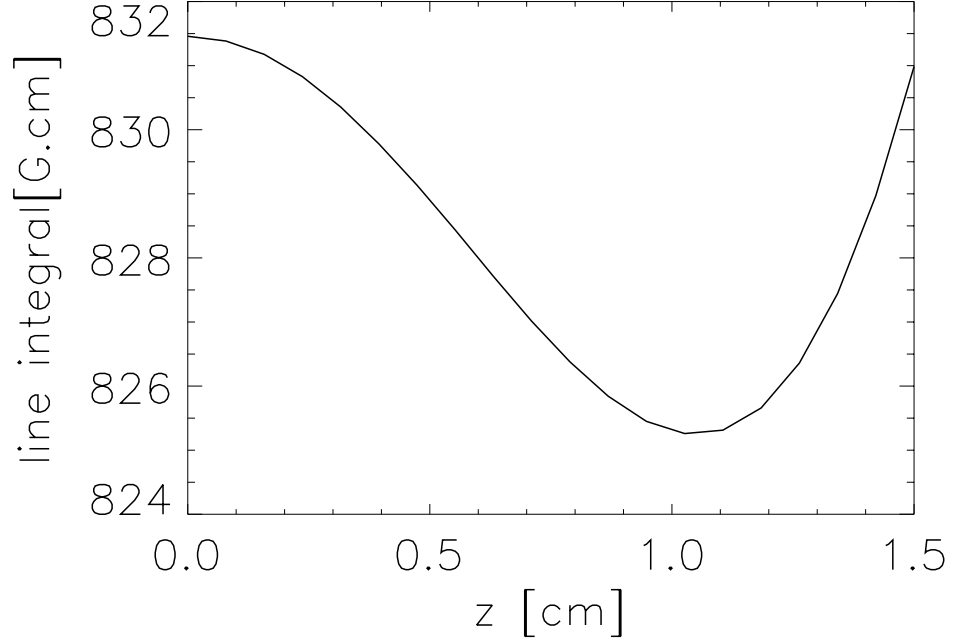
Figure 3.3: The sum of the curve of the correction coil with 270×1.48 A and the curve of the magnet in Fig. 3.2 which determines the final homogeneity of the line integral. The maximum deviation is 6.6 G.cm.

are present. The maximum deviation in the sum is 6.6 G.cm. This is a factor of 3 higher than the requirement (see Eq. 3.4). However, it should be noted that the difference of the line integral is reduced from 192 G.cm to 6.6 G.cm for $z = 1.5$ cm, i.e a factor of 29 (see Fig. 3.2). The remaining inhomogeneity is true for two extreme paths. However, the final polarization is determined by averaging the line integral of all the neutron paths over the beam cross-section.

Fig. 3.4 shows the measured polarization for a beam cross-section of 2x10 mm^2 as a function of the applied correction current for a SESANS setup using foils [10]. Without any correction the polarization is 0.46. As the current of the coils increases the polarization becomes 0.81. This is an improvement of the polarization with almost a factor of two. The maximal polarization in the present SESANS setup is 0.872 ± 0.004. This is shown by the straight line Fig. 3.4. Thus the polarization is nearly completely corrected. However, the correction that improved the homogeneity in the z-direction created an
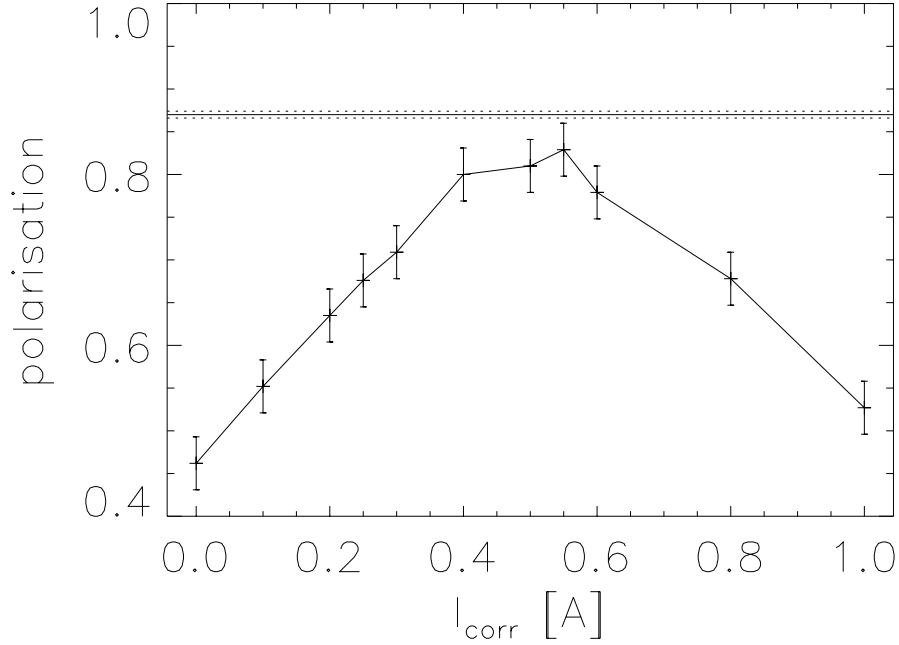
Figure 3.4: improvement of the polarization by applying a correction coil. $y_0 = 3$ cm. The beam cross-section is $2 \times 10\,\text{mm}^2$. The lines show the limit of the polarization in the present SESANS instrument.

inhomogeneity in the y-direction which will be treated in the next section.

3.2.6   Conclusion

In order to realize a SESANS instrument with a good polarization one needs homogeneous line integral differences. It has been shown that the line integral difference of a dipole magnet increases quadratically with z. By applying a correction coil of which the line integral decreases quadratically with z it is possible to homogenize the line integral differences of the magnet. This has been shown both theoretically and by measurement. At present this improvement of the polarization is only in the z direction. In the future we want to extend this improvement also in the y direction in order to have a good polarization over a beam cross-section of $30 \times 30\,\text{mm}^2$

3.3   Line integral correction in two dimensions

The content of this section has been accepted for publication in Applied
Physics A, 2002 as: "Line integral corrections in Larmor precession devices"
Oktay Uca, Wim G. Bouwman, Jeroen Plomp, Wicher Kraan, M.Theo Rekveldt.
Copyright by Springer-Verlag GmbH

3.3.1   Introduction

One of the powerful features of SESANS is the ability to use a full divergent
beam to measure directly correlation functions [6, 10]. This means that one
can use large beam cross-sections which lead to short measurement times
and high counting statistics. However, increase of beam size results in an
increase of line integral errors which depolarizes the beam. Fresnel-coils
are used to compensate the line integral errors for a magnetic field parallel
to the neutron beam [2]. Monkenbusch introduced a correction scheme for
zero field precession [27]. The first correction mechanism for magnetic fields
perpendicular to the neutron beam was introduced in [28].

However, the correction mechanism in [28] is only in one direction. As a
consequence, only a beam size of 2×15 mm^2 is used. The present article
reports line integral corrections in two directions by using a second correction
coil. One can now easily use beams of 10×15 mm^2.

3.3.2   Problem and method of correction

The SESANS setup with foil option is shown in Fig. 3.5. It consists of three
dipole electro-magnets and inclined magnetized foils. The first and last foil
start and stop the Larmor precession, respectively whereas the middle foil
acts as a π-flipper in order to obtain the spin-echo balance [10]. The magnetic
field in the magnets increases in the $\pm z$-direction with z^2. The line integral
along a neutron path is defined as $\int_{path} |\mathbf{B}| dl$. Therefore, the line integral
$L_m(z)$ of one magnet which is infinitely long in the y-direction can be written
as [28]:

$$L_m(z) = \int |\mathbf{B}| dx = c_0 + c_m z^2 \qquad (3.13)$$

in which c_m can be calculated from $B_z(x, 0)$ a measured z-component of the
field along x at $z = 0$:

$$c_m = \frac{1}{2} \int \frac{\left(\frac{\partial B_z(x,0)}{\partial x}\right)^2}{B_z(x,0)} dx. \qquad (3.14)$$
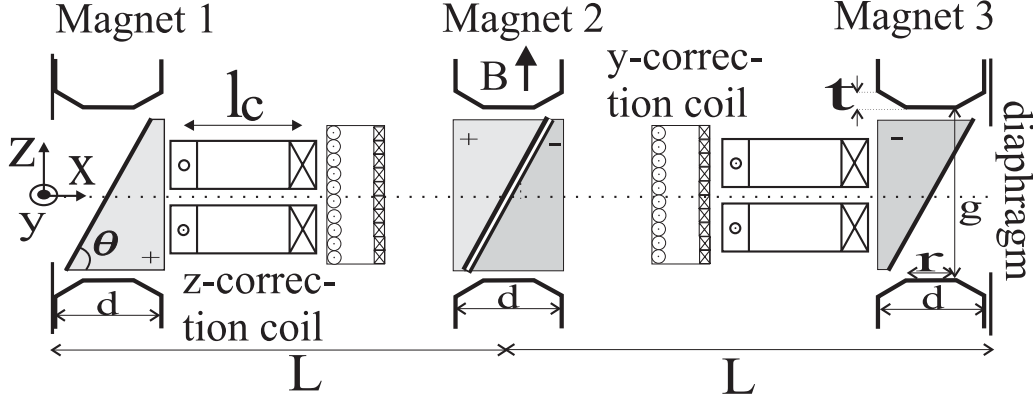
Figure 3.5: SESANS setup with foil option and correction coils. l_c is the effective length of the z-correction coil, r and d are two length dimensions of the pole face, t is the thickness of the pole face, L is the half length of the setup, g is the gap distance and θ is the inclination angle of the foils. In the experiments, the magnet parameters were t=1 cm, g=3 cm, r=10 cm, d=16 cm, θ=45 deg, l_c=16 cm and L=128 cm.

In order to correct the line integral error in the z-direction we will use two correction coils; one coil transforms the z-gradient into a y-gradient, which can be corrected directly by a second coil as shown in Fig. 3.5. The z-correction coil consists of four bunches of current carrying wires as shown in Fig. 3.6A. The outer wires are not shown in this figure. A Taylor expansion up to fourth order of the magnetic field generated by the coils using Biot-Savart law gives:

$$B_c(y,z) = \frac{2Iy_0\mu_0}{\pi(y_0^2 + z_0^2)}(1 + \frac{y_0^2 - 3z_0^2}{(y_0^2 + z_0^2)^2}y^2 - \frac{y_0^2 - 3z_0^2}{(y_0^2 + z_0^2)^2}z^2 -$$
$$4\frac{y_0^4 - 12y_0^2z_0^2 + 3z_0^4}{(y_0^2 + z_0^2)^4}y^2z^2),$$

$$(3.15)$$

where $\mu_0 = 0.4\pi$ G.cm/A and I is the current through the wires. The coefficient of the higher order term y^2z^2 will vanish if we choose $z_0 = 0.29y_0$. If we substitute this ratio of 0.29 in (3.15) the line integral $L_{cz}(y,z)$ for the z-correction coil of length l_c can be given by :

$$L_{cz}(y,z) = \frac{0.59\mu_0 l_c I}{y_0} + \frac{0.37\mu_0 l_c I}{y_0^3}(y^2 - z^2) + O(y^4, z^4)$$
$$\equiv c_{z,0} + c_z(y^2 - z^2) + O(y^4, z^4),$$

$$(3.16)$$
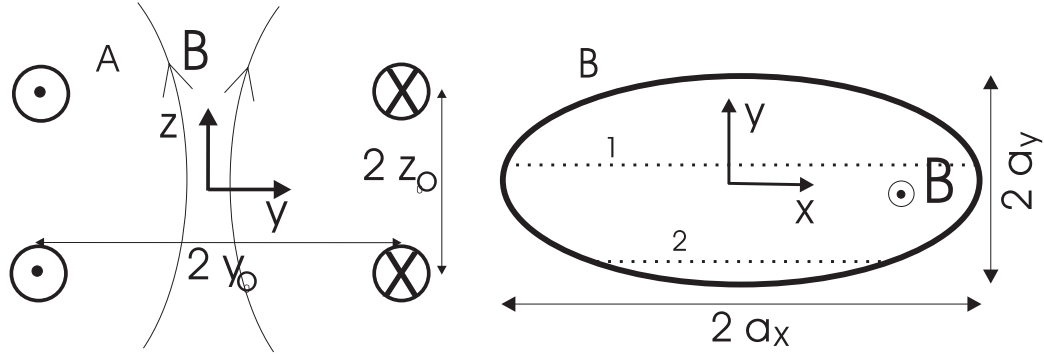
Figure 3.6: A)Front view of the z-correction coil. It consists of four bunches of current carrying wires. $2y_0$ and $2z_0$ are the distances between the bunches of wires int the z and y-direction respectively. B) top view of the y-correction coil. It is a parabolic coil in the y-direction and infinitely long in the z direction. Two neutron beams, 1 and 2, are also indicated in the figure. $2a_x$ and $2a_y$ are the longest distances between the wires of the coil in the x and y direction respectively.

in which the y and z dependencies are separated from each other up to fourth order. To correct the line integral error in the z-direction we must choose $c_z = c_m$ see (3.13) and (3.16). Then the total line integral of the magnet and the z-correction coil will be

$$L_m(z) + L_{cz}(y, z) = c_0 + c_{z,0} + c_m y^2. \qquad (3.17)$$

This equation shows that the line integral is independent of z, but now a y-dependency has been introduced. This is because the z-correction coil actually transforms the line integral errors in the z-direction into the y-direction. To overcome this problem a second correction coil of aluminum wire is used which transmits the neutrons very well. This is a parabolically wound coil which produces a homogenous field B in the z-direction. Two neutron paths are shown in Fig. 3.6B. Path "2" is shorter than path "1". Therefore neutrons which follow path "2" will acquire less line integral than those of path "1". As a result, a quadratic decrease of the line integral is obtained: the path length can be described by $2a_x(1 - (\frac{y}{a_y})^2)$. So the line integral of the y-correction coil can be given by

$$L_{cy}(y) = 2a_x B(1 - \frac{y^2}{a_y^2}) \equiv c_{y,0} - c_y y^2. \qquad (3.18)$$

To compensate the y dependency in (3.17) we must choose $c_y = c_m$. The total line integral of the magnet, the z-correction coil and the y-correction
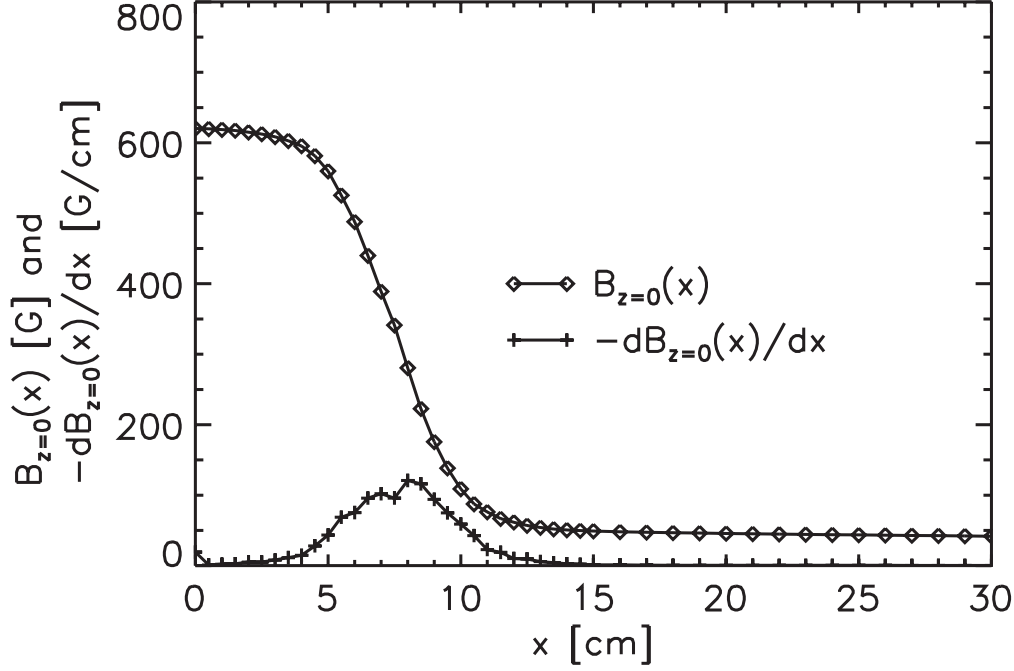
Figure 3.7: Measured value of $B_{z=0}(x)$ and its derivative $dB_{z=0}(x)/dx$.

coil is then

$$L_m(z) + L_{cz}(y, z) + L_{cy}(y) = c_0 + c_{y,0} + c_{z,0}. \tag{3.19}$$

This is independent of y and z and thus, homogenous as is required for successful SESANS measurements.

3.3.3   Results

In Fig. 3.7 a measurement of $B_z(x)$ at z=0 is shown. The calculated value of $dB_z(x)/dx$ is also plotted. Applying (3.14) yields $c_m = 93.4$ G/cm. However, in the polarization measurements the field at $x = 0$ was 533.6 G instead of 620 G see Fig. 3.7. This is due to the different experimental conditions. Therefore, $c_m = 93.4 \times 533.6/620 = 80.4$ G/cm. From the condition $c_z = c_m$ we can calculate the required current in the z-correction coil with (3.16):

$$I = \frac{c_m y_0^3}{0.374 \mu_0 l_c}. \tag{3.20}$$

This gives a current of $I = 586.6$ A for $y_0 = 3.8$ cm, $l_c = 16$ cm and $c_m = 80.4$ G/cm. The coils which we used had 200 windings. Therefore, the current which we need from the power supply is 2.93 A.
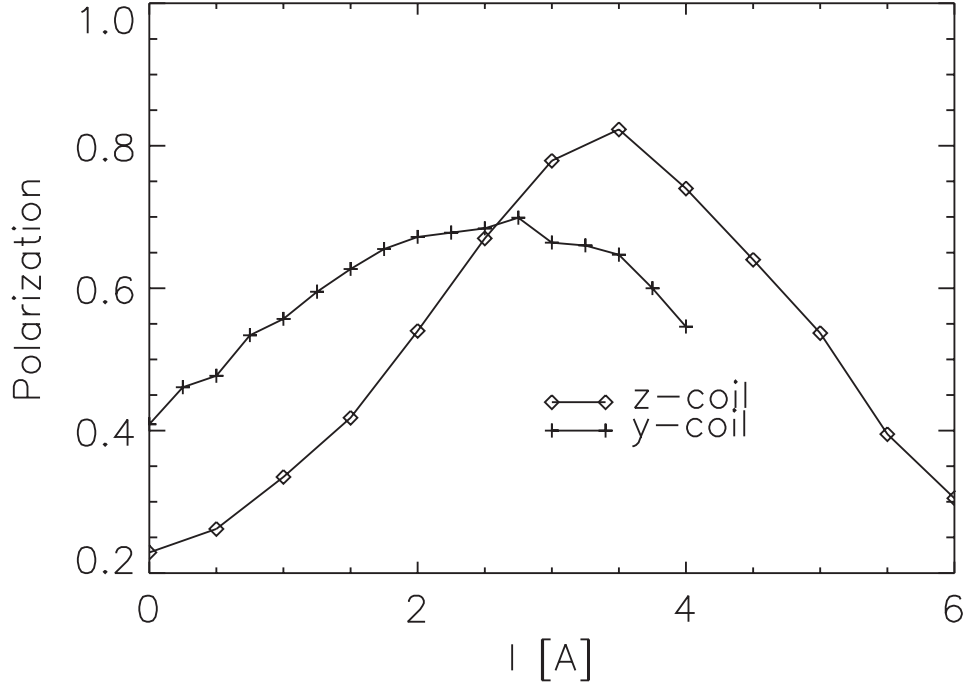
Figure 3.8: Improvement of the polarization as a function of current through the correction coils. The z correction coil consists of 200 windings. The beam cross-section is 2×15 mm ^{2} The y-correction coil consists of 157 windings. The beam cross-section is 10×15 mm ^{2}.

The required field in the y-correction coil can be obtained form the condition $c_y = c_z = c_m$:

$$B = \frac{c_m a_y^2}{2 a_x},$$ (3.21)

which for $a_x = 2.5$ cm and $a_y = 1.7$ cm, yields $B = 46.46$ G.

In Fig. 3.8 the polarization is shown as a function of the current through the z and y-correction coils for a beam size of 2×15 mm^2 and 10×15 mm^2, respectively. The best correction in z-direction occurs for a current of 200×3.5 A. The small deviation from the expected value of 200×2.93 A is partially due to the finiteness of the z-correction coil. In deriving (3.15) we neglected the end effects. Furthermore, the coils were placed between two iron plates acting as a guide field. This will also lower the gradient of the correction coil.

The optimum current for the y-correction coil is at 157×2.5 A. From a simulation performed with the software package Radia [23], the required current for producing a field of 46.46 G is 157×2.40 A. This is in very good
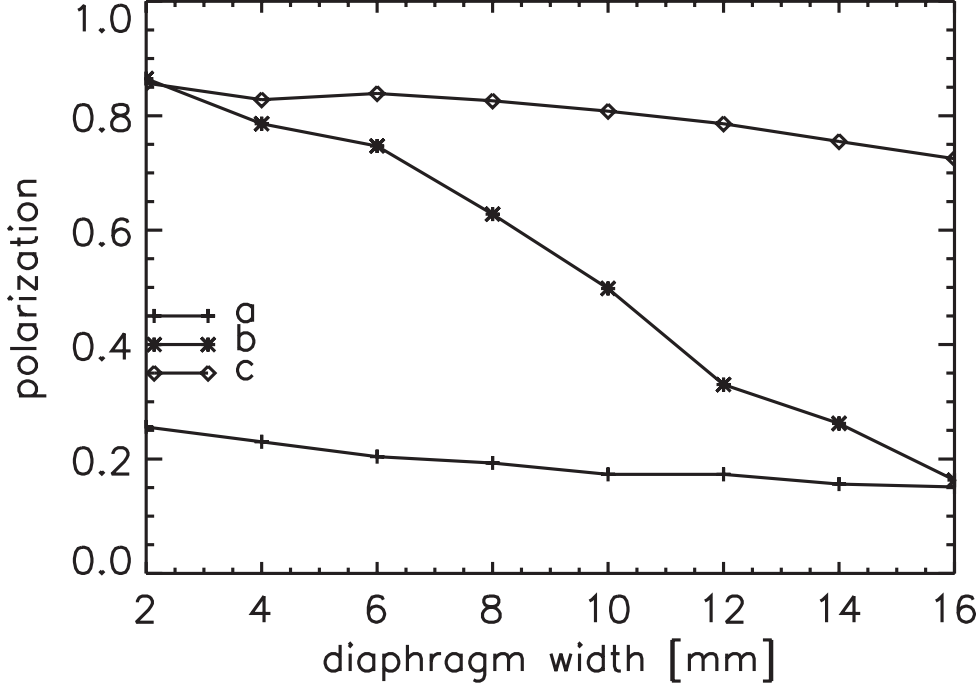
Figure 3.9: Improvement of the polarization with z- and y-correction coils switched on. Diaphragm height is 15 mm. The magnetic field in the magnets is 533.6 G. a) y correction coil and z correction coil are switched off. b) Only the z-correction coil is switched on. $I_z = 200 \times 3.5$ A, $I_y = 0$ where I_z and I_y are the currents through the z and y coils, respectively. c)Both z correction and y-correction coils are switched on. $I_z = 200 \times 3.5$ A, $I_y = 157 \times 2.25$ A.

agreement with the expected value. The working of the y-correction coils is shown in Fig. 3.9. The diaphragm width is increased for a constant height of 15 mm. If no correction is applied the polarization $P = 0.25$ for a 2 mm width beam. With the z-correction coils switched on $P = 0.86$. This is also the maximum achievable polarization level in the present SESANS setup due to the foils, flippers, polarizer and analyzer as found with a pencil beam. For large diaphragm widths the polarization decreases, as it is expected. The y-correction coils improve the polarization. For a beam of 10×15 mm^2 $P = 0.82$. The slight decrease of P for large diaphragm widths is due to the deviation of the magnetic field of the magnet from being quadratic.

3.3.4   Conclusions

Line integral errors can be corrected by using two correction coils. The z-correction coil transforms the line integral errors from the z-direction to the

y-direction. In addition, this coil has the advantage that the neutrons are not passing through the wires of the coil. A second correction coil is used to correct the errors in the y-direction. This coil has a parabolic shape. For a beam of 10×15 mm^2 the polarization improves from $P = 0.2$ to $P = 0.82$. This method of correction is not limited to a beam of 10×15 mm^2. It can even be used for larger beam sizes as long as the magnetic field changes quadratically from the symmetry center. This is always possible by choosing the magnet dimensions sufficiently large.

3.4 Analytical treatment of correction

In this section we will analyze in more detail the principles of the correction coils in the SESANS setup. In Fig.3.10 a sketch of the SESANS instrument is given. An arbitrary neutron path through the diaphragm opening is also drawn. This path can be given by $z = mx + n$. Because of the diaphragms not all values of (m, n) are allowed. If the diagram height is $2z_d$ then $\forall z \in [-z_d, z_d]$ at $x = 0 \leftrightarrow z \in [-z_d, z_d]$ at $x = 2L$. For $x = 0$ $n \in [-z_d, z_d]$. So we get the condition that for $n \in [-z_d, z_d]$, $m \in [\frac{-z_d - n}{2L}, \frac{z_d - n}{2L}]$.

The first and the last magnet are placed symmetrically around the second magnet at a distance L and the first and second correction coils which have a length l are placed at a distance a from magnet 1 and 3. The center of the magnets and the intersection of the foils with the x-axis is at x_1, x_2, x_3, whereas the path intersects the foils at x_{f1}, x_{f2}, x_{f3}. Thus the precession in the first magnet starts at $x = x_{f1}$ and stops at $x = x_1 + d/2$. The foils can be described by $z = \tan(\theta_0)(x - x_i)$ where $i = 1, 2, 3$. This means that the path intersects the foils at:

$$x_{fi} = \frac{\tan(\theta_0)x_i + n}{\tan(\theta_0) - m} \tag{3.22}$$

with $i = 1, 2, 3$.

For the magnetic field in the magnet we can take:

$$B(z) = B(0)(1 + \alpha_i z^2) \tag{3.23}$$

with $i = 1, 2, 3$. In principal, the x-component must be modelled, because it is the origin of the line integral difference. However, for analyzing the working of the correction coils we can also take a field changing quadratically in the z direction. Since the correction coils do not make B_x zero, but they compensate the line integral caused by a quadratically changing field in the z direction. From the point of view of correction it does not matter whether
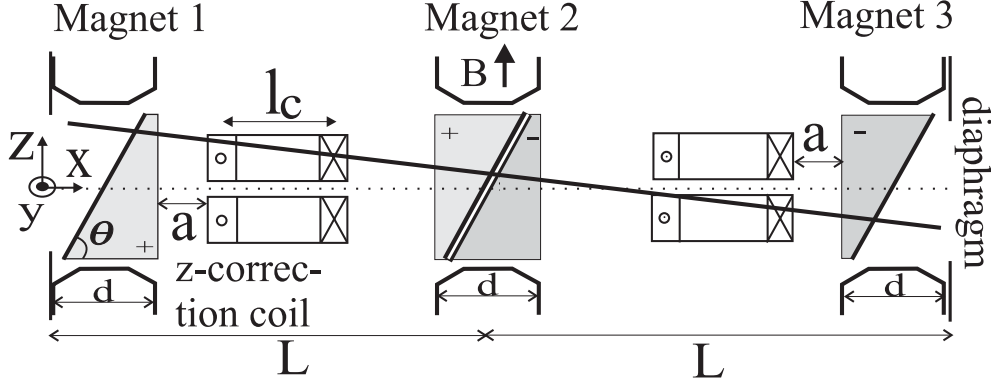
Figure 3.10: Side view of the SESANS instrument with foils. Two correction coils are used for correcting the line integral.

this change is caused by the x-component of the field or the z-component. The side effect of this will be that the value of the correction current will not be the absolute one. For the correction coils we take, Eq.3.12:

$$B_c(z) = \frac{\mu_0 I}{\pi y_0}(1 - (\frac{z}{y_0})^2). \tag{3.24}$$

The total precession in presence of the correction coils is the line integral of the magnetic field along the neutron path l, i.e $\phi = c\lambda(\int B(z)dl + \int B_c(z)dl)$. The path can be parameterized by $z = mx + n$ with $x \in [0, 2L]$. Therefore the total precession becomes:

$$\phi = c\lambda\left\{ B(0)\sqrt{1 + m^2}\left(\int_{x_{f1}}^{x_1+d/2}(1 + \alpha_1 z^2)dx + \int_{x_2-d/2}^{x_{f2}}(1 + \alpha_2 z^2)dx \right.\right.$$

$$\left. - \int_{x_{f2}}^{x_2+d/2}(1 + \alpha_2 z^2)dx - \int_{x_3-d/2}^{x_{f3}}(1 + \alpha_3 z^2)dx \right) +$$

$$\left. \frac{\mu_0 I}{\pi y_0}\left(\int_{x_1+d/2+a}^{x_1+d/2+a+l}(1 - \left(\frac{z}{y_0}\right)^2)dx + \int_{x_3-d/2-b-l}^{x_3-d/2-b}(1 - \left(\frac{z}{y_0}\right)^2)dx \right)\right\} \tag{3.25}$$

Consider the case when $\alpha_1 = \alpha_2 = \alpha_3 = 0$, and $I = 0$, corresponding to the situation when the magnets are homogeneous and there is no correction coil. Note that θ, the angle between the foils and x axis, is arbitrary. Calculation of Eq. 3.25 gives $\phi = 0$. Thus each path is in echo.

In the following Eq. 3.25 will not be calculated, because it is to lengthy. Instead we will look if there is any current, I, for which the precession $\phi = 0$

is independent of (m, n). If this is true then with one current value each neutron path is in echo and the line integral inhomogeneities are corrected. In the following we will consider several cases with regard to the homogeneity in the magnets and the shape of the precession regions.

3.4.1   Same inhomogeneity in all three magnets and rectangular precession regions

This corresponds to $\alpha_1 = \alpha_2 = \alpha_3 = \alpha$ and $\theta_0 = \pi/2$. A solution for I with $\phi = 0$ gives:

$$I = \frac{\alpha B(0)d(d - 2L)\pi y_0^3}{2l(2a + 2d - 2L + l)\mu_0},\tag{3.26}$$

which is independent of (m, n). Therefore it is possible to make the line integral inhomogeneities vanish if one chooses the current equal to the value given in Eq.3.26.

3.4.2   Same inhomogeneity in two magnets and rectangular precession regions.

Let us now take $\alpha_1 = \alpha_2 = \alpha$ and $\theta_0 \Rightarrow \pi/2$. The first and second magnet have the same inhomogeneity whereas the third is different. We obtain for I the following:

$$
\begin{aligned}
&I = B(0)d\pi y_0^3 \times \\
&\frac{\{\alpha[k - 12dm(Lm + n)] - [7d^2m^2 - 18d(2Lm + n)m + 12(2Lm + n)^2]\alpha_3\}}{48l(2a + 2d - 2L + l)m(Lm + n)\mu_0}
\end{aligned}
$$

$$\tag{3.27}$$

with $k = 7d^2m^2 + 18dnm + 12n^2$ and. Because I depends on (m, n) it is not possible to correct the line integral inhomogeneities for all neutron paths with one current value.

3.4.3   Same inhomogeneity in all three magnets and triangular precession regions.

For $\theta_0 \to \pi/4$ we have a triangular shaped precession region. If we take the inhomogeneities in the magnets the same, i.e $\alpha_1 = \alpha_2 = \alpha_3 = \alpha$ we obtain for I:

$$I = \frac{\alpha B(0)\pi y_0^3\{(3mr - 2)d^2 - 4Ld(2mr - 1) + 4L^2 mr\}}{4l\mu_0(2a + 2d - 2L + l)(m - 1)^3} \tag{3.28}$$

with $r = m^2 - 3m + 3$. This equation depends only weakly on m and not on n. Therefore only paths with the same slope are completely corrected. However, if we neglect the weak dependency on m, Eq. 3.28 becomes:

$$I = \frac{\alpha B(0)\pi y_0^3 d\{d - 2Ld\}}{2l\mu_0(2a + 2d - 2L + l)} \tag{3.29}$$

This equation is the same as Eq.3.26 and independent of (m, n). So, one can correct with one current value in approximation all paths.

3.4.4 Conclusions

We have studied the correction scheme analytically for correcting the line integral inhomogeneities in the z direction for the SESANS setup. The amount of current needed for the correction coils for each neutron path is expressed among other things in terms of inhomogeneity of the magnetic field and inclination angle θ_0 of the foils. If the inhomogeneity in all magnets are the same and there are rectangular precession regions all paths are corrected with one current value. If the precession regions are triangularly shaped then the current for each path is independent of the height of the beam but depends weakly on the slope of the path which can be neglected. Therefore, it is possible to correct all paths with one current value.

Chapter 4

Model calculations for the Spin-Echo Small-Angle Neutron Scattering instrument

Abstract

Spin-Echo Small-Angle neutron scattering (SESANS) is a new kind of SANS technique enabling measurements to be made directly in real space from a range of a few nanometers up to microns. In this paper it is shown that SESANS measures directly correlations by calculations on models. Furthermore, the effect of polydispersity and structure factor has been studied. An exact expression for the correlation function has been derived in the case of random systems such as fractal systems.

4.1 Introduction

SESANS extends the range of characteristic length scales which can be probed by SANS into the micron range. With SESANS, correlation functions like quantities can be measured in real space instead of momentum space as in normal SANS [6, 10]. We shall call this quantity the SESANS correlation function or correlation function for shorthand when there is no ambiguity. The reason for this is that the SESANS correlation function re-

sembles the real space correlation function. The underlying technique is the Larmor precession of neutrons in a magnetic field. SESANS can be realized by a setup which consists of two parts with precession areas. In its simplest form, each part consists of a parallelogram shaped magnetic field region. The neutron spin precesses in the two parts in the opposite sense. Because the path length in the two regions is the same for an unscattered beam, the polarization will not change. After passing through the two field regions, the initial state and the final state of the polarization will be the same. This is called the echo condition. However, for a scattered beam the path length in the two parts of the parallelogram may be different. This will lead to depolarization of the neutron beam.

Thus the measured quantity in SESANS is the change in polarization which is a function of the correlation function. The correlation function can be given by [10]:

$$G(z) = \frac{1}{\sigma k_0^2} \int_{-Q_{zm}}^{Q_{zm}} \int_{-Q_{ym}}^{Q_{ym}} \frac{d\sigma(\mathbf{Q})}{d\Omega} \cos(Q_z z) dQ_z dQ_y. \qquad (4.1)$$

$G(z)$ resembles a Fourier transform between Q_z and z, which can be identified as a probability function for the occurrence of the spin-echo length z. The latter is a measure for the distances between two scattering volumes in the sample that is probed. Furthermore, k_0 is the wave vector of the initial beam, $\mathbf{Q}$ the momentum transfer and σ the scattering probability per unit length of thickness:

$$\sigma = \frac{1}{k_0^2} \int_{-Q_{zm}}^{Q_{zm}} \int_{-Q_{ym}}^{Q_{ym}} \frac{d\sigma(\mathbf{Q})}{d\Omega} dQ_z dQ_y. \qquad (4.2)$$

The integration boundaries are determined by the critical reflection angle of the polarizer and analyzer mirrors in the y-direction and the acceptance angle of the detector in the z-direction. This leads to $Q_{ym} = 0.13$ nm $^{-1}$ and $Q_{zm} = 0.94$ nm $^{-1}$ in the setup used in the Delft reactor [6]. These values will also be used in the subsequent sections unless stated otherwise. For particles with a radius larger than 10 nm the scattering is mainly in the low angle regime. Therefore, for particles of 200 nm radius the integration boundaries are effectively infinite. The scattering cross-section is given with the local monodisperse approximation by: [29]

$$\frac{d\sigma(\mathbf{Q})}{d\Omega} = \eta(\Delta\rho)^2 \int_0^\infty D(R')v(R')^2 F^2(\mathbf{Q}, R')S(\mathbf{Q}, R')dR'. \qquad (4.3)$$

In these equations η is the volume fraction, $\Delta\rho$ the scattering length density difference between the particle and solvent , $v(R')$ the volume of a particle, $F(\mathbf{Q}, R')$ the form factor, $S(\mathbf{Q}, R')$ the structure factor and $D(R')$ the number

size distribution. The relation between the polarization P and correlation function $G(z)$ in the presence of multiple scattering is [11]:

$$P(z) = e^{-\sigma t(1-G(z))} \tag{4.4}$$

where t is the thickness of the sample. Single scattering is just the first order expansion of Eq. 4.4. Therefore, the polarization for single scattering is:

$$P_1(z) = 1 - \sigma t + \sigma t G(z). \tag{4.5}$$

Recently, Zhao [30] proposed a SESANS setup with cylindrical precession areas. Although this gives rise to symmetrical formulas for calculating the SESANS signal, it is not applicable for the Delft setup. The reason for this is that Zhao's formulas are applicable in a cylindrically symmetrical SESANS setup whereas SESANS formulas for the Delft setup are valid in general. Furthermore, one must use a small pinhole in Zhao's setup in front of the sample. Otherwise, the non-scattered beam that crosses the symmetry axis in one of the precession areas is not in echo. However, one of the powerful features of SESANS is the ability to use a full divergent, large cross-section beam for measurements which leads to short measurement times and high counting statistics. For these reasons the Zhao setup is not equivalent to the SESANS setup in Delft. Therefore, the formulas given by Zhao cannot be used to calculate the SESANS correlation function in our case.

Our main objective in this paper is to show that the SESANS correlation function is directly related to the real space structure. Furthermore, since SESANS is a technique under development we do not know its strong and weak features. Therefore, we want to explore the possibilities of SESANS before we decide which real experiments to do first.

In some cases the effect of the structure factor will also be incorporated in the calculations. Once the correlation function is known, the polarization can easily be calculated by Eq. 4.4.

The effect of background (incoherent scattering)is in SESANS quite different compared with SANS. The background in SESANS is always orders of magnitude smaller than the SESANS signal. The reason for this is that in SANS one has to obtain data as a function of Q whereas; in SESANS we integrate over the whole Q-range. In SANS the signal to background ratio becomes particularly important at large Q. In SESANS the contribution of this region to the signal is small compared to the small Q-range.

4.2   Spherical systems
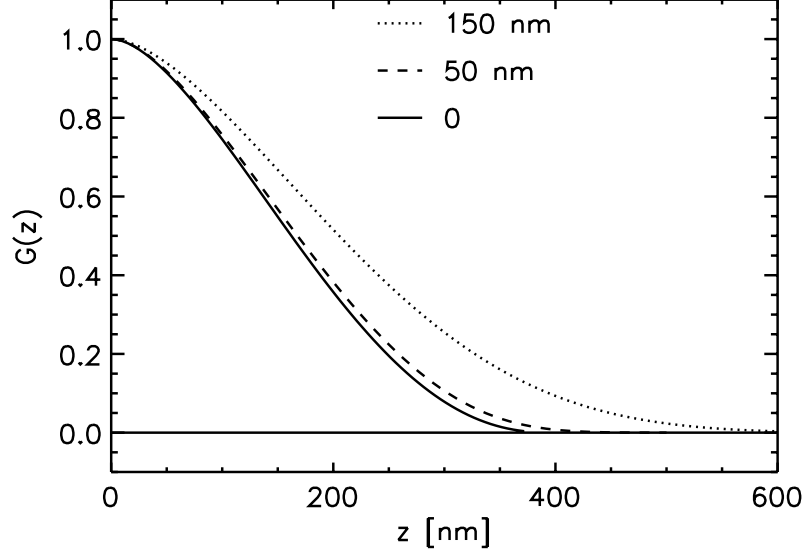
Figure 4.1: Correlation functions of three polydisperse spheres. The spheres have a Gaussian distribution with R=200 nm and a full-width half-maximum of 0, 50 and 150 nm.

4.2.1   Polydisperse systems

For a sphere with radius R the form factor is [29]:

$$F_s(Q) = \frac{3(\sin(QR) - QR\cos(QR))}{(QR)^3}. \qquad (4.6)$$

The corresponding correlation function has already been calculated by Rekveldt [6].

Fig. 4.1 shows the effect of polydispersity on a spherical system with a radius of $R = 200$ nm. The curves are calculated according to Eq. 4.1. A Gaussian distribution is taken for $D(R')$:

$$D(R') = 2^{-4(\frac{R'-R}{\Gamma})^2}. \qquad (4.7)$$

where Γ is the full width half maximum. The structure factor is set to 1. For reasons of comparison, $G(z)$ of a mono disperse sphere is also calculated. The largest length over which correlations are possible in a sphere of $R = 200$ nm is 400 nm. Therefore, in Fig. 4.1 the correlation function for the mono disperse sphere vanishes after 400 nm. As the width of the distribution gets larger, longer lengths over which correlations are present become available,
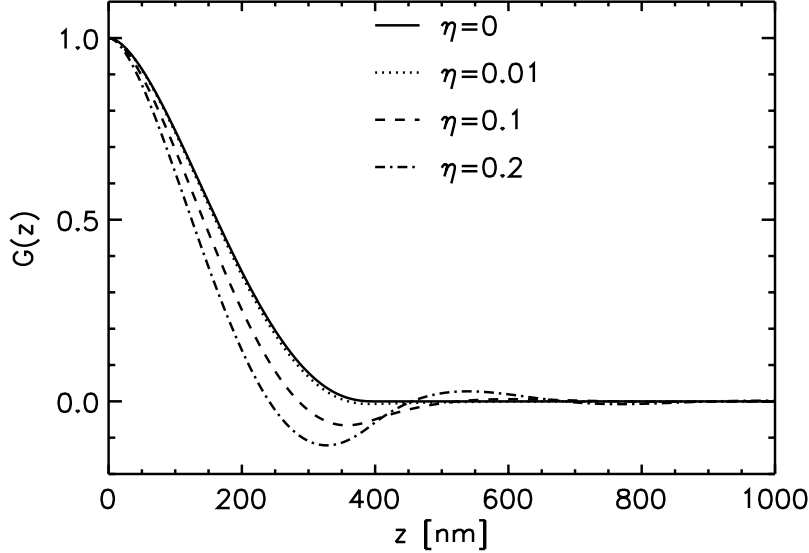
Figure 4.2: Correlation function of spheres interacting with a hard-sphere potential. The hard-sphere radius is R=200 nm with varying volume fractions of 0, 0.01, 0.1 and 0.2.

thus, the correlation function vanishes at larger length scales. For the curve for $G(z)$ in which $D(R')$ is used with a $\Gamma = 150$ nm the upper radius at the value $D(R') = 0.5$ is 275 nm. The largest length over which correlations are possible for spheres of this radii is 550 nm. So, it is to be expected that the correlation function vanishes at larger length scales. In the figure the corresponding correlation function indeed becomes zero after 550 nm. The smaller radius at this value of Γ will contribute to the beginning part of the correlation function and thus will not matter.

As can be seen from Fig. 4.1 the curve with 150 nm FWHM has the same shape as the monodisperse curve. So, these curves cannot be distinguished from each other. Therefore, determination of Gaussian polydispersity cannot be done by SESANS.

4.2.2 Effect of structure factor; hard-sphere model

In this section we will look at the effects of the structure factor on the correlation function for a system of spherical particles. As form factor we take Eq.4.6 again. There are only a few cases for which analytical expressions exist for the structure factor. If the interaction potential is the hard-sphere

potential the structure factor can be calculated. In this model the particles interact with a hard-sphere radius of R and have a volume fraction η. The structure factor is given by [29, 31]:

$$S(Q) = \frac{1}{1 + 24\eta H(2RQ)/(2RQ)} \qquad (4.8)$$

where the function H is defined as:

$$H(A) = \alpha \frac{\sin(A) - A\cos(A)}{A^2} + \beta \frac{2A\sin(A) + (2 - A^2)\cos(A) - 2}{A^3} \qquad (4.9)$$
$$+ \gamma \frac{-A^4\cos(A) + 4\left[(3A^2 - 6)\cos(A) + (A^3 - 6A)\sin(A) + 6\right]}{A^5}$$

and:

$$
\begin{aligned}
\alpha &= \frac{(1 + 2\eta)^2}{(1 - \eta)^4} \\
\beta &= \frac{-6\eta(1 + \eta/2)^2}{(1 - \eta)^2} \\
\gamma &= \eta\alpha/2.
\end{aligned}
\qquad (4.10)
$$

The correlation function has been calculated for four volume fractions, i.e. $\eta = 0$, $\eta = 0.01$, $\eta = 0.1$ and $\eta = 0.2$ see Fig. 4.2. For $\eta = 0$ the structure factor evaluates to 1. In this case we have the correlation function corresponding to mono disperse homogenous spheres with a radius of 200 nm.

For $\eta = 0.2$ we see clear oscillations. These are due to interference with the surrounding particles. Although we have not used regions with negative scattering lengths, there are negative values of the SESANS correlation function. To understand this we will write the structure factor in terms of pair correlation function $g(\mathbf{r})$:

$$S(\mathbf{Q}) = 1 + \eta \int d\mathbf{r}\, e^{i\mathbf{Q}\cdot\mathbf{r}}(g(\mathbf{r}) - 1). \qquad (4.11)$$

If we substitute this in Eq.4.1 with $D(R') = \delta(R' - R)$ we obtain for $G(z)$:

$$G(z) = \frac{1}{\sigma k_0^2}\left[\int F^2(\mathbf{Q})\cos(Q_z z)d\mathbf{Q} + \eta \int F^2(\mathbf{Q})\cos(Q_z z)\left(\int d\mathbf{r}' e^{i\mathbf{Q}\cdot\mathbf{r}'}h(\mathbf{r}')\right)d\mathbf{Q}\right]$$
$$(4.12)$$

where $h(\mathbf{r}) = g(\mathbf{r}) - 1$ is the indirect correlation function. $G(z)$ is now separated in two parts. The first term is only due to the form factor. It corresponds with $\eta = 0$ in Fig.4.2. The second term is a function of the form factor and the indirect correlation function. The indirect correlation function is equal to -1 in the region $0 \le r \le 2R$ and for $r > 2R$ it is oscillating around 0. Therefore, in Eq.4.12 the second term gives a negative contribution for $0 \le r \le 400$. This means that in Fig. 4.2 we subtract from the curve corresponding to $\eta = 0$ a positive quantity which comes from the second term in Eq. 4.12. This is the reason why the first minimum in Fig. 4.2 becomes more negative with increasing volume fraction. For $R > 400$ the first term in Eq. 4.12 is actually 0. Because the second term is a function which oscillates around zero, we have positive and negative values of the SESANS correlation function. The peaks are related to the higher correlation in the system.

Large polydispersity will smear out the interaction effect. The width of the minimum at $z = 325$ nm in Fig. 4.2 is 75 nm. So polydispersities up to 25 % will not effect the curve. Beyond 25 %, polydispersities will show smearing out of the interaction effect.

4.2.3 Effect of structure factor; sticky hard-sphere model

Another model for the structure factor is the sticky-hard sphere model. It consists of particles interacting via very short ranged square well potentials. It can be applied in colloidal particles, microemulsion systems, and non-ionic micellar solutions [32]. The parameters of the model are the volume fraction η, $u_0/(k_B T)$ where u_0 is the depth of the potential well and T the temperature and σ/a in which σ is the particle diameter and a is a range of which is assumed that the correlation function vanishes beyond it. The structure factor is then written as [32]:

$$S(Q) = \frac{1}{A(Q)^2 + B(Q)^2} \tag{4.13}$$

where:

$$A(Q) = 1 + 12\eta'\left(\alpha\left[\frac{\sin(\kappa) - \kappa\cos(\kappa)}{\kappa^3}\right] + \beta\left[\frac{1 - \cos(\kappa)}{\kappa^2}\right] - \frac{\lambda}{12}\frac{\sin(\kappa)}{\kappa}\right) \tag{4.14}$$

$$B(Q) = 12\eta'\left(\alpha\left[\frac{1}{2\kappa} - \frac{\sin(\kappa)}{\kappa^2} + \frac{1 - \cos(\kappa)}{\kappa^3}\right] + \beta\left[\frac{1}{\kappa} - \frac{\sin(\kappa)}{\kappa^2}\right] - \frac{\lambda}{12}\left[\frac{1 - \cos(\kappa)}{\kappa}\right]\right)$$
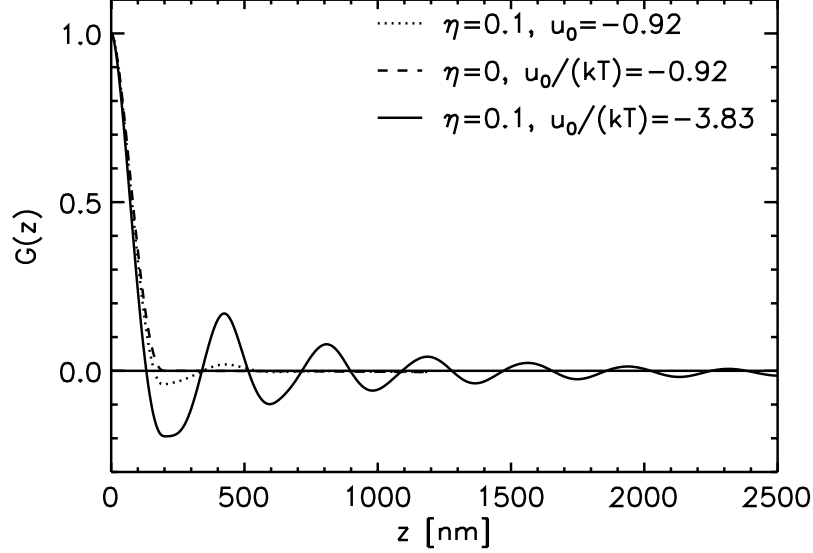
Figure 4.3: Correlation function of spheres interaction with a sticky hard-sphere potential with a diameter of 200 nm. The calculation has been done for volume fractions of 0 and 0.1 with a potential depth of -0.92 and -3.83.

with $\kappa = Qa$. Furthermore,:

$$
\begin{aligned}
\epsilon &= 1 - \frac{\sigma}{a} \qquad\qquad\qquad\qquad\qquad\qquad (4.15) \\
\eta' &= \eta \left(\frac{a}{\sigma} \right)^3 \\
\tau &= \frac{1}{12\epsilon} e^{u_0/(k_B T)} \\
\lambda &= \frac{-6(2 + \eta')}{(\eta' - 1)(-\eta' + 13\eta'^2 + 12\tau - 12\eta'\tau)} \\
\mu &= \frac{\lambda\eta'}{1 - \eta'} \\
\alpha &= \frac{1 + 2\eta' - \mu}{(1 - \eta'^2)} \\
\beta &= \frac{-3\eta' + \mu}{2(1 - \eta')^2}.
\end{aligned}
$$

In Fig. 4.3 the dashed line is calculated with $\eta = 0$ and $\sigma = 200$ nm. The structure factor evaluates to 1 and the largest length is 200 nm. The dotted line is calculated with $\eta = 0.1$ and $u_0/(k_B T) = -0.92$, see [32] for the choices
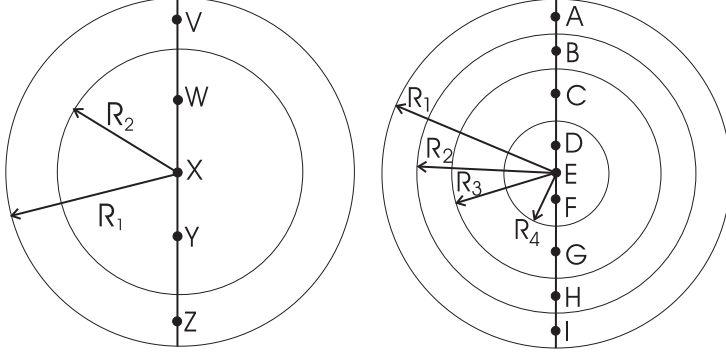
Figure 4.4: One and three shell systems. For the one shell case R_1=200 nm and R_2=140 nm. For the three shell case R_1=200 nm, R_2=160 nm, R_3=120 nm and R_4=60 nm.

of the parameters. Due to the interaction with the surrounding particles we see oscillations. If we increase $u_0/(k_B T)$ to -3.83 then the amplitude of oscillations increase. This is what could be expected, since the stronger interactions give rise to stronger correlations.

4.3 Multishell model

The spherical multishell model has already been calculated by Bouwman [33]. This model was chosen in analogy with calculations of the distance distribution function by Glatter [34]. In this section we will give a quantitative interpretation of the observed maxima and minima in the correlation function.

The form factor for spherical shells with radii R_i and scattering length density ρ_i can be given by [29]:

$$F(Q) = \frac{1}{M} \left[\rho_1 v(R_1) F_s(Q, R_1) + \sum_{i=2}^{N} (\rho_i - \rho_{i-1}) v(R_i) F_s(Q, R_i) \right] \quad (4.16)$$

$$M = \rho_1 v(R_1) + \sum_{i=2}^{N} v(R_i)(\rho_i - \rho_{i-1})$$

where $v(R)$ is the volume of a sphere with radius R, $F_s(Q)$ is the form factor for a sphere as given in Eq. 4.6 and M the total scattering length. We have considered the one shell and the three shell case as shown in Fig. 4.4

The following scattering length density was used for the calculations with
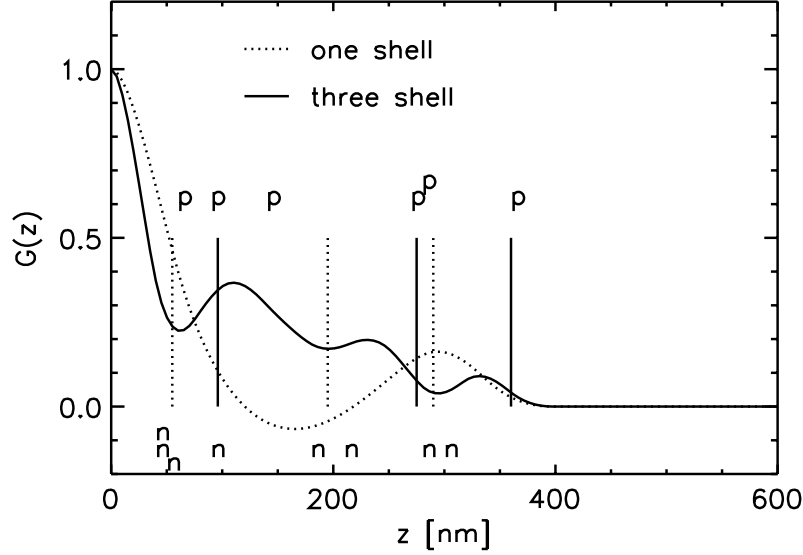
Figure 4.5: Correlation function for multishell model with one and three shells. The positions for the positive and negative correlations for the three shell system are denoted by p,n, respectively. The expected positions of the maxima and minima of the three shell system are shown by full- and dashed-vertical bars respectively. The expected positions for the minima are 55 nm, 195 nm and 290 nm. The expected positions for the maxima are 96 nm, 275 nm and 360 nm.

one shell:

$$\rho = \begin{cases} 1 & \text{if } 0 \leq R \leq 140 \\ -1 & \text{if } 140 \leq R \leq 200. \end{cases} \tag{4.17}$$

In case of three shells the scattering length density was:

$$\rho = \begin{cases} 1 & \text{if } 0 \leq R \leq 60 \\ -1 & \text{if } 60 \leq R \leq 120 \\ 1 & \text{if } 120 \leq R \leq 160 \\ -1 & \text{if } 160 \leq R \leq 200. \end{cases} \tag{4.18}$$

In Fig. 4.5 the multishell model has been calculated with one and three shells. For both cases there is no correlation after 400 nm. Minima in the graph indicate regions of opposite scattering length density. In the case of one shell there is one maximum and one minimum. For the three shell model one has three maxima and three minima. Further conclusions can be drawn by considering the most probable distances. These distances are obtained

Table 4.1: Positive correlations for the three shell case. See the text for the explanation of the symbols.

++ correlation			$--$ correlation		
AC	AG	AI	BE	BH	DF
90	270	360	140	280	60

by connecting any of the points V to Z and A to I for the one and three shell case respectively with each other. The points for the shells are at half distance of the shell thickness. For example, V and A are at 170, 180 nm for the one shell and three shell case, respectively. There are $++$, $--$, $-+$ and $+-$ correlations in the systems. $++$ and $--$ are not distinguishable. The $+-$ and $-+$ distances are also not distinguishable.

In the one shell system we can easily explain the locations of the minimum and maximum. For the one shell case we have a $++$ correlation at $|VZ|=340$ nm, a $+-$ correlation at $|VX|=170$ nm and a $--$ correlation at 140 nm. Therefore, it is to be expected that the $++$ correlation will produce a maximum at 340 nm and the $+-$ correlation a minimum at 170 nm. This is in good agreement with the observed positions. The $--$ correlation at 140 nm will be hidden in the positive beginning part of the curve.

The situation is more complicated for the three shell case. In Tab. 4.1 and Tab. 4.2 all characteristic distances occurring are tabulated. These distances are also shown in Fig. 4.5. The $++$ and $--$ correlations will give rise to positive correlations and are denoted by p in the figure whereas the $+-$ and $-+$ correlations will lead to negative correlations and are denoted by n. One can see that some distances form a group. For example, around 200 nm one has negative correlations of 180 and 210 nm . By averaging these we obtain the expected position for the minima. All maxima and minima are denoted as vertical and dashed-vertical bars, respectively. The positions for the minima and maxima are 55 nm, 195 nm, 290 nm and 96 nm, 275 nm, 360 nm. This is in good agreement with the calculated curve.

It is clear that the length scales over which positive and negative correlations occur can be read out directly from a SESANS measurement.

Again, polydispersity influences the curve. If we consider the last minimum in Fig. 4.5, 25 % polydispersity will smear out this structure. That gives a limit to the interpretation of SESANS measurements on shell systems.

Table 4.2: Negative correlations for the three shell case. See the text for the explanation of the symbols.

+− correlation			−+ correlation				
AB	AE	AH	BC	BE	EG	EI	HI
40	210	300	50	280	90	180	40

4.4   Ellipsoid of revolution

For an ellipsoid of revolution with semi axes R, R and εR the square of the form factor is given by [29]:

$$F_e^2(Q, \varepsilon) = \int_0^{\pi/2} F_s^2(Q\, r(R, \varepsilon, \alpha)) \sin(\alpha) d\alpha \qquad (4.19)$$

where $r(R, \varepsilon, \alpha) = R(\sin(\alpha)^2 + \varepsilon^2 \cos(\alpha)^2)^{1/2}$. The calculations are done for three values of ε: 0.3, 1 and 3. For each value of ε the radii are chosen from the value of the volume for $R = 200$ nm. This is done in order to have the same amount of scattering from the three ellipsoids. The volume of the ellipsoid is given by $4/3\pi R^3 \varepsilon$. The corresponding radii for increasing values of ε are 298.76 nm, 200 nm, 138.67 nm. It can be seen from Fig. 4.6 that the three correlation functions are not the same. For $R = 200$ nm the largest length over which correlations occur is 400 nm. As can be seen from the graph there are no correlation above 400 nm (dotted line). For $\varepsilon = 0.3$ the largest length is $2 \times 298.76 = 596$ nm. From the graph we see that the corresponding curve is almost zero above 550 nm. This is because for increasing lengths the correlations decrease. There is actually one length of 596 nm in the ellipsoid ,i.e the one from one pole to the other of the ellipsoid. For $\varepsilon = 3$ the largest length is $2 \times 139 \times 3 = 834$ nm. It can be seen from the graph that the correlation function vanishes at larger distances. Between 50 nm and 200 nm the curve for the sphere is larger than for the oblate an prolate ellipsoids. This is because for the sphere all distances occur with the same probability. At very small distances these curves come together because the probability of finding these small distances is the same for the three cases. This is comparable to the situation for the distance distribution function [34].
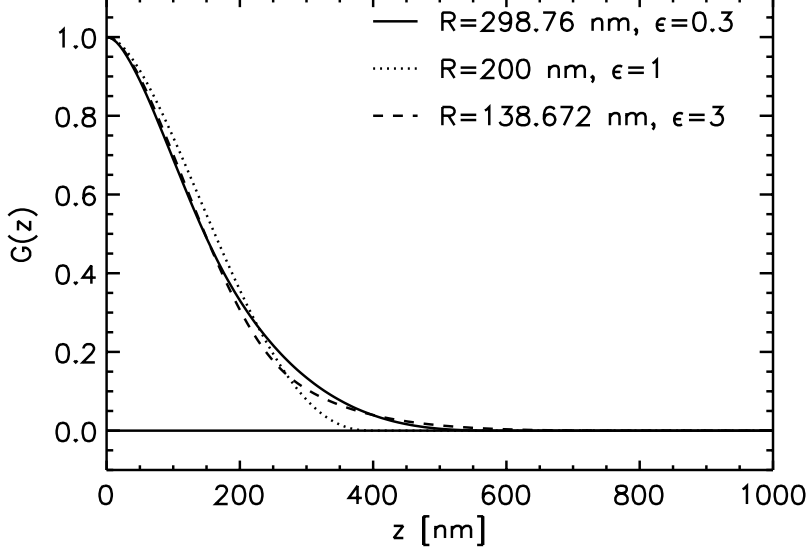
Figure 4.6: Correlation function of an ellipsoid of revolution with semi-axis of R and ϵR. In each case, the radii are chosen in such a way that the total volumes of the ellipsoids are the same. For large z the curve for the prolate sphere is larger than that for the oblate and perfect sphere. In the range of 50 t0 200 nm the the curve for the perfect sphere is larger than the prolate and oblate sphere. For small z values the correlation curves of the three spheres come together.

4.5 Cylindrical model

The expression for a cylinder of radius R and length L is given by [29]

$$F_c^2(Q) = \int_0^{\pi/2} \left[\frac{2j_1(QR\sin(\alpha))}{QR\sin(\alpha)} \frac{\sin\left(QL\cos(\alpha)/2\right)}{(qL\cos(\alpha))/2} \right]^2 \sin(\alpha)d\alpha \qquad (4.20)$$

where $j_1(x)$ is the first order Bessel function. In Fig. 4.7 correlation functions for three cylinders are calculated. The height of the cylinders L is 100 nm in each case. The largest correlation for a cylinder is at $(R^2 + L^2)^{1/2}$. For the cylinder with $R = 15$ nm, $R = 30$ nm and $R = 80$ nm these are at 101 nm ,104 nm and 188 nm, respectively which is in good agreement with the graph.

The value of the radii for the cylinders with $R = 15$ nm and $R = 30$ nm at half-height are 16 nm and 29 nm. For the cylinder with $R = 80$ nm the half-height value is 60 nm. Therefore, for $R \leq L/2$ the half-height value is a
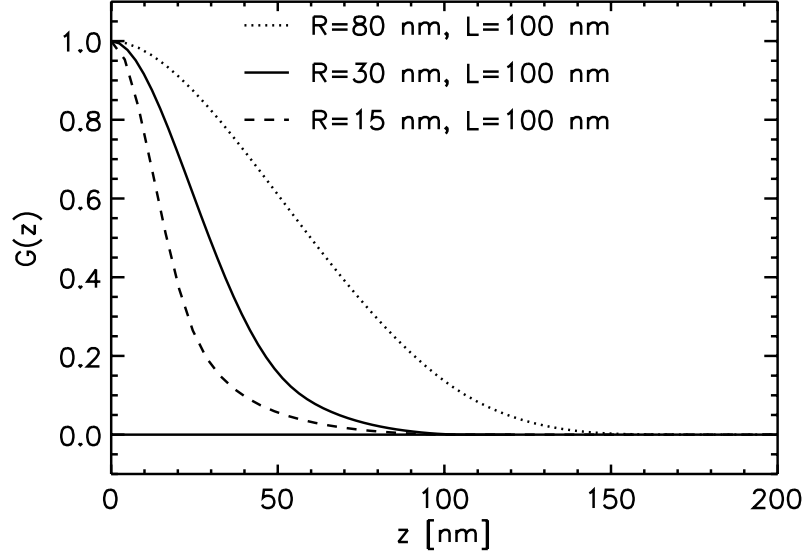
Figure 4.7: Correlation function for three cylinders with a height of 100 nm and radii of 15, 30 and 80 nm. The radii at half-height are 16, 29 and 60 nm.

good measure for the radius.

4.6   Debye-Lorentz model

This model can be used in randomly distributed systems such as fractal systems. The form factor is given by [35]

$$F_d = \frac{1}{(1 + (\xi Q)^2)^p} \tag{4.21}$$

where p depends on the dimensionality of the system and ξ is the correlation length. Fig. 4.8 shows that for different values of p the $G(z)$ is very different. In the calculations ξ is taken to be 200 nm. The correlation functions stretch out over larger distances. This is to be expected, because in momentum space for large p Eq. 4.21 falls off very rapidly. The opposite is true in real space.

If one takes the integration boundaries infinite in Eq. 4.1 analytical expressions can be obtained for $G(z)$ i.e. $Q_{ym} \to \infty$ and $Q_{zm} \to \infty$.
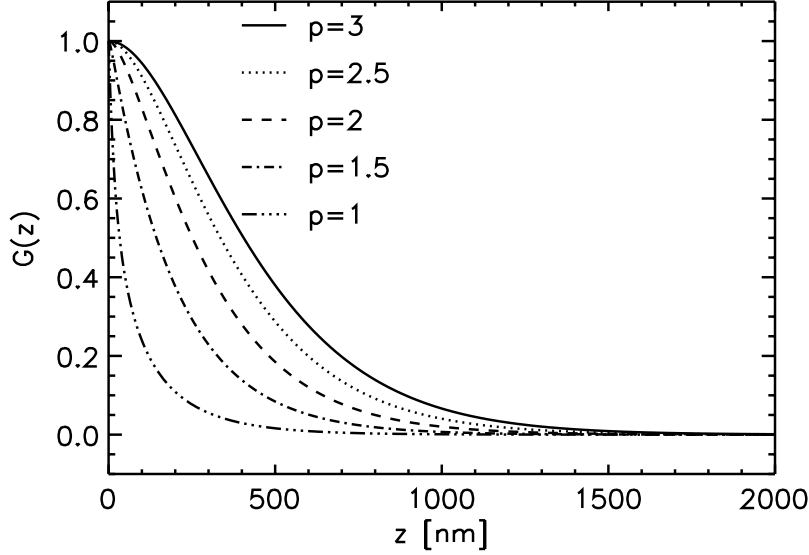
Figure 4.8: Debye-Lorentz model for varying values of p with a correlation length ξ of 200 nm.

The integral to be evaluated is

$$I(z) = \int_{-\infty}^{\infty} \int_{-\infty}^{\infty} \frac{\cos(q_z z)}{\left(1 + \xi^2(q_y^2 + q_z^2)\right)^p} dq_y dq_z \qquad (4.22)$$

$$= \int_{-\infty}^{\infty} \cos(q_z z) I_1 dq_z$$

where I_1 is

$$I_1 = \xi^{-2p} \int_{-\infty}^{\infty} \frac{1}{(k^2 + q_y^2)^p} dq_y \qquad (4.23)$$

with

$$k^2 = \frac{1 + \xi^2 q_z^2}{\xi^2}. \qquad (4.24)$$

This integral can be evaluated by the following integral: [36]

$$\int_0^{\infty} \frac{dx}{(x^2 + a^2)^n} = \frac{(2n-3)!!}{2(2n-2)!!} \pi a^{1-2n} = \frac{\sqrt{\pi}\Gamma(n-1/2)a^{1-2n}}{2\Gamma(n)}, \qquad (4.25)$$

where the double factorial is defined as $n!! = n(n-2)(n-4)....$ Making use

of Eq. 4.25 $I(z)$ becomes

$$
\begin{aligned}
I(z) &= \frac{\xi^{-2p}k^{1-2p}\sqrt{\pi}\Gamma(p-1/2)}{\Gamma(p)} \times \\
&\quad \int_{-\infty}^{\infty} k^{1-2p}\cos(q_z z)dq_z \\
&= \frac{\sqrt{\pi}\Gamma(p-1/2)}{\xi\Gamma(p)} \int_{-\infty}^{\infty} (1+\xi^2 q_z^2)^{1-2p}\cos(q_z z)dq_z.
\end{aligned}
\tag{4.26}
$$

This integral can be evaluated by the following integral:[36]

$$
\begin{aligned}
&\int_0^{\infty} (\beta^2 + q_z^2)^{\nu-\frac{1}{2}}\cos(q_z z)dq_z \\
&= \frac{1}{\sqrt{\pi}}\left(\frac{2\beta}{z}\right)^{\nu}\cos(\pi\nu)\Gamma(\nu+\frac{1}{2})K_{\nu}(z\beta) \\
&= \left(\frac{2\beta}{z}\right)^{\nu}\frac{\sqrt{\pi}K_{\nu}(z\beta)}{\Gamma(1/2-\nu)}
\end{aligned}
\tag{4.27}
$$

for $a > 0$, $Re(\beta) > 0$ and $Re(\nu) < 1/2$ and where we have used the following property of the Gamma function: $\Gamma(z)\Gamma(1-z) = \pi/\sin(\pi z)$, [37]. In this equation $K_{\nu}(z\beta)$ is the modified Bessel function. By using this in Eq.4.26 we obtain

$$
I(z) = \frac{2^{2-p}\xi^{-1-p}\pi z^{p-1}K_{1-p}(z/\xi)}{\Gamma(p)}.
\tag{4.28}
$$

for $Im(z) = 0$ and $Re(p) > 1/2$. To obtain $G(z)$ we have to evaluate $I(0)$. Due to difficulties in evaluating $I(0)$ by Eq. 4.28, we will evaluate $I(0)$ by putting $z = 0$ in Eq.4.26 and carry out the integration over q_z by using Eq.4.25. After doing so we obtain

$$
I(0) = \frac{\pi\Gamma(p-1)}{\xi^2\Gamma(p)}.
\tag{4.29}
$$

Finally, we have for $G(z)$

$$
G(z) = \frac{I(z)}{I(0)} = \frac{2^{2-p}}{\Gamma(p-1)}\left(\frac{z}{\xi}\right)^{p-1}K_{1-p}(z/\xi)
\tag{4.30}
$$

for $p > 1$. We cannot develop this equation for general p. In the next paragraphs we will investigate $G(z)$ for specific values of p.

p=3

$$G(z) = \frac{1}{2}\left(\frac{z}{\xi}\right)^2 K_2(\frac{z}{\xi}). \tag{4.31}$$

For $z \ll \xi$ we can develop $K_2(\frac{z}{\xi})$. An expansion up to fifth order gives $K_2(\frac{z}{\xi}) = -1/2 + 2\xi^2/z^2$. Substituting this in Eq. 4.31 gives for $G(z)$

$$G(z) = 1 - \frac{1}{4}\left(\frac{z}{\xi}\right)^2 + O(z^4). \tag{4.32}$$

From the constant term of a $\ln(1 - G(z))$ vs. $\ln(z)$ plot one can determine ξ.

p=2.5

$$G(z) = (1 + \frac{z}{\xi})e^{-z/\xi}. \tag{4.33}$$

For small z we can develop Eq. 4.33. We obtain

$$G(z) = 1 - \frac{1}{2}\left(\frac{z}{\xi}\right)^2 + O(z^3). \tag{4.34}$$

The constant term in a double logarithmic plot will contain ξ.

p=2

$$G(z) = \frac{z}{\xi}K_1(\frac{z}{\xi}). \tag{4.35}$$

In this case we have to expand at least up to third order. The expansion gives for $G(z)$

$$G(z) = \frac{z}{\xi} - 0.308\left(\frac{z}{\xi}\right)^3 + 0.5\left(\frac{z}{\xi}\right)^3 ln(\frac{z}{\xi}). \tag{4.36}$$

It is not possible from a simple logarithmic plot from this equation to obtain ξ.

p=1.5

$$G(z) = e^{-z/\xi}. \tag{4.37}$$

In this case there are no inflection points. However, if we make a logarithmic plot then the slope will give us $1/\xi$.
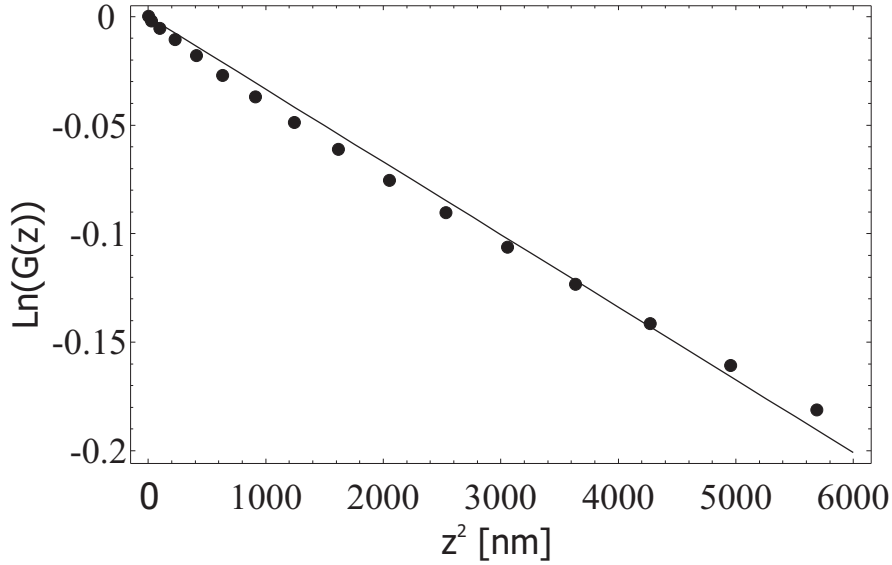
Figure 4.9: $\ln(G(z))$ vs. z^2 plot for monodisperse spheres of 200 nm radius. The radius of gyration and hence the radius are obtained from the slope.

4.7   Small-angle approximation

One important approximation in SANS is the small-angle approximation or the Guinier approximation. In this section we will investigate the $G(z)$ for small angle approximation. In some cases the main information in the scattering process will be contained in the small angle range. Only in this case we can use the Guinier approximation for SESANS, whereas in SANS one can always investigate the scattering curve for small Q. The reason for this is that in SESANS one actually integrates over all the Q range. For the form factor we will use [7]

$$F_g(\mathbf{Q}) = e^{-\frac{R_g^2 Q^2}{3}}. \tag{4.38}$$

If we substitute this in Eq. 4.1 and carry out the integration with infinite boundaries we obtain for $G(z)$

$$G(z) = e^{-\frac{3z^2}{4R_g^2}}. \tag{4.39}$$

If we compare Eq. 4.39 with Eq.4.38 we see that R_g appears in the SESANS case in the denominator. This is because in SESANS one measures in real space whereas in SANS in momentum space.

The small-angle approximation is valid for small z. It is not valid for the whole z range. This can be understood as follows: In SESANS, the form

factor is multiplied with a cosine factor and integrated over Q. The spin-echo length z, see Eq. 4.1 controls the frequency of the cosine. In the small-angle approximation for the form factor, only the small Q region contains the relevant information on the radius of the particles. Large z values mean that the form factor is multiplied with a highly oscillating cosine. Therefore, after integration over Q, the small Q region will not contribute much to the signal for large z values.

The integration in Eq. 4.1 can be carried out because the contribution of the integrand for large Q is negligible. One can obtain by Eq. 4.39 the radius of gyration and hence the radius of the particles as in SANS. To illustrate this we will use the curve for the monodisperse sphere of R=200 nm radius in Fig. 4.1. If we make a $\ln(G(z))$ vs. z^2 plot for small z we obtain from the slope, according to Eq. 4.39, R_g and hence R. In Fig. 4.9 this plot and a linear fit is shown. The fit is $-3.35 \times 10^{-5} z^2$. $R_g = \sqrt{\frac{3}{4} \frac{1}{3.35 \times 10^{-5}}} = 150$ nm. So, $R = (5/3)^{1/2} \times R_g = 193$ nm which corresponds well with the actual value of 200 nm.

4.8 Conclusions

The correlation function that is measured with SESANS gives direct information on the structure of a sample as illustrated with different model calculations.

The length scales present in the sample can directly be determined as illustrated with calculations on spheres, cylinders and ellipsoids. Determination of Gaussian polydispersity cannot be determined by SESANS. The Guinier approximation can be applied in SESANS in the same manner as in conventional SANS and gives thus in the same way information about the important length scales in the system.

The effect of correlations between particles shows up clearly in SESANS. One can separate the SESANS correlation function in two parts: One part is only a function of the shape of the particle and the other part is a function of the shape and the interference between the particles.

The length scales over which positive and negative correlations are present is shown by calculations on spherical multishell systems. The positions of the maxima and minima can be predicted fairly well.

The dimensionality of the studied structure of which the form factor can be described by a Debye-Lorentz like model can be determined from the correlation function. An analytical expression is obtained for this kind of correlation function. The correlation function stretches out over larger distances when the dimensionality of the system increases. Furthermore, if one

knows the dimensionally of the system beforehand the correlation length can ce determined directly.

Chapter 5

Measurements

5.1   Introduction

In this chapter we will show SESANS measurements. These measurements
are performed on the first prototype SESANS instrument at the Interfaculty
Reactor Institute in Delft. The first measurements are done on limestone
which turned out to be a convenient choice, since it gives a lot of scattering.
In the first section we will show the SESANS measurements on limestone and
hence that the SESANS principle works. A drawback of the first SESANS
instrument is that the z range is limited to 250 nm and therefore, it is not
possible to collect a full data set for the limestone measurements. Further,
the limestone measurements are used to show that the multiple scattering
formula derived in chapter 1 is correct.

In section 2 we will show measurements on polystyrene spheres of 100 and
60 nm. Since all characteristics of these particles are known, it is possible to
calculate the expected spectrum without any adjustable parameters. In this
way the first quantitative comparison can be made.

5.2   Limestone

The first SESANS measurements at IRI were obtained from scattering from
BCR-limestone powder (CRM 116) which is a certified laboratory powder
[38]. Limestone is constituted for more than 99.7 % of calcite of which the
chemical formula is $CaCO_3$ [39, 40]. There are no less than three phases of
$CaCO_3$ which are aragonite, vaterite and calcite. Arogonite is orthorombic,
vaterite is hexagonal and calcite is trigonal (R$\bar{3}$c). The most encountered
phase of these minerals in nature is calcite [41] of which the lattice parameters
are $a = b = 4.99$ Å, $c = 17.06$ Å and it has a unit cell volume of 367.85 Å^3
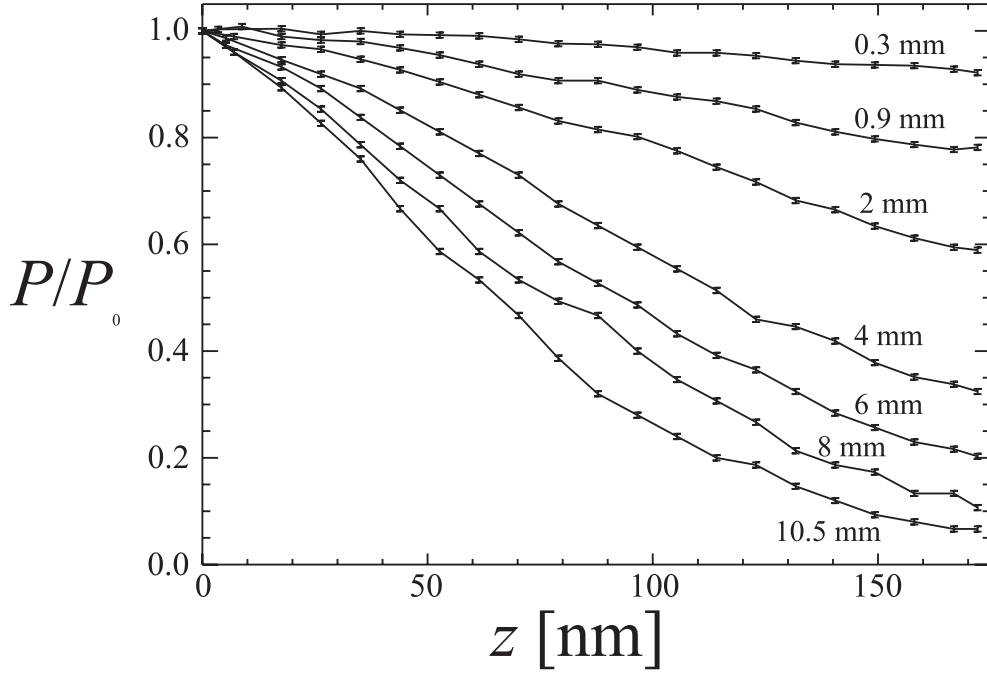
Figure 5.1: SESANS signal of several thicknesses of limestone powder. The measurements were performed at IRI, Delft with a magnetized foil set–up. A wavelength of $\lambda = 2.05$Å was used. The signal is due to the surface structure of the powder particles or due to double Bragg scattering.

[42]. The mean particle diameter of BCR-limestone powder is 4 μm [38]. In Fig. 5.1 measurements with different sample thicknesses are shown. The measurement setup is as shown in Fig. 1.5. The sample position s_x is varied to change the spin-echo length z, Eq.1.20.

The largest spin-echo length in the measurement is 175 nm. So, the origin of the signal cannot be attributed to the size of powder particles, since these have a diameter of 4 μm. Therefore, the signal can be due to the surface structure of the powder particles or due to the holes between the particles. The surface structure can be described by scattering from fractal systems. The fractal dimension D_f for surface fractals of bodies with sharp interfaces and spheres is 4 [43]. This means that we can use Eq.4.35 with $p = 2$ ($p = D_f/2$) for describing the data:

$$G(z) = \frac{z}{\xi} K_1(\frac{z}{\xi}). \tag{5.1}$$
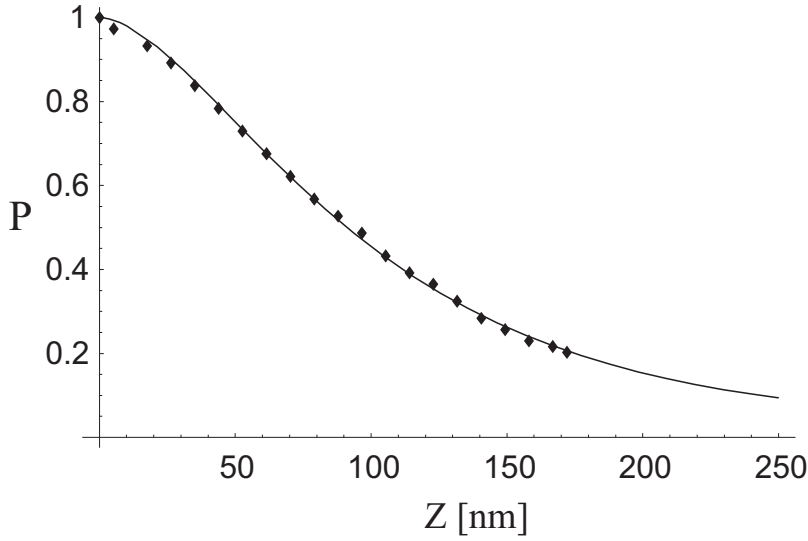
Figure 5.2: Fit of 6 mm thick limestone data. The fit results are $T = 5.59 \cdot 10^{-3}$ and $\xi = 218$ nm

The polarization is then given by Eq.1.32:

$$P(z) = T^{(1-G(z))}. \tag{5.2}$$

where T is the transmission. In Fig. 5.2 scattering from 6 mm thick limestone data is fitted with Eq.5.2. The fit and the data are in good agreement. The fit results are $T = 5.59 \cdot 10^{-3}$ and $\xi = 218$ nm. However, it should be noted that in the measurement the level of T was not measured due to the limited z range. Therefore, the parameters T and ξ are correlated.

   Another possibility for the origin of the signal is double Bragg diffraction. The Bragg law is given by:

$$\sin(\theta/2) = \frac{\lambda}{2d} \tag{5.3}$$

where d is the lattice spacing. The incoming beam can be scattered double over large angles so that the beam makes a small angle with respect to the incoming beam direction. This gives rise to small-angle scattering. However, there will be no Bragg scattering at all if [44]:

$$\lambda > 2d_{max} \tag{5.4}$$

since then Eq.5.3 cannot be satisfied. d_{max} can be calculated by the software package PowderCell for the above given cell parameters of limestone and $\lambda = 2.05$ Å. This gives $d_{max} = 3.854$ Å. This means that the used wavelength
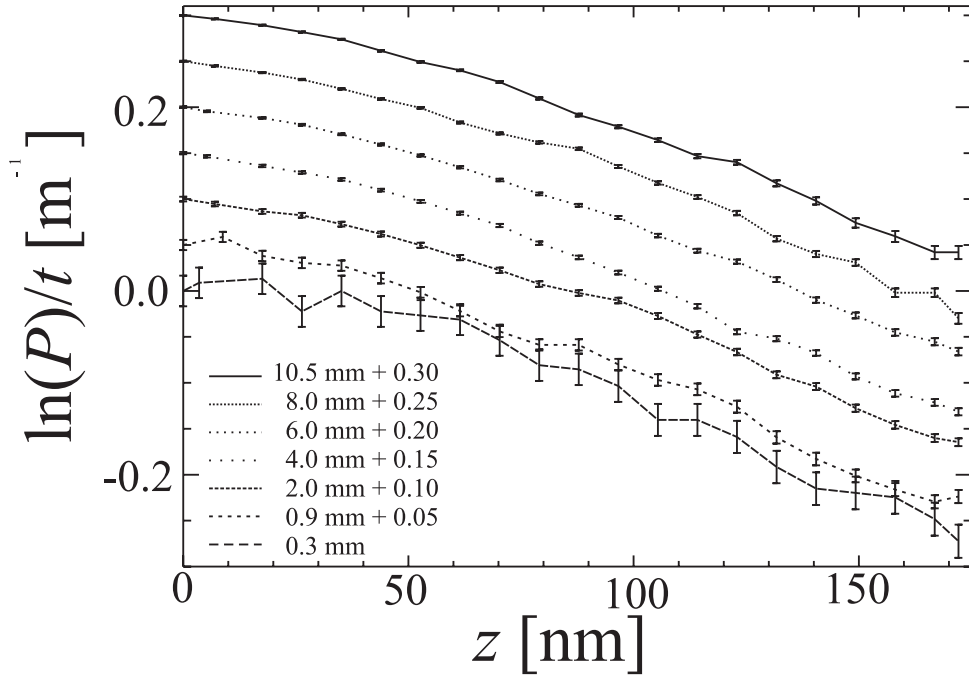
Figure 5.3: Data in Fig. 5.1 scaled according to Eq.(1.34) with the thickness to obtain the shape of the correlation function $G(z)$. The curves collapse on one single curve when they are plotted on the same scale. Only the counting statistics are taken into account in the error bars. To highlight the differences in the error bars in the curves, thicker curves have each been shifted in scale by 0.05 mm^{-1} with respect to each other.

should be larger than 7.708 Å in order to have no Bragg scattering. Therefore, it is possible that the signal is due to double Bragg scattering. However, we are not interested with the limestone measurements in the origin of the signal but only in obtaining a signal.

5.3   Multiple scattering

Multiple scattering results in peak broadening in conventional SANS. In SESANS it results therefore in stronger decay of the polarisation as a function of z as one can see in Fig. 5.1. Not only the amount of depolarisation changes, but also the shape becomes more narrow for thicker samples. Scaling the polarisation according to (1.34) gives a collapse of all the data on one single curve which is directly proportional to the correlation function $G(z)$

as shown in Fig.5.3. This shows that the formalism works. The error bars in the logarithmic plot is given by:

$$\Delta\left(\frac{\ln(P/P_0)}{t}\right) = \frac{\Delta(P/P_0)}{P/P_0} \cdot \frac{1}{t} \tag{5.5}$$

This means that for each curve the larger the depolarization the larger the error bars in the logarithmic plot, since $\Delta(P/P_0)$ is constant. This is clearly seen in the 0.3 mm curve in Fig.5.3. Another point is that there is an optimum thickness t for which the error bars are the smallest. Thus it is important to choose t carefully.

5.4   SESANS measurements on colloids

In this section we will show the first quantitative SESANS measurements. The measurements are done on totally characterized polystyrene spheres. This allows us to calculate the polarization as a function of the spin-echo length z which are the measured quantities in a SESANS experiment.

Polystyrene spheres with a radius of 60 and 100 nm were used from Bangs Laboratories, Inc., Indiana, USA (www.bangslabs.com). The coefficient of variation is claimed to be ~ 0.01. The original samples are suspensions with a concentration of $\eta_0 = 10\%$ in H_2O. D_2O is added to increase the contrast. The initial volume fraction is:

$$\eta_0 = \frac{V_{ps}}{V_{ps} + V_{H_2O}}, \tag{5.6}$$

where V_{ps} and V_{H_2O} are the volumes of polystyrene and H_2O, respectively. The initial mass m can be written as:

$$m = m_{ps} + m_{H_2O} = \delta_{ps}V_{ps} + \delta_{H_2O}V_{H_2O}. \tag{5.7}$$

Eq.5.6 and Eq.5.7 is a set of two equations with two unknowns, V_{ps} and V_{H_2O}, which can be solved in terms of η_0, m, δ_{ps} and δ_{H_2O}. The solutions can then be substituted in Eq.5.6.

By doing so the volume fraction of polystyrene and similarly that of H_2O and D_2O are, respectively,:

$$\begin{aligned}
\eta_{ps} &= m\delta_{D_2O}\eta_0 v^{-1} \\
\eta_{H_2O} &= m\delta_{D_2O}(1-\eta_0)v^{-1} \\
\eta_{D_2O} &= 1 - m\delta_{D_2O}v^{-1}
\end{aligned}$$

$$\tag{5.8}$$

with:
$$v = m\delta_{\text{D}_2\text{O}} + m_{\text{D}_2\text{O}} \left(\delta_{\text{H}_2\text{O}}(1 - \eta_o) + \delta_{\text{ps}}\eta_0 \right). \tag{5.9}$$

Here m is the total mass of the mixture before addition of D$_2$O. $\delta_{\text{H}_2\text{O}}$, $\delta_{\text{D}_2\text{O}}$ and δ_{ps} are the densities of H$_2$O, D$_2$O and polystyrene and have the values 1 g.cm^{-3}, 1.1 g.cm^{-3} and 1.05 g.cm^{-3}, respectively.

With these equations the contrast is then given by:
$$\Delta\rho = \rho_m - \rho_{ps} \tag{5.10}$$

where $\rho_{ps} = 1.42\,10^{14}$ m^{-2} is the scattering length density of the polystyrene spheres and ρ_m is the scattering length density of the matrix which is given by:
$$\rho_m = \frac{\eta_{\text{H}_2\text{O}}}{\eta_{\text{H}_2\text{O}} + \eta_{\text{D}_2\text{O}}}\rho_{\text{H}_2\text{O}} + \frac{\eta_{\text{D}_2\text{O}}}{\eta_{\text{H}_2\text{O}} + \eta_{\text{D}_2\text{O}}}\rho_{\text{D}_2\text{O}} \tag{5.11}$$

Here, $\rho_{\text{H}_2\text{O}} = -0.56\,10^{14}$ m^{-2} and $\rho_{\text{D}_2\text{O}} = 6.38\,10^{14}$ m^{-2} are the scattering length densities of H$_2$O and D$_2$O, respectively.

The total scattering probability, σt, can be calculated by integrating Eq. 1.23 over the whole momentum space with $F(\mathbf{Q}^2)$ given by Eq.4.6. This gives [12]:
$$\sigma t = \frac{3}{2}\eta(\Delta\rho)^2\lambda^2 R t \tag{5.12}$$

For the measurements, the SESANS instrument has been used in the setting as described in 1.5 with a wavelength of $\lambda = 0.224$ nm. The spin echo length z was again varied by changing the distance s_x between the sample and the last magnetized foil. Further $L = 150$ cm, $B = 55.0$ mT. The polarization of the beam without any sample was $P_0 = 0.73$. The samples were contained in quartz cuvettes with a thickness of $t = 10$ mm. The height and the width of the diaphragms are respectively 4.5 mm and 7 mm.

In Fig. 5.4, measurement of the polarization as a function of the spin-echo length is shown for the 100 nm spheres. The mass of the mixture, m, before addition of D$_2$O was 0.43 g. 1.4 g D$_2$O, $m_{\text{D}_2\text{O}}$, was added to this mixture. One can calculate now by Eq.5.8 to Eq.5.11 the volume fraction of polystyrene and the contrast before and after addition. The volume fraction decreased from $\eta_{\text{ps}} = 0.1$ to $\eta_{\text{ps}} = 0.0251$ whereas the scattering length density increased from $\Delta\rho = -1.98 \cdot 10^{14}$ m^{-2} to $\Delta\rho = 3.35 \cdot 10^{14}$ m^{-2}. σt is then 0.210. With these values the polarization can be numerically calculated by Eq.1.32, Eq.1.22 and Eq.4.6. The calculated polarization is also shown in Fig. 5.4. The measurement and the calculation agrees well in shape. Note that the saturation level is equal to σt. A direct visual interpretation of the measurement is possible. There are no correlations with a length scale longer than 200 nm.
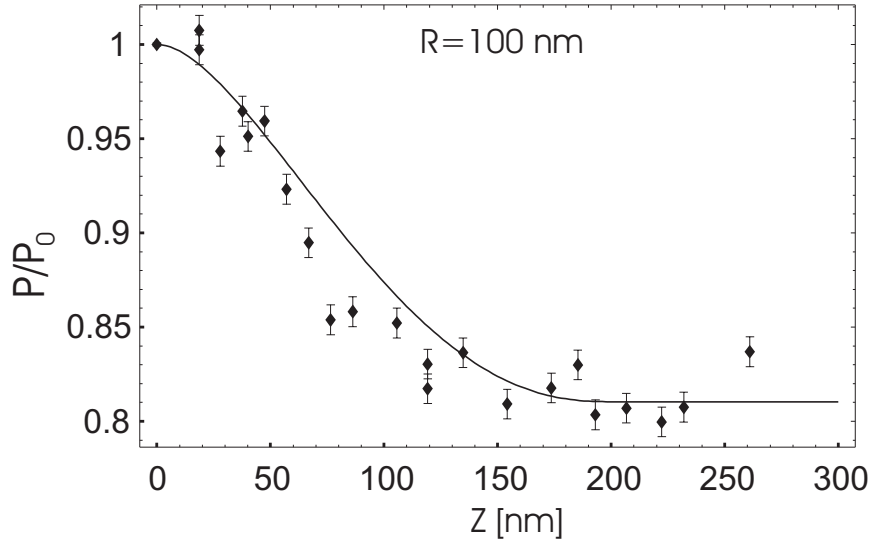
Figure 5.4: Measured and calculated polarization for spheres of 100 nm.

In Fig. 5.5, measurement and calculation of the polarization for spheres of 60 nm radius is shown. In this case $m = 0.4$ g and $m_{D_2O} = 1.19$ g. As a result the volume fraction decreases from $\eta_{ps} = 0.1$ to $\eta_{ps} = 0.0268$ whereas the scattering length density increased from $\Delta\rho = -1.98 \cdot 10^{14}$ m^{-2} to $\Delta\rho = 3.24 \cdot 10^{14}$ m^{-2}. σt is 0.127. In this case, the measurement and the calculation do not agree very well. The total scattering in the measurement is 0.15 whereas in the calculation it is 0.127. The reason could be the diaphragm opening, since a too small diaphragm opening gives rise to detection of a smaller part of the scattered neutrons which means less depolarization. However, the measurement shows larger depolarization. At the moment, the reason for this difference in the measured curve and the calculation for the 60 nm spheres is not understood.

5.5 Conclusions

The SESANS principle has been demonstrated by measurements of limestone. The scaling formula for multiple scattering has been applied on limestone measurements of different thicknesses. The measurement of the different thicknesses scale with the multiple scattering formula as discussed in chapter 1.

The first quantitative SESANS measurements are done on polystyrene spheres of 100 and 60 nm. The numerical calculation of the expected spectrum from first principles and the measurement of it for the 100 nm spheres
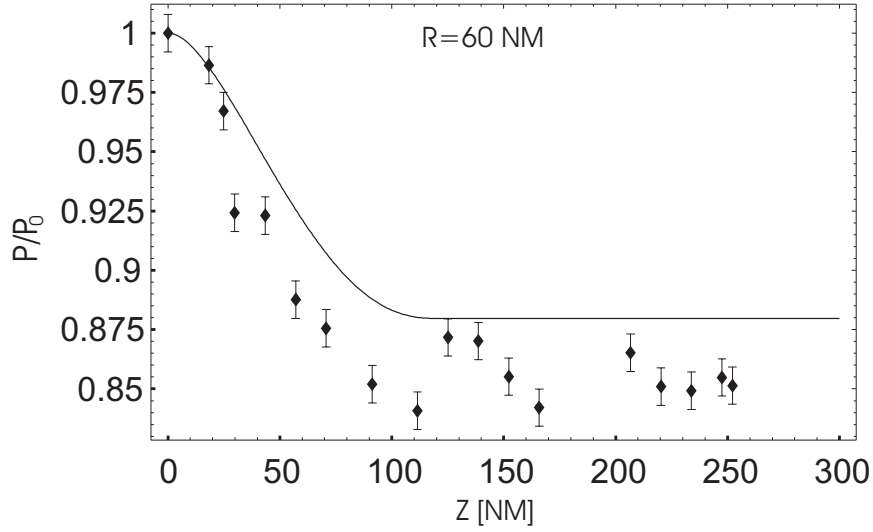
Figure 5.5: Measured and calculated polarization for spheres of $R = 60$ nm.

Table 5.1: Important parameters of D11 at ILL, LOQ at ISIS and SESANS at IRI.

	D11	LOQ	IRI-SESANS
Q/z-range	$5 \cdot 10^{-4}$ to 0.3Å^{-1}	0.006 to 0.24 Å^{-1}	3-250 nm
incident wavelength	$4.5 \leq \lambda$ (Å) ≤ 20	2.2-10.0 Å at 25 Hz, 2.6-6.7 Å or 6.3-10.0 Å at 50 Hz	2 Å
$\Delta\lambda/\lambda$	9%		1-2 %
flux at sample	$3.2 \cdot 10^7$ cm^{-2} s^{-1}	$2 \cdot 10^5$ cm^{-2} s^{-1}, pulsed	10^4
sample-detector distance	2.5...40.5 m	4.05 m	1.5 m

are in good agreement with each other. In case of the 60 nm spheres, there is a difference between the measurement and the calculation which is not yet understood.

To illustrate the power of this technique we will compare whether it is feasible or not to get similar information at LOQ in ISIS and at D11 in ILL using conventional SANS.

The accessible Q range for the main detector banks at LOQ is $0.006 \, \AA^{-1} \leq Q \leq 0.24 \, \AA^{-1}$, see Table:5.1 [45]. For a momentum transfer Q, the maximum measurable distance D is $D \sim \pi/Q$ [46]. This corresponds in real space with a range of $1.3 \, \text{nm} \leq D \leq 52 \, \text{nm}$. So it is impossible to do the measurements in Fig. 5.4 and Fig. 5.5 at LOQ.

At D11 in ILL the Q range is $5 \cdot 10^{-4} \, \mathring{A}^{-1} \leq Q \leq 0.3 \, \mathring{A}^{-1}$, see Table:5.1 [47]. This corresponds with the following range in real space: $1 \, nm \leq D \leq 628 \, nm$. So it is just possible to do this kind of measurements at D11.

It should also be noted that it is completely impossible to do SANS on these particles with the small source at IRI, since it is impossible to do these measurements at ILL and ISIS.

Chapter 6

Conclusions

SESANS is a real space technique to measure structures in contrast with SANS which is an inverse space technique. The measured quantity is the polarization as a function of spin-echo length which is given for the three foil option by Eq.1.20

$$z = \frac{c\lambda^2 B \cot(\theta_0) s_x}{2\pi} \tag{6.1}$$

If $B = 2000$ G, $\lambda = 0.2$ nm, $\theta_0 = 45^0$ and $s_x = 150$ cm then the maximum z range will be $z_{max} = 885$ nm. For the other SESANS options this value will automatically double. However, this is not a fundamental limit. By increasing θ_0, s_x, λ and B this range can readily be extended far into the micron region.

The minimum measurable correlation length z_{min} depends on the maximum measurable wave vector transfer Q_{max}. This transfer depends on the acceptance angle of the analyzer plus detector which is 3×10^{-2} radians for the Delft setup. This gives $Q_{max} = 0.94$ nm^{-1}. So $z_{min} = \pi/Q_{max} = 3.3$ nm.

In Fig. 6.1 the form factor for a sphere of 100 nm radius, the $\cos(Q_z z)$ factor with z=100 nm and the product of these two functions are plotted. For the form factor $Q_y = 0$ is chosen. The form factor is a rapidly decreasing function which is a general feature in SANS. The measured polarization is proportional to the area under the dashed curve Eq.1.21 and Eq.1.22. This curve only has a significant contribution over the one and a half period of the cosine function. In a SESANS experiment by changing z the area under the product function is calculated. One can also see z as the frequency of modulation. If z is increased the product function will be more oscillatory and the product area will decrease. For high z values the main contribution to the SESANS signal is then from the region around $Q = 0$. This is the most difficult part to measure in conventional SANS.

The spin-echo length is proportional to λ^2. Therefore, SESANS combined
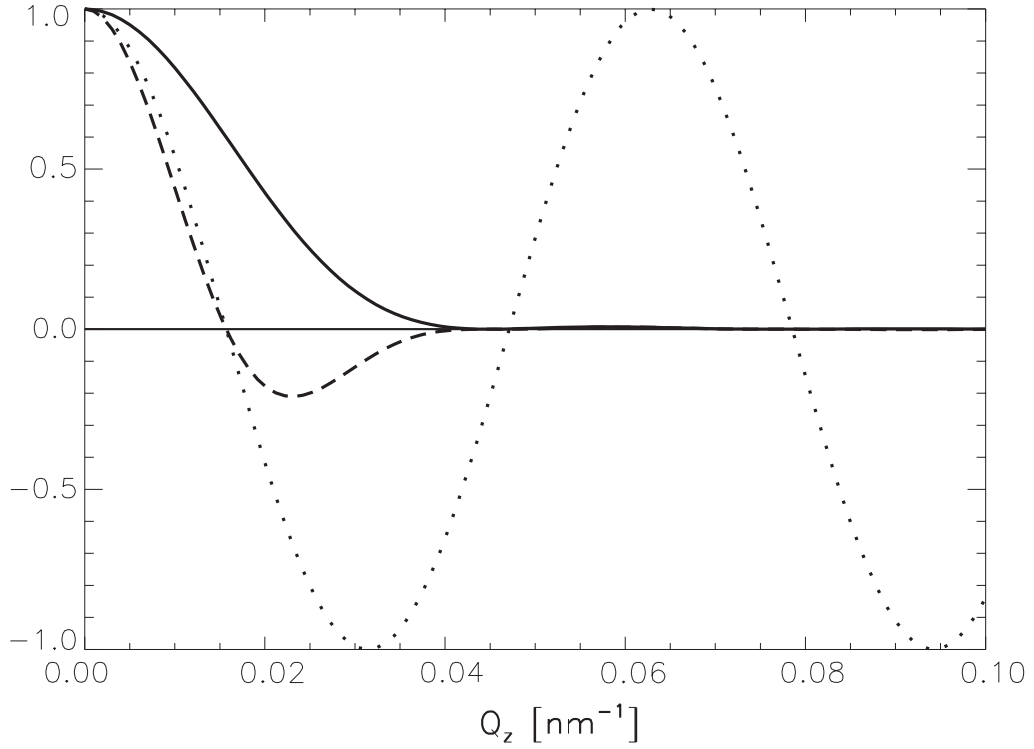
Figure 6.1: The continuous curve is the form factor for a sphere of 100 nm radius. The dotted curve is $\cos(Q_z z)$ with $z = 100$ nm. The dashed curve is the product of the form factor and the cosine term. The area under this curve is proportional to the polarization.

with TOF techniques can be used very effectively at a pulsed neutron source. This means that the spin-echo length is changed by the wavelength for fixed s_x and B. However, z is now changing quadratically instead of linearly. If it will be built, ESS (European Spallation Neutron Source) will be the worlds most powerful pulsed neutron source. The thermal neutron peak flux from ESS (2×10^{17} /cm^2/s) will exceed the constant flux of existing high flux reactors by two orders of magnitude [48]. So, the spin-echo length can be changed very effectively at a source like ESS. Thus in a single shot, whole $P(z)$ can be measured. Furthermore, the high flux will enable to do time dependent SESANS measurements.

The major contribution of SESANS to science will be in the micron region, since the nanometer range is also accessible by conventional SANS. A lot of research can be done in powder technology [38]. The reason for this is that the microstructural behavior of the powder particles have a large effect on the macroscopical behavior. Food science is another field to which

the SESANS technique can contribute. Caseine micelles are an important constituent in milk. It plays a major role in cheese making. SANS measurements on these micelles cover a range from 2-200 nm. For measurements between 200-1000 nm one has to switch to other techniques such as light scattering. With SESANS one can cover this range in a single experiment. Furthermore, neutrons have a large penetration depth compared to light. Additionally, deuterium labelling can be done which is not possible with light. Nowadays, composite materials are used in an increasing number of products. Composites are formed by combining two or more quite different materials to give the composite unique properties. The greatest advantage of composite materials is strength and stiffness combined with lightness. The development of these materials will depend on a fundamental understanding of the microstructure.

SESANS

Summary

Spin-Echo Small-Angle Neutron Scattering (SESANS) is a SANS technique
which can probe distances in real space from a few nanometers up to mi-
crons. With SESANS one can obtain structural information of materials
which means the size and the form of the object. In SANS one obtains data
as a function of momentum transfer. It is very difficult to measure angles
close to zero since then the scattered beam coincides with the incoming beam
and because of this the two dimensional detector must be put at a large dis-
tance from the sample. However, in SESANS data is obtained as a function
of the spin-echo length which corresponds with real space features of the sam-
ple. Each data point automatically includes integration over the momentum
space. Therefore, small angles are included in an measurement as easy as
large angles. Since one measures with SESANS the integrated intensity there
is no need for collimating the beam which means high counting statistics.

The underlying principle of SESANS is the Larmor precession of polarized
neutrons. The setup consists of two precession arms in which the neutrons
effectively precess in opposite directions. When there is no scattering the
amount of precession in the first arm is equal to the amount of precession in
the second arm. This is the echo situation. However, when there is scattering
from a sample, the amount of precession in the two parts will not be the same
due to the traversed path differences which will lead to depolarization of the
beam. The amount of depolarization depends on the structure of the sample.

There are four possibilities to realize a SESANS setup. These are: the
three foil option, wedge option, resonant field option and four foil option.
In all the options dipole magnets are used which generate a magnetic field

perpendicular to the neutron beam direction. In this thesis the three foil option is treated extensively.

In the three foil option single and double foils which are readily magnetized are used as $\pi/2$ and π flippers. The setup consists of three dipole magnets. In the first and last magnets single foils and the middle magnet double foils are mounted. These foils are tilted with respect to the neutron beam direction and form triangular shaped precession regions. The scattering angle is encoded with the precession angle which is proportional to the momentum transfer. The measured quantity is the polarization as a function of the spin-echo length. This length is proportional to the magnetic field value of the magnets, the distance between the sample and magnet and the square of the wavelength. The polarization is proportional to the cosine transform from momentum space to real space of the scattering power of the sample.

Multiple scattering can be treated easily in contrast to SANS. In SESANS multiple scattering results in stronger decay of the polarization as a function of the spin-echo length.

There are two requirements which have to be fulfilled in a SESANS magnet. Firstly, the magnetic fields in the middle of the magnet in a volume of $30 \times 30 \times 30$ mm^3 must homogenous within 1.3 G for a field of 2000 G in the center of the magnet. The reason for this is that the precession angle must be a linear function of the height in order to realize angle encoding. If the field is not homogenous then the precession angle will have a non-linear dependency on the field. The homogeneity of the magnetic field is readily achieved when the width of the pole face of the dipole magnets is 18 cm. To save weight, the radius of the core is brought back to 12 cm, keeping the width of the pole face at 3 cm in order to avoid saturation effects. With these parameters to have 2000 G in the center, a total current of 5000 A is needed through one current package that encloses one pole.

Secondly, the line integral must have a homogeneity of 2.2 G.cm over the beam cross-section which cannot be achieved by increasing the pole gap distance. This inhomogeneity is caused by the fringing of the field lines at the entrance and exit opening of the magnets. Inhomogeneities in the vertical component of the magnetic field will not contribute to the line integral errors but it is proportional to the square of the perpendicular components of the field. Two external coil sets are used to homogenize the line integral over the beam cross-section. The first set consists of four coils. These contain four current carrying wires parallel to the mean beam axis. The distances between the wires are chosen in such a way that it gives a quadratically changing field in both perpendicular directions to the mean beam axis.

This first coil set actually transforms the variation of the line integral

from one perpendicular direction to the other one. The inhomogeneity in this new direction is then corrected with a parabolically shaped coil placed in the neutron beam. For a beam of 15 mm high and 10 mm wide the polarization is increased from 0.25 to 0.86.

Model calculations are performed in order to calculate the SESANS correlation function. The length scales present in systems such as spheres, cylinders and ellipsoids can directly be determined. On the other hand determination of Gaussian polydispersity cannot be done with SESANS for spherical systems. The Guinier approximation can be done in the same manner as with SANS and gives information on the Guinier radius. Structure factor effects shows up clearly in the SESANS signal. For hard sphere interaction, oscillations appear around the zero level of the SESANS correlation function. An analytical expression is obtained for systems which can be described by a Debye-Lorentz model. These calculations show that SESANS allows to do interpretations in real space.

The SESANS principle is demonstrated by measurement of limestone. The scaling formula for multiple scattering has been applied successfully on limestone measurements of different thicknesses.

The first quantitative measurements in Delft are done on latex spheres of 60 and 100 nm. The calculation without any adjustable parameters and the measurement are in good agreement for the 100 nm particles. In case of the 60 nm spheres there is a small difference between the measurement and the calculation which is not yet understood. It would be impossible to these measurements with conventional SANS machines such as at LOQ in ISIS and just possible at D11 in ILL.

SESANS can be used very effectively at a pulsed neutron source since the spin-echo length is proportional to the square of the wavelength. Therefore, it will be possible to obtain the whole depolarization curve as a function of the spin-echo length in one single shot. This will make time-dependent measurements on subsecond timescale possible.

SESANS

Samenvatting

Spin-Echo Small-Angle Neutron Scattering (SESANS) ofwel Spin-Echo kleine-hoek Neutronenverstrooiing is een techniek waarmee lengteschalen vanaf een paar nanometer tot mikrons bepaald kunnen worden. Met SESANS kan informatie over de struktuur van materialen verkregen worden. Strukturele informatie betekent de grootte en de vorm van een object. In een SANS meting worden de gegevens als functie van de impulsoverdracht verzameld. Hierbij is het erg moeilijk om bij hoeken in de buurt van nul te meten omdat dan de verstrooide bundel samen gaat vallen met de invallende bundel en daardoor de twee dimensionale detector op grote afstanden van het preparaat geplaatst moet worden. Echter in SESANS worden gegvens verkregen als functie van de spin-echo lengte die met eigenschappen van het preparaat in de reële ruimte correspondeert. Elk meetpunt bevat automatisch een integratie over de impulsoverdrachtsruimte. Hierdoor zijn de effecten bij kleine hoeken net zo gemakelijk meegenomen in een meting als die bij grote hoeken. Omdat men met SESANS de geïntegreerde intensiteit meet is het niet nodig om de bundel te collimeren wat in een hoge telstatistiek resulteert.

Het onderliggende principe van SESANS is de Larmor precessie van gepolariseerde neutronen. De opstelling bestaat uit twee precessiearmen waarin de neutronen effectief gezien in tegengestelde richting precederen. Wanneer er geen verstrooiing plaatsvindt is de hoeveelheid precessie in de eerste arm gelijk aan die in de tweede arm. Dit is de echosituatie. Echter, als er verstooiing is, is de hoeveelheid precessie in de eerste arm niet gelijk aan die in de tweede arm vanwege de padlengteverschillen voor het neutron in de eerste en de tweede arm. Dit zal leiden tot depolarisatie van de bundel. De mate van depolarisatie hangt af van de struktuur van het preparaat.

Er zijn vier opties om SESANS te realiseren. Deze zijn: de drie-folie optie, wiggen optie, resonant veld optie en vier-folie optie. In alle opties

worden er dipool magneten gebruikt die een magnetisch veld loodrecht op de neutronen richting genereren. In dit proefschrift wordt de drie-folie optie uitgebreid behandeld.

De drie-folie optie bevat enkel- en dubbelfolies die gemakelijk te magnetiseren zijn. Deze worden als respectievelijk $\pi/2$ en π flippers gebruikt. De opstelling bestaat uit drie dipool magneten. In de eerste en laatste magneet zijn enkelfolies en in de middelste magneet is een dubbelfolie opgesteld. Deze folies maken alle dezelfde hoek met de gemiddelde neutronenrichting en vormen driehoekige precessiegebieden. De verstrooingshoek wordt gecodeerd met de precessie die evenredig is met de impulsoverdracht. In een SESANS meting wordt de polarisatie als functie van de spin-echo lengte gemeten. Deze lengte is evenredig met het veld in de magneten, de afstand van het preparaat tot de magneet en het kwadraat van de golflengte. De polarisatie is evenredig met de cosinus transformatie van impulsruimte naar de reële ruimte van de hoeveelheid verstrooiing van het preparaat.

Meervoudige verstooiing kan makelijk analytisch behandeld worden in tegenstelling tot SANS. In SESANS resulteert meervoudige verstooiing in een snellere afname van de polarisatie als functie van de spin-echo lengte .

Er zijn twee eisen waaraan voldaan moet worden in een SESANS magneet. Ten eerste moet het magneetveld in het midden van de magneet in een ruimte van $30 \times 30 \times 30$ mm^3 homogeen zijn binnen 1.3 G bij een veldwaarde van 2000 G. De reden hiervoor is dat de precessiehoek een lineaire functie van de hoogte van het neutronenpad moet zijn om hoek labelling te realiseren. Als het veld niet homogeen is dan zal de precessiehoek een niet lineaire afhankelijkheid van het veld hebben. De vereiste homogeniteit van het veld kan gemakelijk gerealiseerd worden als de breedte van de poolschoenen 18 cm is. Om gewicht te besparen, is de straal van de ijzeren kern van de pool teruggebracht tot 12 cm waarbij de dikte van de poolschoen op 3 cm is gehouden om verzadigingseffecten te voorkomen. Met deze parameters, om een veld van 2000 G te hebben, is een totale stroom van 5000 A nodig door elk pakket windingen dat één pool omvat.

Ten tweede moet de lijnintegraal een homogenitiet van 2.2 G.cm hebben over de bundeldoorsnede. Deze homogeniteit kan niet bereikt worden door de poolafstand te vergroten. De inhomogeniteiten in de lijnintegraal zijn ten gevolge van de buiging van de veldlijnen bij de ingangs- en uitgangsopening van de magneten. Inhomogeniteiten in de verticale component van het veld zullen niet bijdragen tot de fouten in de lijnintegraal. Deze zijn evenredig met het kwadraat van de loodrechte componenten van het veld. Twee externe sets spoelen worden gebruikt om de lijnintegraal te homogeniseren. De eerste set bestaat van vier spoelen. Deze bevatten vier stroom voerende draden die parallel lopen aan de gemiddelde neutronenrichting. De afstanden

tussen de draden zijn op een dusdanige manier gekozen dat zij tezamen een kwadratisch veranderende veld genereren gezien in beide richtingen loodrecht op de neutronen bundel.

Deze eerste spoelset transformeert eigenlijk de variatie van de lijn integraal van de ene loodrechte richting naar de andere. De inhomogeniteit die in deze nieuwe richting is ontstaan wordt gecorrigeerd met een tweede, parabolische spoel die in de bundel wordt gezet. Voor een bundel van 15 mm hoog en 10 mm breed wordt de polarisatie verbeterd van 0.25 naar 0.86.

Modelberekeningen zijn uitgevoerd om de SESANS correlatiefunctie uit te rekenen. Lengteschalen die voorkomen in bollen, cylinders en ellipsoden kunnen gemakelijk bepaald worden. Anderzijds kan SESANS een Gaussische polydispersiteit voor spherische deeltjes niet bepalen. De Guinier benadering kan op dezelfde manier toegepast worden als met SANS om de Guinierstraal te bepalen. Effekten van de struktuurfactor zijn duidelijk zichtbaar in het SESANS signaal. Bij harde bollen zijn er oscillaties zichtbaar rondom de nulniveau van de SESANS correlatiefunctie. Een analytische uitdrukking is verkregen voor systemen die met het Debye-Lorentz model beschreven kunnen worden. Deze berekeningen laten zien dat het mogelijk is om met SESANS interpretaties te doen in reële ruimte.

Het SESANS principe is aangetoond met metingen aan kalksteen. De schalingsformule voor multiple verstooing is met succesvol toegepast op kalksteen metingen aan preparaten van verschillende dikte.

De eerste kwantitative metingen in Delft zijn uitgevoerd op latex bolletjes van 60 en 100 nm. De berekeningen zonder enige aanpasbare parameters zijn goed in overstemming met de metingen voor 100 nm deeltjes. In geval van de 60 nm bolletjes is er een klein verschil tussen de meting en de bereking die niet is begrepen. Het zou onmogelijk zijn om deze metingen uit te voeren op conventionele SANS machines zoals LOQ bij ISIS; en het zou net mogelijk zijn bij D11 in ILL.

SESANS kan zeer efficient toegepast worden bij een gepulseerde neutronen bron omdat de spin-echo lengte evenredig is met het kwadraat van de golflengte. Daarom is het mogelijk om de gehele depolarisatie curve als functie van de spin-echo lengte te meten in een enkele puls. Dit zal tijdafhankelijke metingen op subseconde tijdschaal mogelijk maken.

SESANS

Özet

Spin-Echo Small-Angle Neutron Scattering (SESANS) veya Spin-Eko Küçük-Açı Nötron Saçılım'ı bir SANS tekniği olup reel uzayda bir kaç nanometreden mikron seviyesine kadar olan uzunluklari ölçebilmektedir. SESANS'la malzemeler hakkında yapısal bilgi edinilebilir. Burada yapısal bilgiden maksat cisimlerin şekil ve büyüklüğüdür. SANS'la data momentum transferinin fonksiyonu olarak ölçülür. Bu teknikle sıfıra yakın açıları ölçmek oldukca zordur. Çünki bu durumda iki boyutlu dedektörü numuneden oldukca uzağa koymak gerekiyor. Oysa SESANS'la data spin-eko uzunluğunun bir fonksiyonu olarak elde edilmektedir. Her data noktası otamatik olarak momemtum uzayı üzerinden alınan integrayonu içerir. Bu sebeble küçük açılar büyük açılar kadar kolay ölçülebilmektedir. SESANS'la entegre edilmiş şiddet ölçüldüğü için ışınları paralel hale getirmek gerekmez, bu da yüksek sayısal istatistik manasına gelir.

SESANS'ın temelinde yatan prensip polarize edilmiş nötronların Larmor presesyon hareketidir. Düzenek iki presesyon kolundan meydana gelmekte olup her bir kolda nötronlar efektif olarak zıt yönlerde presesyon hareketi yaparlar. Saçılım olmadığı zaman, birinci koldaki presesyon miktarı ikinci koldaki presesyon miktarına eşit olur. Bu eko durumudur. Ancak numunede saçılım meydana gelirse, herbir kolda katedilen mesafe farklı olacağı için nötronlar depolarize olur. Depolarize miktarı numunenin yapısal özelliklerine bağlıdır.

SESANS dört yolla gerçekleştirilebilir. Bunlar üç folyo, kama, rezonant alan ve dört folyo seçeneğidir. Herbir seçenekte dipol mıknatıslar kullanılmakta olup bu mıknatıslar nötronların hareket doğrultusuna dik manyetik alan oluşturular. Bu tezde üç folyo seçeneği detaylı bir şekilde incelendi.

Üç folyo seçeneğinde, kolay mıknatıslanabilir tek ve çift folyolar $\pi/2$ ve π çeviricileri olarak kullanılır. Düzenek üç dipol mıknatısdan oluşmaktadır. İlk ve son mıknatısta tek, orta mıknatısda ise çift folyolar monte edilmiş durumdadır. Bu folyolar nötronların hareket doğrultusuna göre eğik durumdadırlar ve üçgensel presesyon bölgesi oluştururlar. Saçılma açısı presesyon açısıyla kodlanır ki bu da momentum transferiyle doğru orantılıdır. Ölçülen büyüklük spin-eko uzunluğunun fonksiyonu olarak polarizasyondur. Bu uzunluk manyetik alan, numune ile mıknatıs arasındaki mesafe ve dalga boyunun karesi ile doğru orantılıdır. Polarizasyon numunenin saçma gücünün momentum uzayından reel uzaya olan kosinüs tranformasyonu ile orantılıdır.

SANS'a mukabil katlı saçılım analitik olarak incelenebilir. SESANS'da katlı saçılım polarizasyonun, spin-eko uzunluğunun fonksiyonu olarak hızlı bir şekilde azalmasına sebebiyet verir.

SESANS mıknatısında yerine gelmesi gereken iki gereklilik şartı var. Birincisi $30 \times 30 \times 30$ mm^3'lik bir hacimde 2000 G'lık bir alan için manyetik alan 1.3 G içerisinde homojen olamlıdır. Bunun sebebi, açısal kodlamanın gerçekleşmesi için, presesyon açısının yüksekliğin linier bir fonsiyonu olması gereğidir. Eğer alan homojen olmazsa, o zaman presesyon açısı alana linier olmayan bir şekilde bağlı olur. Homojenlik şartı mıknatısın kutupsal genişliği 18 cm olduğunda kolayca sağlanabilir. Ağırlığı azaltmak için demir çekirdeğin yarıçapı 12 cm'ye düşürülürken kutupsal yüzlerin genişliği demirin doyma durumuna gelmesini engellemek için 3 cm'de tutuldu. Bu parametriler ile merkezde 2000 G'lik bir alan için, bir kutbu kapsayan bir akım paketinden geçen toplam 5000 A'e ihtiyaç vardır.

İkinci olarak çizgisel integral nötron hüzme kesiti üzerinde 2.2 G.cm'lik homogjenliğe sahip olmalıdır. Bu ise kutup mesafesini arttırmakla sağlanamaz. Çizgisel integrayon hatalarının temel sebebi, mıknatısların giriş ve çıkışlarında manyetik alanın saçaklanmasıdır. Manyetik alanın düşey bileşenleri çizgisel integrasyon hatalarına sebebiyet vermezken bu hatalar alanın dik bileşenlerinin karesiyle doğru orantılıdır. Bu hataları düzeltmek için iki harici bobin kullanılır. Birinci bobin dört parça bobinden oluşur. Bunlar nötronların hareket doğrultusuna paralel akım taşıyan dört tel içerir. Teller arası mesafe nötronların hareket doğrultusuna dik iki yönde, manyetik alan iki derceden artacak şekilde ayarlanır.

Birinci bobin aslında çizgisel integrasyondaki değişimi bir dik yönden diğer dik yöne çevirir. Bu yeni yöndeki hata hüzmeye yerleştirilen parabolik biçimli ikinci bir bobinle düzeltilir. 15 mm yüksekliğinde, 10 mm açıklığındaki bir hüzme için polarizasyon 0.25'den 0.86'ya çıkarılabilmektedir.

SESANS korelasyon fonksiyonunu hesaplamak için model hesaplamaları yapıldı. Küre, silindir, elipsoid gibi sistemlerdeki mevcut karakteristik uzunluklar direkt olarak belirlenebilmektedir. Öte yandan küresel sistemler için

Gauss dağılımına göre olan polydisperslik SESANS'la belirlenemiyor. Guinier yaklaşımı SANS'da olduğu gibi uygulanmakta olup Guinier yarıçapı belirlenebilinir. Strüktür faktör etkileri SESANS sinyalinde belirgin bir biçimde ortaya çıkıyor. Sert küre etkileşimi SESANS korelasyon fonsiyonunun sıfır seviyesinde osilasyonlar olarak belirmektedir.

SESANS prensibi kalker ölçümleri ile ispatlandı. Katlı saçılım için olan ölçekleme formülü başarılı bir biçimde değişik kalınlıkta ki kalker numunelerine uygulandı.

Delft'teki ilk kantitatif ölçümler 60 ve 100 nm'lik lateks küreler ile yapıldı. Ayarlanabilir parametresiz hesaplamalar ile ölçümler, 100 nm parçacıklar için birbiriyle uyuşmaktadır. 60 nm kürelerde ise ölçümle hesap arasında ufak bir fark bulunmaktadır ki bu henüz anlaşılabilmiş değildir. Bu tür ölçümleri ISIS'deki LOQ gibi konvansiyonel SANS aletiyle yapmak imkansız, ILL' de D11 ile yapmak ise ancak mümündür.

Spin-eko uzunlugu dalga boyunun karesiyle orantılı olduğu için, SESANS vurulu kaynaklarda etkin bir şekilde kullanılabilir. Bu sebele spin-eko uzunluğunun bir fonksiyonu olarak bütün bir depolarizasyon eğrisi tek bir vuru ile ölçülebilir. Bu ise zamana bağlı saniye altı ölçümleri mümkün kılmaktadır.

Dankwoord

Het produceren van een proefschrift kan niet alleen worden toegeschreven aan een enkel persoon. Daarom wil ik alle mensen bedanken die hebben bijgedragen aan het tot stand komen van dit proefschrift. Zonder hun bijdrage zou het niet mogelijk geweest zijn om deze dissertatie te schrijven.

Wim Bouwman wil ik bedanken voor al zijn inspanningen. In de afgelopen vier jaar heb ik nooit het idee gehad dat ik zonder begeleiding zat. Dit in tegen stelling tot ramp verhalen die je regelmatig hoort wat betreft slechte begeleiding van promovendi. Hij heeft mijn teksten heel snel gelezen en van commentaar voorzien. Dit heb ik altijd zeer gewaardeerd. Ook hebben we vele interessante gesprekken gevoerd over religie in het bijzonder over de Islam n.a.v. kranten knipsels die ik kreeg van Wim.

Theo Rekveldt wil ik bedanken voor zijn waardevolle ideeën. Vooral de discussies die ik met hem heb gevoerd over lijn integraal correcties zijn zeer nuttig geweest. Je kan altijd bij hem terecht als er problemen zijn.

Don Kearley heeft in een later stadium de taak als promotor op zich genomen. Hem wil ik bedanken voor zijn inzet door met mij periodieke bijeenkomsten te houden over de gang van zaken.

De leden van het SESANS groep met wie ik elke maandag ochtend een bijeenkomst had wil ik ook van harte bedanken. Het was zeer leuk om met Wicher Kraan metingen te doen op de SP. De bereidheid van Jeroen Plomp om bij allerlei technische problemen snel te hulp te schieten heeft geleid tot de uitvoering van de metingen zonder vertraging. Tim Krouglov, Serguie Grigoriev en Mascha van Oossanen wil ik bedanken voor al hun inzet bij het SESANS project. Rob Kreuger wil ik bedanken voor de gedachtenwisselingen met hem over magneetveld berekeningen.

Tenslotte wil ik mijn familie bedanken voor al haar steun en vertrouwen in mij. Öncelikle yetişmemde büyük emekleri olan anne ve babama müteşekkirim. Onların üzerimde olan haklarını hiç bir zaman ödeyemem.

Ayrıca bana olan destek ve yardımlarından dolayı eşim Birgül'e, ablalarım Güllü ile Gülseren'e, kardeşlerim Aynur, Fatma ve Abdullah'a da teşekkür etmek isterim.

Curriculum Vitae

Oktay Uca was born on 2nd of December 1971 in Vlaardingen. After the primary school he went to İzmir/Turkey to attend secondary school in 1984. In 1990 he finished İzmir Atatürk Lisesi. In 1990 he studied for one year physics at Dokuz Eylül Üniversitesi in İzmir. In 1991 he came to the Netherlands and studied for one year physics at Hogeschool Holland in Diemen. He started studying physics at Utrecht University in 1992 of which he graduated from in 1997. After having a short Ph.D. period at Rijnhuisen Institute for plasma physics he started in September 1998 working as Ph.D. student at Interfaculty Reactor Institute, Delft. There he participated in the development of the Spin-Echo Small-Angle Neutron Scattering (SESANS) instrument. The results of that research are presented in this thesis.

List of Publication

Oktay Uca and Wim G. Bouwman and Wicher H. Kraan and M.Theo Rekveldt, "An analysis of magnetic field inhomogeneities in a spin-echo small-angle neutron scattering instrument", Physica B, 276-278, 136-137, 2000

Oktay Uca and Wicher H. Kraan and Wim G. Bouwman and M.Theo Rekveldt, "Line integral corrections in a spin-echo small-angle neutron scattering instrument", Physica B, 297, 28-31, 2001

Oktay Uca, Wim G. Bouwman, Jeroen Plomp, Wicher H. Kraan, M.Theo Rekveldt, "Line integral corrections in Larmor precession devices", Accepted for publication in Applied Physics A, 2002

Oktay Uca, Wim G. Bouwman and M.Theo Rekveldt, "Model calculations for the Spin-Echo Small-angle Neutron Scattering correlation function", Accepted for publication in Journal of Applied Crystallography, 2002

Oktay Uca, Wim G. Bouwman and M.Theo Rekveldt , "Magnetic design of a Spin-Echo Small-Angle Neutron-Scattering instrument", Accepted for publication in Nuclear instruments and methods in physics research A

W. G. Bouwman, M. Oossanen, W. H. Kraan, O. Uca and M. Th. Rekveldt, "Development of spin-echo small-angle neutron scattering", Journal of Applied Crystallography: 33, 767-770, 2000

M. Th. Rekveldt, W. G. Bouwman, W. H. Kraan, O. Uca, S. V. Grigoriev, K. Habicht and T. Keller, "Elastic neutron scattering measurements using Larmor precession of polarized neutrons", to be published in springer-verlag", 2002

M. Th. Rekveldt, W. G. Bouwman, W. H. Kraan, O. Uca, S. V. Grigoriev and R.Kreuger, "Technical aspects of Larmor precession with inclined front

and end faces", to be published in springer-verlag, 2002

Wim G. Bouwman, Oktay Uca, Serguei V. Grigoriev, Wicher H. Kraan, Jeroen Plomp and M. Theo Rekveldt, "First quantitative test of spin-echo small-angle neutron scattering", accepted for publication in Applied Physics A (2002)

Bibliography

[1] A.P. Radlinski and A.L. Hinde. Small angle neutron scattering and petroluem geology. *Neutron News*, 13:10–14, 2002.

[2] F. Mezei (edited by). Lecture notes in physics. *Springer-Verlag*, 128:183–188, 1979.

[3] R. Pynn. Neutron spin-echo and three-axis spectrometers. *J. Phys. E:Sci. Instrum*, 11:1133–1140, 1978.

[4] V.T. Lebedev, A.D. Dudakov, L. Cser, L. Rosta, and Gy. Torok. Real space small-angle scattering device. *Journal De Physique IV*, 3:481–485, 1993.

[5] T. Keller, R. Gähler, H. Kunze, and R. Golub. Features and performance of an nrse spectrometer at bensc. *Neutron News*, 6:16–18, 1995.

[6] M. Th. Rekveldt. Novel sans instrument using neutron spin echo. *Nucl. Instr. & Methods in Phys. Res. B*, 114:366–370, 1996.

[7] J.Baruchel, J.Hodeau, M.Lehmann, J.Regnard, and C.Schlenker. *Neutron and synchrotron radiation for condensed matter studies, Volume 1.* springer-verlag, 1995.

[8] B.H. Bransden and C.J. Joachain. Introduction to quantum meachanics. 1989.

[9] W.H. Kraan, M.Th. Rekveldt, and P.T. Por. Adiabatic rotators for 3-d neutron polarization analysis. *Nuclear Instruments and Methods in Physics Research A300*, pages 35–42, 1991.

[10] W. G. Bouwman, M. Oossanen, W. H. Kraan, O. Uca, and M. Th. Rekveldt. Development of spin-echo small-angle neutron scattering. *Journal of Applied Crystollography*, 33:767–770, 2000.

[11] M. Th. Rekveldt, W. G. Bouwman W. H. Kraan, O. Uca, S. V. Grigoriev, K. Habicht, and T. Keller. Elastic neutron scattering measurements using larmor precession of polarized neutrons. *to be published in springer-verlag*, 2002.

[12] J. Schelten and W. Schmatz. Multiple-scattering treatment for small-angle scattering problems. *J.Appl.Cryst*, 13:385–390, 1980.

[13] M. Th. Rekveldt, W. G. Bouwman W. H. Kraan, O. Uca, S. V. Grigoriev, and R.Kreuger. Technical aspects of larmor precession with inclined front and end faces. *to be published in springer-verlag*, 2002.

[14] W.H. Kraan, S.V. Grigoriev, R. Kreuger, F.M. Mulder, and M.Th. Rekveldt. Zero-field precession induced by adiabatic rf spin flippers. *Physica B*, 297:23–27, 2001.

[15] W.H. Kraan, S.V. Grigoriev, M.Th. Rekveldt, W.G. Bouwman, and O.Uca. Spin-echo sans based on adiabatic hf flippers in dipole magnets with skew poles. *Accepted for publication in Applied Physics A*, 2001.

[16] Michael Monkenbush, R. Schatzler, and D. Richter. The julich spin-echo spectrometer- design and performance. *Nuclear instruments and methods in physics research A*, 399:301–323, 1997.

[17] Virginia W. Miner and Woodrow W. Conover. *The Shimming of high resolution NMR magnets*. Acorn NMR Inc. http://www.acornmr.com, 1997.

[18] P. Elleaume, O. Chubar, and J. Chavanne. Computing 3d magnetic fields from insertion devices. *Proceedings of the particle accelerator conference 1997, Electronics & Communication Engineering Journal*, 3:3509–3511, 1998.

[19] M.G. Fedurin and N.A. Mezentsev. Achievement of one-coordinate cross uniformity of magnetic field in central pole of strong field superconducting wiggler. *Nuclear instruments and methods in physics research A*, 448:59–61, 2000.

[20] M.G. Fedurin, G. Kulipanov, N. Mezentsev, and V. Shkaruba. Superconducting high-field three-pole wigglers at budker inp. *Nuclear instruments and methods in physics research A*, 448:51–58, 2000.

[21] V.M. Borovikov, V.K. Djurba, and M.G. Fedurin et.al. Superconducting 7 wave length shifter for bessy-ii. *Nuclear instruments and methods in physics research A*, 467-468:181–184, 2001.

[22] Pc-aot-1.atdiv.lanl.gov (ip 128.165.32.190). *PC-AOT-1E.ATDIV.LANL.GOV (IP 128.165.34.239)*, 1999.

[23] *For more information see: http://www.esrf.fr/machine/ support/ids/Public/Codes/Radia/Radia.html.*

[24] Oktay Uca, Wim G. Bouwman, Wicher H. Kraan, and M.Theo Rekveldt. An analysis of magnetic field inhomogeneities in a spin-echo small-angle neutron scattering instrument. *Physica B*, 276-278:136–137, 2000.

[25] Oktay Uca, Wicher H. Kraan, Wim G. Bouwman, and M.Theo Rekveldt. Line integral corrections in a spin-echo small-angle neutron scattering instrument. *Physica B*, 297:28–31, 2001.

[26] Oktay Uca, Wim G. Bouwman, Jeroen Plomp, Wicher H. Kraan, and M.Theo Rekveldt. Line integral corrections in larmor precession devices. *Accepted for publication in Applied Physics A*, none:none, 2002.

[27] Michael Monkenbush. Correction scheme for divergent beams in zero-field spin-echo spectrometers. *Nuclear instruments and methods in physics research A*, 437:455–458, 1999.

[28] O. Uca, W. H. Kraan, W. G. Bouwman, and M. Th. Rekveldt. Line integral corrections in spin echo small angle neutron scattering instrument. *Physica B*, 297:28–31, 2001.

[29] J. Pedersen. Analysis of small-angle scattering data from colloids and polymer solutions: modeling and least square fitting. *Advances in colloid and interface science*, 70:171–210, 1997.

[30] Jinkui Zhao. Concepts in spin echo small-angle neutron scattering. *Journal of Applied Crystallography*, 34:639–645, 2001.

[31] David J. Kinning and Edwin L. Thomas. Hard-sphere interactions between spherical domains in diblock copolymers. *Macromolecules*, 17:1712–1718, 1984.

[32] S. V. G. Menon. A new interpretation of the sticky hard sphere model. *J. Chem. Phys.*, 95:9186–9190, 1991.

[33] W. G. Bouwman and M. Th. Rekveldt. Spin-echo small-angle neutron scattering calculations. *Physica B*, pages 126–127, 2000.

[34] O. Glatter. Interpretation of real-space information from small-angle scattering experiments. *J.Appl.Cryst.*, 12:166–175, 1979.

[35] T.M. Sabine and W.K. Bertram. The use of multiple-scattering data to enhance small-angle neutron scattering experiments. *Acta Cryst.*, A55:500–5007, 1999.

[36] I.S. Gradshteyn and I.M Ryzhik. *Table of Integrals series and products.* Academic press, 1965.

[37] G. Arfken. *Mathematical methods for physicists.* Academic press, 1968.

[38] Richard Janssen. *Structure and shear in a cohesive powder.*

[39] Marvin R., Gordon Osborne, Ken Lies, Ray Jordan, and Jr. Raymond M. Coveney. Complex refractive index of limestone in the visible and infrared. *Applied Optics*, 17:353–356, 1978.

[40] L. L. Long, M. R. Querry, R. J. Bell, and R. W. Alexander. Optical properties of calcite and gypsum in the crystalline and powdered form in the infrared and far-infrared. *Infrared Physics*, 34:191–201, 1993.

[41] *http://mineral.galleries.com/minerals/carbonat/calcite/calcite.htm.*

[42] D. S. Draper and D. Xirouchakis. Thermal emission spectroscopy of synthetic coesite and stishovite. *Lunar and Planetary Science XXXI, NASA Johnson Space Center Houston.*

[43] Stephen M. King. *Modern techniques for polymer characterization.* John Wiley and Sons Ltd, 1999.

[44] Stephen W. Lovesey. *Theory of neutron scattering from condensed matter, volume 1.*

[45] *http://www.isis.rl.ac.uk/largescale/loq/technical/tech_spec.htm.*

[46] L.A Feigin and D.I Svergun. *Structure analysis by small angle X-ray and Neutron scattering.* plenum publishing, 1987.

[47] *http://www.ill.fr/YellowBook/D11/.*

[48] *http://www.fz-juelich.de/ess/ess/technical_data.htm.*